Enhanced Isogeometric Analysis of Fracturing in Solid and Porous Media

Farshid Fathi

A report submitted in partial fulfilment for the
degree of Doctor of Philosophy

in the

Department of Civil and Structural Engineering

September 2021

Enhanced Isogeometric Analysis of Fracturing in Solid and Porous Media

Farshid Fathi

A report submitted in partial fulfilment for the
degree of Doctor of Philosophy

in the

Department of Civil and Structural Engineering

September 2021

Declaration

All sentences or passages quoted in this document from other people's work have been specifically acknowledged by clear cross-referencing to author, work and page(s). Any illustrations that are not the work of the author of this report have been used with the explicit permission of the originator and are specifically acknowledged. I understand that failure to do this amounts to plagiarism and will be considered grounds for failure.

Name: **Farshid Fathi**

Signature: **Farshid Fathi**

Date: **December 2021**

Abstract

EXtended Finite Element Method (XFEM) decouples the crack path from the discretisation, a major advantage compared to interface elements for simulating arbitrary fracturing. Also, avoiding the costly option of remeshing, XFEM enables propagating discontinuities to be modelled on the original mesh layout. XFEM, however, has been replaced by other techniques, such as meshless methods, to provide higher-order continuity across element boundaries. This is required to remove stress jumps at element boundaries, to improve stress estimates particularly in the presence of a discontinuity, and to locally satisfy mass conservation of the fluid part needed at element boundaries of a porous medium. With the advent of IsoGeometric Analysis (IGA), spline bases have been proposed to provide $C^{\mathbb{p}}$-continuity ($\mathbb{p} > 0$) across element boundaries, which also have been incorporated in XFEM, so-called eXtended IsoGeometric Analysis (XIGA), to replace the underlying C^0-continuity of the Lagrangian interpolations. Within the realm of Linear Elastic Fracture Mechanics (LEFM), XIGA has been well addressed, but not so far cohesive zone models. The interelement sharing of control points in splines removes the Kronecker-Delta property available for Lagrange interpolation underlying the customary finite element method. These features complicate elementwise enrichment of individual control points, as well as the compatibility enforcement. The latter is of utmost importance as a possible source of error, which has not been well addressed for XIGA despite the full investigation carried out in the original contribution combining IGA and XFEM. Shifting technique can localise the effect of the Heaviside function, although, unlike XFEM, it stretches to the blending elements. This is similar to the effect of blending technique to enforce compatibility in XFEM. An XIGA formulation is proposed for Non-Uniform Rational B-splines (NURBS) to account for small strain and geometrically nonlinear cohesive fractures. Compatibility enforcement is realised of shifting and blending techniques perpendicular and parallel to the discontinuity, respectively. The latter enables removing the undesired effect of the discontinuity ahead of the crack tip, which is absent in recent XIGA contributions. To provide a standard finite element data structure Bézier extraction is utilised. In a further development, XIGA is augmented with the Local Maximum Entropy (LME), a meshless technique with superior features to elevate the accuracy of the enhanced section, which is coined X-IGALME. The results indicate a guaranteed stability of the solution for X-IGALME, where XIGA and XFEM fail. Unlike elementwise approaches, the singularity-free characteristic of X-IGALME facilitates a single prescription for enrichment in any condition, including void level set. Finally, XIGA for a progressively fracturing porous medium is investigated, representing a successful fracture simulation in fluid saturated porous media using a 2PDOF (two pressure degrees of freedom) model.

Acknowledgment

It has been a privilege and pleasure to work under the guidance and inspiration of my supervisor, Professor René de Borst. His unceasing support, kindness and patience have made a great learning environment rare to come across, reminding me how fortunate I was to be a member of his group in the last four years. I clearly remember that I used to finish each of our fruitful discussions with the same sentence *"Thanks, I have learnt a lot!"*.

I would like to express my deepest gratitude to Professor Harm Askes for his unconditional support, particularly in the beginning of my PhD journey. I wish to extend my sincere appreciation to the members of my thesis committee, Dr Inna Gitman and Dr Fehmi Cirak, for their insightful comments and suggestions. It has been a pleasure working with Dr Lin Chen for his mentorship. I really enjoyed our countless constructive discussions, even until late in evenings.

Many other people have guided and supported me during the last four years. I have had highly informative discussions with Dr Yousef Ghaffari-Motlagh, Dr Fathima Mehmanzai, Dr Daniele Tartarini, Dr Isa Kolo, Dr Tim Hageman and Dr Sepideh Alizadeh Sabet. I would like to thank Dr Eric Jan Lingen of Dynaflow Research Group for the course delivered and his support regarding the software Jem/Jive. I am also grateful for support from The University of Sheffield, particularly during the last semester. The financial support by ERC Advanced Grant 664734 "PoroFrac" and Department of Civil and Structural Engineering are gratefully acknowledged.

Finally, around half of this work has been carried out during the Covid-19 pandemic. Support of family has been the main source of energy to overcome this hard time. Moreover, special thanks go to my friends - Peyman, Nina, Serena, Sourabh, Francesca and Grant - who were always by my side as my second family.

Farshid Fathi
Sheffield, December 2021

Contents

List of Figures

List of Tables

Chapter 1

Introduction

Engineering disciplines are replete with experimental studies, as they serve the most explicit way to tackle a wide spectrum of problems. With the advent of Finite Element (FE) approach, numerical simulations became a new alternative to explore engineering problems. They quickly became widespread, particularly in the cases where experimental studies were unjustifiable. Some of these cases, for instance, encompass: a rare or expensive material to be supplied; a complex boundary condition to be satisfied; several variables to be controlled simultaneously; or high risks to be taken while experimenting. Nowadays, computers have become an integral part of modern engineering, ranging from personal laptops to high performance computing (HPC) clusters at universities. Developments in computer science and technology have equipped smallest portable computers with computing facilities. Now, computational mechanics has reached its pinnacle, capable of simulating extremely complex physical phenomena, which is even elevated to a new level where Computer-Aided Design (CAD) and analysis tools are integrated in one. This was originated to reduce computational cost by bypassing the cumbersome mesh generation stage in analysis and to retain the precision obtained from the design [30, 66, 74, 75]; the method was coined IsoGeometric Analysis (IGA).

Non-Uniform Rational B-splines (NURBS), a technology built on B-splines but superseding them in exact parametrisation of conic shapes and quadratic surfaces [35], are considered the predominant approximants in CAD packages. NURBS incorporation into IGA suffered from a deficiency often needed for the analysis stage, local mesh refinement. Though this issue was resolved later [147], it led to the development of T-splines [12] as a powerful tool to capture arrbitrary topological complexity, which also alleviated the difficulties associated with the use of tensor products [119]. Later, it was also cast in the finite element data structure [117]. Therefore, using NURBS, the scene was set for a design-through analysis of an at least accurately parametrised geometry [35]. While it has been widely used for intact materials,

extension to fracture and fracturing dominant materials is the focus of this thesis. Exploiting knot insertion [138], lowering the continuity-order of splines by increasing the multiplicity of knot values, discontinuities were introduced for interface elements in IGA. Prior to this, IGA had been combined with XFEM for Linear Elastic Fracture Mechanics (LEFM) [39].

1.1 Problem Statement and Thesis Objectives

The objective of this thesis is to incorporate the extended approach into NURBS-based IGA for fracture analysis. Particularly, the focus is set on cohesive-zone models realised of solid and fluid saturated porous media. This blending between NURBS and the extended approach was first studied by De Luycker et al. [39] where blending technique was used to enforce compatibility. Different aspects of the proposed approach were discussed. Unlike the original work, compatibility enforcement was absent in later XIGA contributions, a necessity to render the original and extra layers consistent. This is of utmost importance, particularly for XIGA where higher interelement continuity at element borders extends the discontinuous domain to the intact zone ahead of the fracture incorrectly. By utilising an extended approach in this thesis:

- The crack path is decoupled from the underlying mesh layout, i.e. the inclusion of the discontinuity within the displacement field allows for an independent extension of the crack with respect to the original discretisation.
- Compatibility enforcement perpendicular and parallel to the crack path is comprehensively studied using shifting and blending techniques, respectively.
- Comparison between the current extended approach results and other customary finite element approaches, e.g. standard interface element and XFEM approaches, is made for small strain and geometrically nonlinear regimes.
- Efficacy of the developed formulations is assessed in new territories to blend finite element and entropy-based meshfree approaches in an extended framework. This blend exploits the best of both approaches.
- Higher interelement continuity is utilised to locally satisfy the mass conservation of fluid saturated porous media at element boundaries, the requirement absent in Lagrange basis functions underlying customary finite element approach.

1.2 Fracture Modelling

The notion of fracture encompass nucleation, growth and coalescence of micro cracks which materialises in the form of a single discontinuity at the marco structure. Micro structures and

their effects on a macro crack can be studied as parts of a multi-scale analysis. Nevertheless, continuum fracture simulations can be divided into two general groups: discrete and smeared approaches.

1.2.1 Smeared approach

The closest approach to the stiffness deterioration caused by micro-mechanical phenomena is referred to as smeared approach, also known as continuum failure model, which is generally based on strain softening, a reduction of the load bearing capacity caused by an increase of the inelastic strain. Applications of such approach encompass continuum damage mechanics [88], anisotropic damage models [11] and plasticity [48]. Classical continuum models suffer from the possibility to become ill-posed, where zero energy dissipation incurs complete loss of integrity [142]. Accordingly, strain localisation occurs within a zero band-width, leading to mesh dependency. Preserving the same kinematic concepts, nonlocal terms were introduced to the classical continuum models, rendering the governing equations well-posed at face of strain softening [101]. Gradient enhanced [36, 81, 80, 79] and rate dependent [94, 124] models are other approaches to obtain well-posed equations. Moreover, Cosserat continuum also renders well-posed governing equations for shear loading [38, 2, 63]. The common feature between all of these approaches is the need for a length scale explicitly/implicitly applied to control the width of the localisation zone, while a zero length scale recovers the classical continuum theory.

1.2.2 Discrete approach

Another set of fracture models utilise real crack definition, either in the form of degrees of freedom defined explicitly for the discontinuity [111, 114] or as an extra discontinuous term introduced in the kinematics of strain or displacement field. For the former, either a priori knowledge of the crack path or adaptive remeshing [130] is required for fracture modelling, while the latter decouples the crack path from the underlying mesh layout. Discontinuity inclusion in strain or displacement field is entirely dependent on the physics of material. For instance a sharp displacement gradient within a small region is observed for metals, suggesting a continuous displacement field followed by a discontinuous strain field. Therefore kinematic inclusion of discontinuity can represent strong or weak discontinuities based on the discontinuity in the displacement or strain fields, respectively.

Linear elastic fracture mechanics (LEFM) is the most conventional way to model discontinuities, which assumes a traction-free crack within an elastic bulk. In the case of a considerable inelastic deformation taking place in front of the crack tip, however, other approaches should be utilised. The most common approach, for quasi-brittle materials for

instance, is to lump the inelastic deformations as cohesive tractions forced on a fictitious extension of the crack line, see Figure 1.1. This is equivalent to concentrate the effect of the micro cracks in a line in front of the crack tip, so called the process-zone. The size of this zone is an important concept to decide between LEFM and cohesive-zone models. When the size of the fracture process zone is small compared to a typical structural dimension, linear elastic fracture mechanics [57, 69] is the method of choice. However, when the fracture process zone becomes non-negligible, cohesive-zone models [10, 41, 64] are often more applicable from a physics point of view. This holds, for instance, for many problems in fractured, fluid-saturated porous media [107]. Fracture models were also realised for meshless methods [16, 40], where a discontinuity is incorporated by adding dicontinuous terms in the basis function which approximate the displacement field [49].

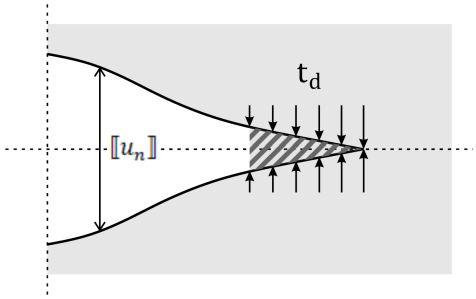

Figure 1.1: Cohesive-zone model in the form of tractions t_d acting on the fictitious crack extension. The hatched section illustrates the crack extension equivalent to the fracture process-zone. The normal displacement jump is also indicated by $[\![u_n]\!]$.

1.3 Porous Media

Fluid flow in a deforming porous medium has always been a topic of attention due to its numerous applications in, for instance, petroleum and geotechnical engineering [139], biology and medical sciences [85, 97, 137], and three-[125] or four-phase[67, 136] media considering ion transport and electrical charges. At early stages, the theory was limited to the intact porous materials [132, 18, 31, 84]. Analytical solutions considering fracture are available [99, 52, 96], but restricted to simplifying assumptions such as linear elastic, homogeneous and impermeable materials with an idealised geometry. As one of the earliest numerical models to consider the discontinuity, the fluid flow in a fracturing porous medium was explored [21] where finite element and finite difference methods were exploited for discretisation of the bulk and approximation of fluid flow inside the fracture, respectively.

Different aspects of fractured and/or fracturing simulations for saturated/unsaturated porous media were studied in a set of papers by de Borst and co-workers [37, 104, 106], also

for shear bands [105] and large deformation dominant materials [70]. Moreover, implications of a continuous/discontinuous pressure models across the discontinuity was carried out using hydromechanical interface elements [47]. IGA was first adopted for the intact porous materials [71]. It was developed for fractured and/or fracturing porous media using the hydromechanical interface elements [72] which was later augmented with mass transport models inside the fracture for stationary cracks [140, 59]. Hydromechanical interface elements were exploited for simulation of non-Newtonian fluids [58, 62, 61] and multi-phase problems [60]. Comprehensive studies on finite element-based fracture in porous media, including IGA, can be found in de Borst's works [32, 33].

1.4 Thesis Outline

A brief review of mathematical requirements is presented in the second chapter to provide sufficient background for the ensuing chapters. Next, XIGA formulation is developed for cohesive fracture in the solid phase. Implementation aspects, comprising shifting and blending techniques, are comprehensively studied. The developed formulation is proposed for geometrically nonlinear delamination in composites in the fourth chapter. The use of a sign function instead of a Heaviside step function removes the need to make an assumption for the normal to the crack at its centreline. The performance of XIGA results is compared with those of XFEM at the hand of some examples including buckling and large rotations. The fifth chapter blends XIGA and LME to exploit the best of both methods at the boundaries and in the vicinity of the crack, respectively. Implications of this blend, coined X-IGALME, is studied by a variety of examples each aim to verify a specific aspect, one at a time. Finally, a two pressure degrees of freedom XIGA model is proposed for coupling fluid with the fracturing solid in the sixth chapter before the thesis finishes with Conclusion chapter.[1]

[1]This chapter is partly based on:

Fathi, F., Chen, L. and de Borst, R., 2020. Extended isogeometric analysis for cohesive fracture. International Journal for Numerical Methods in Engineering, 121(20), pp.4584-4613.

Fathi, F., Chen, L. , Hageman, T. and de Borst, R., 2021. Extended isogeometric analysis of a progressively fracturing fluid-saturated porous medium. Submitted to International Journal for Numerical Methods in Engineering.

Chapter 2

Mathematical Background

This chapter[1] provides the mathematical background to form an eXtended IsoGeometric Analysis (XIGA) approach. It consists of two sections: IsoGeometric Analysis (IGA) preliminaries and Generalised/eXtended Finite Element Method (G/X-FEM). The IGA section starts with B-splines, as the corner-stone of spline technologies, followed by a brief account on its transformation into Non-Uniform Rational B-spline (NURBS). Bézier extraction, used in this thesis entirely, casts the formulation in finite element data structure format. The IGA section concludes with point projection technique utilised for line integration procedure in this thesis.

Section 2.2 discusses the kinematics of displacement discontinuity within a G/X-FEM approach. It continues with brief discussions about level-set technique, physics of discontinuity, cohesive-zone model and crack extension direction.

2.1 Isogeometric Analysis Preliminaries

Isogeometric analysis was originally developed to integrate design and analysis tools, particularly to retain the accuracy stemmed from the design and to bypass meshing process in the analysis phase [22]. This led to a direct incorporation of basis functions available in computer-aided design packages into the analysis phase [140, 95, 22]. Another advantage of isogeometric analysis over traditional finite element analysis is the higher-order interelement continuity that supersedes the customary C^0-continuous Lagrange shape functions in traditional FEM [72, 35]. Exploiting a smooth basis function removes computational issues in fluid-structure interaction [14, 13], and improves the discretisation of higher-order differen-

[1]This chapter is partly adopted from:

Fathi, F., Chen, L. and de Borst, R., 2020. Extended isogeometric analysis for cohesive fracture. International Journal for Numerical Methods in Engineering, 121(20), pp.4584-4613.

tial equations in phase field models [23], Kirchhoff-Love plate theory [95], or gradient damage models [138], to name a few.

The possibility of employing higher-order continuity with spline basis functions allows to remove the jump in derivatives, e.g. it can lead to a continuous stress field [140]. This facilitates simulating fracture by improving the stress estimation, and thus predicting propagation onset and direction more accurately. In finite element analysis, shape functions are constructed with Lagrange polynomials, while isogeometric analysis replaces these polynomials with spline basis function used to generate the geometry in design industry.

Traditionally, spline basis functions were defined over the parametric domain, unlike traditional finite element analysis that provides an element-wise framework in which the basis functions are defined over a canonical set of shape functions over a parent element [35]. With the aim to set an element-based structure for IsoGeometric Finite Element Analysis (IGFEA), Bézier elements were utilised. The formulation is elaborated in the following sections.

2.1.1 B-splines

Despite all the differences between design and analysis, both exploit the same conceptual idea which is a linear combination of basis functions, N_k, in parametrising the geometry [35].

$$\mathbf{x}(\xi) = \sum_{k=1}^{n} N_k(\xi)\mathbf{P}_k, \tag{2.1}$$

where $\mathbf{x}$ is the parametrised geometry and $\mathbf{P}_k$ denotes the point-set, for instance it serves as the set of nodal point in customary finite element analysis.

A univariate B-spline is a piecewise polynomial represented with a monotonically increasing set of values, usually referred to as the knot vector, $\Xi = \{\xi_1, \xi_2, \cdots, \xi_{n+p+1}\}$; n and p denote the number and the order of the basis function, respectively. The knot vector Ξ is constructed of m non-negative intervals representing the number of elements in the parameter domain. By increasing the multiplicity of the first and the last knots to $p+1$, a so-called *open knot vector* results. Since our work only deals with open knot vectors, they are denoted as *knot vectors* in the remainder.

The geometry of a B-spline is also parameterized as a linear combination of basis functions N:

$$\mathbf{x}(\xi) = \mathbf{P}^{\mathrm{T}}\mathbf{N}(\xi). \tag{2.2}$$

where $\mathbf{N}$ maps a coordinate ξ from the parameter domain onto the physical domain, and $\mathbf{P}_k$ is the set of control points. The B-spline basis functions are recursively defined by the

Cox-de Boor formula:

$$N_{k,p}(\xi) = \frac{\xi - \xi_k}{\xi_{k+p} - \xi_k} N_{k,p-1}(\xi) + \frac{\xi_{k+p+1} - \xi}{\xi_{k+p+1} - \xi_{k+1}} N_{k+1,p-1}(\xi), \tag{2.3}$$

with the initial value:

$$N_{k,0}(\xi) = \begin{cases} 1 & \xi_k \leq \xi < \xi_{k+1} \\ 0 & \text{otherwise.} \end{cases} \tag{2.4}$$

2.1.2 Nonuniform rational B-splines (NURBS)

B-splines were replaced by NURBS in Computer-Aided Design (CAD) [66] owing to their ability to accurately parameterize conic shapes [35]. Similar to a univariate B-spline, a NURBS is a parametrised curve defined over the piecewise polynomial basis function $\{R_{k,p}(\xi)\}_{k=1}^{n}$, where n and p denote the number and the order of the knot vector, respectively. Since spline-based basis functions share the same features, a NURBS curve can be rewritten similar to Equation (2.1):

$$\mathbf{x}(\xi) = \sum_{k=1}^{n} R_k(\xi)\mathbf{P}_k. \tag{2.5}$$

A NURBS basis function R is defined as a weighted B-spline basis function N:

$$R_{k,p}(\xi) = \frac{w_k N_{k,p}}{W(\xi)}, \tag{2.6}$$

with $N_{k,p}$ defined in Equations (2.3) and (2.4), w_k is the corresponding weight, and $W(\xi) = \sum_{k=1}^{n} N_k(\xi) w_k$ is the weighting function. The univariate NURBS curve defined in Equation (2.5) can be extended to a bivariate (surface)

$$\mathbf{S}(\xi, \eta) = \sum_{k=1}^{n} \sum_{l=1}^{m} R_{k,l}^{p,q}(\xi, \eta)\mathbf{P}_{k,l}, \tag{2.7}$$

with the bivariate NURBS basis function defined as the tensor product of univariate bases [22] as:

$$R_{k,l}^{p,q}(\xi, \eta) = \frac{N_{l,q}(\eta) N_{k,p}(\xi) w_{k,l}}{\sum_{\hat{k}}^{n} \sum_{\hat{l}}^{m} N_{\hat{k},q}(\eta) N_{\hat{l},p}(\xi) w_{\hat{k},\hat{l}}}. \tag{2.8}$$

2.1.3 Computation of Bézier extraction

As mentioned previously, the traditional spline technology does not follow a local element-wise structure as a finite element framework does. With the aim to provide an element-based

structure, Bézier extraction was utilized. A degree p Bézier curve can be defined as a linear combination of Bernstein polynomial basis functions and a set of control points [22]. The Bernstein polynomials can be recursively defined over [-1 1]. It is noted that these polynomials are originally defined for $\xi \in [0\ 1]$, while it is presented for [-1 1] to facilitate the integration scheme [22]:

$$\mathcal{B}_{k,p}(\xi) = \frac{1}{2}(1-\xi)\mathcal{B}_{k,p-1}(\xi) + \frac{1}{2}(1+\xi)\mathcal{B}_{k-1,p-1}(\xi), \tag{2.9}$$

where

$$\mathcal{B}_{1,0}(\xi) \equiv 1, \tag{2.10}$$

and

$$\mathcal{B}_{k,p}(\xi) \equiv 0 \qquad \text{if} \quad k < 1 \quad \text{or} \quad k > p+1. \ . \tag{2.11}$$

By virtue of knot insertion, which increases the multiplicity of the knots without changing the geometric and parametric properties of the curve [22], Bézier elements of a NURBS can be computed. In this regard, the multiplicity of each interior knot is increased to the order of the knot vector, p. Noteworthy is that the required multiplicity for this purpose was originally $p+1$, while increasing the multiplicity to p also suffices. This will cause the neighboring Bézier elements to share control points, which consequently reduces the computational cost [22].

To compute Bézier extraction operator for a NURBS, we shall first define the new set of control points. For a given knot vector $\Xi = \{\xi_1, \xi_2, \cdots, \xi_{n+p+1}\}$, a new knot $\bar{\xi} \in [\xi_r, \xi_{r+1}[$ with $r > p$ can be inserted in the knot vector such as $\Xi = \{\xi_1, \cdots, \xi_r, \bar{\xi}, \xi_{r+1}, \cdots, \ \xi_{n+p+1}\}$ with $n+1$ new basis functions defined on Equations (2.3) and (2.4). Accordingly, the new number of knot vectors is $m = n+1$, and the new set of control points $\bar{\mathbf{P}}_{k=1}^{m}$ are defined by [22],

$$\bar{\mathbf{P}}_k = \begin{cases} \mathbf{P}_1, & k = 1, \\ \varphi_k \mathbf{P}_k + (1-\varphi_k)\mathbf{P}_{k-1}, & 1 < k < m, \\ \mathbf{P}_n, & k = m, \end{cases} \tag{2.12}$$

where

$$\varphi_k = \begin{cases} 1, & 1 \le k \le r-p, \\ \frac{\bar{\xi}-\xi_k}{\xi_{k+p}-\xi_k}, & r-p+1 \le k \le r, \\ 0, & k \ge r+1. \end{cases} \tag{2.13}$$

For a general case where $\{\bar{\xi}_1, \bar{\xi}_2, \cdots, \bar{\xi}_m\}$ is the new set of knots required for Bézier

decomposition, equation (2.13) can be defined for each new knot $\bar{\xi}_j, j = 1, 2, \cdots, m$ as φ_k^j where $k = 1, 2, \cdots, n+j$. The Bézier extraction operator can be defined as [22]:

$$\mathbf{C}^j = \begin{bmatrix} \varphi_1 & 1-\varphi_2 & 0 & \cdots & & & 0 \\ 0 & \varphi_2 & 1-\varphi_3 & 0 & \cdots & & 0 \\ 0 & 0 & \varphi_3 & 1-\varphi_4 & 0 & \cdots & 0 \\ \vdots & & & & & & \\ 0 & \cdots & & & 0 & \varphi_{(n+j-1)} & \varphi_{(n+j)} \end{bmatrix}. \tag{2.14}$$

In a similar fashion, Equation (2.12) can be rewritten in recursive manner with the initial value $\bar{\mathbf{P}}^1 = \mathbf{P}$.

$$\bar{\mathbf{P}}^{j+1} = (\mathbf{C}^j)^{\mathrm{T}} \bar{\mathbf{P}}^j. \tag{2.15}$$

The Bézier element decomposition can be defined as the final set of control points ($j = m$), letting $\mathbf{P}^b = \bar{\mathbf{P}}^{m+1}$ and $\mathbf{C}^{\mathrm{T}} = \left(\mathbf{C}^1 \cdots \mathbf{C}^{m-1}\mathbf{C}^m\right)^{\mathrm{T}}$:

$$\mathbf{P}^b = \mathbf{C}^{\mathrm{T}}\mathbf{P}. \tag{2.16}$$

Applying Equation (2.16) in Equation (2.2), with $\boldsymbol{\mathcal{B}}(\xi)$ the Bernstein polynomial, we have:

$$\mathbf{x}(\xi) = (\mathbf{P}^b)^{\mathrm{T}}\boldsymbol{\mathcal{B}}(\xi) = (\mathbf{C}^{\mathrm{T}}\mathbf{P})^{\mathrm{T}}\boldsymbol{\mathcal{B}}(\xi) = \mathbf{P}^{\mathrm{T}}\mathbf{C}\boldsymbol{\mathcal{B}}(\xi) = \mathbf{P}^{\mathrm{T}}\mathbf{N}(\xi). \tag{2.17}$$

Hence, the new basis function $\mathbf{N}(\xi)$ defined over a knot vector for a B-spline curve is presented as:

$$\mathbf{N}(\xi) = \mathbf{C}\boldsymbol{\mathcal{B}}(\xi). \tag{2.18}$$

2.1.4 Bézier extraction for NURBS

Recalling the Equation (2.6), the only difference between B-spline and NURBS curves is the weights used in the NURBS basis function. Therefore, in order to provide a Bézier element based NURBS formulation we need to redefine the weights as [22]:

$$\begin{aligned} W(\xi) = \sum_{k=1}^{n} N_k(\xi) w_k = \mathbf{w}^{\mathrm{T}}\mathbf{N}(\xi) = \mathbf{w}^{\mathrm{T}}\mathbf{C}\boldsymbol{\mathcal{B}}(\xi) = \\ \left(\mathbf{C}^{\mathrm{T}}\mathbf{w}\right)^{\mathrm{T}}\boldsymbol{\mathcal{B}}(\xi) = \left(\mathbf{w}^b\right)^{\mathrm{T}}\boldsymbol{\mathcal{B}}(\xi) = W^b(\xi) \end{aligned} \tag{2.19}$$

with $\mathbf{w}$ the vector associated with the weights in the diagonal matrix of weights, $\mathbf{w} = \{w_k\}_{k=1}^n$. Thus, in the same manner $\mathbf{w}^b = \{w_k^b\}_{k=1}^{n+m}$ and $\mathbf{W}^b$ is the corresponding diagonal matrix of

weights.

Combining Equations (2.5), (2.6) and (2.19) and applying them in the Bézier extraction operator yields:

$$\begin{aligned}\mathbf{T}(\xi) = \sum_{k=1}^{n} R_k(\xi)\mathbf{P}_k = \mathbf{P}^{\mathrm{T}}\mathbf{R}(\xi) = \frac{1}{W^b(\xi)}\mathbf{P}^{\mathrm{T}}\mathbf{W}\mathbf{N}(\xi) = \\ \frac{1}{W^b(\xi)}\mathbf{P}^{\mathrm{T}}\mathbf{W}\mathbf{C}\boldsymbol{\mathcal{B}}(\xi) = \frac{1}{W^b(\xi)}\left(\mathbf{C}^{\mathrm{T}}\mathbf{W}\mathbf{P}\right)^{\mathrm{T}}\boldsymbol{\mathcal{B}}(\xi).\end{aligned} \tag{2.20}$$

Inserting $\mathbf{W}^b$ into Equation (2.20), $\mathbf{T}(\xi)$ becomes:

$$\mathbf{T}(\xi) = \frac{1}{W^b(\xi)}\left(\mathbf{W}^b\mathbf{P}^b\right)^{\mathrm{T}}\boldsymbol{\mathcal{B}}(\xi) = \sum_{k=1}^{n+m}\frac{\mathbf{P}_k^b w_k^b \mathcal{B}_k(\xi)}{W^b(\xi)} \tag{2.21}$$

with:

$$\mathbf{P}^b = (\mathbf{W}^b)^{-1}\mathbf{C}^T\mathbf{W}\mathbf{P}. \tag{2.22}$$

Finally, the elementwise NURBS-based basis function in terms of the Bézier extraction operator $\mathbf{C}$ and Bernstein polynomial $\boldsymbol{\mathcal{B}}$ yields

$$\mathbf{R}^e(\xi) = \mathbf{W}^e\frac{\mathbf{N}^e(\xi)}{W^e(\xi)} = \left(\mathbf{W}^b\right)^e\mathbf{C}^e\frac{\boldsymbol{\mathcal{B}}^e(\xi)}{(W^b)^e(\xi)} \tag{2.23}$$

where e denotes the element under consideration. Figure 2.1 illustrates the effect of Bézier extraction on the Gaussian quadrature schemes used in IGA. A standard mapping similar to customary finite element approach is observed, while two pull backs are utilised in the classical approach in the absence of Bézier extraction.

Following Equation (2.8), a bivariate NURBS can be obtained by tensor product of two univariate NURBS, and the derivatives of the bivariate Bézier-based NURBS basis function read:

$$\frac{\partial\mathbf{R}^e(\boldsymbol{\xi})}{\partial\xi_i} = \mathbf{W}^e\mathbf{C}^e\left(\frac{1}{W^b(\boldsymbol{\xi})}\frac{\partial\boldsymbol{\mathcal{B}}^e(\boldsymbol{\xi})}{\partial\xi_i} - \frac{\partial W^b(\boldsymbol{\xi})}{\partial\xi_i}\frac{\boldsymbol{\mathcal{B}}^e(\boldsymbol{\xi})}{\left(W^b(\boldsymbol{\xi})\right)^2}\right). \tag{2.24a}$$

$$\begin{aligned}\frac{\partial^2\mathbf{R}^e(\boldsymbol{\xi})}{\partial\xi_i\partial\xi_j} = \mathbf{W}^e\mathbf{C}^e\left(\frac{1}{W^b(\boldsymbol{\xi})}\frac{\partial^2\boldsymbol{\mathcal{B}}^e(\boldsymbol{\xi})}{\partial\xi_i\xi_j} - \frac{1}{\left(W^b(\boldsymbol{\xi})\right)^2}\frac{\partial W^b(\boldsymbol{\xi})}{\partial\xi_j}\frac{\partial\boldsymbol{\mathcal{B}}^e(\boldsymbol{\xi})}{\partial\xi_i} - \frac{1}{\left(W^b(\boldsymbol{\xi})\right)^2}\frac{\partial W^b(\boldsymbol{\xi})}{\partial\xi_i}\frac{\partial\boldsymbol{\mathcal{B}}^e(\boldsymbol{\xi})}{\partial\xi_j}\right. \\ \left. - \frac{\partial^2 W^b(\boldsymbol{\xi})}{\partial\xi_i\partial\xi_j}\frac{\boldsymbol{\mathcal{B}}^e(\boldsymbol{\xi})}{\left(W^b(\boldsymbol{\xi})\right)^2} + 2\frac{\partial W^b(\boldsymbol{\xi})}{\partial\xi_j}\frac{\partial W^b(\boldsymbol{\xi})}{\partial\xi_i}\frac{\boldsymbol{\mathcal{B}}^e(\boldsymbol{\xi})}{\left(W^b(\boldsymbol{\xi})\right)^3}\right)\end{aligned} \tag{2.24b}$$

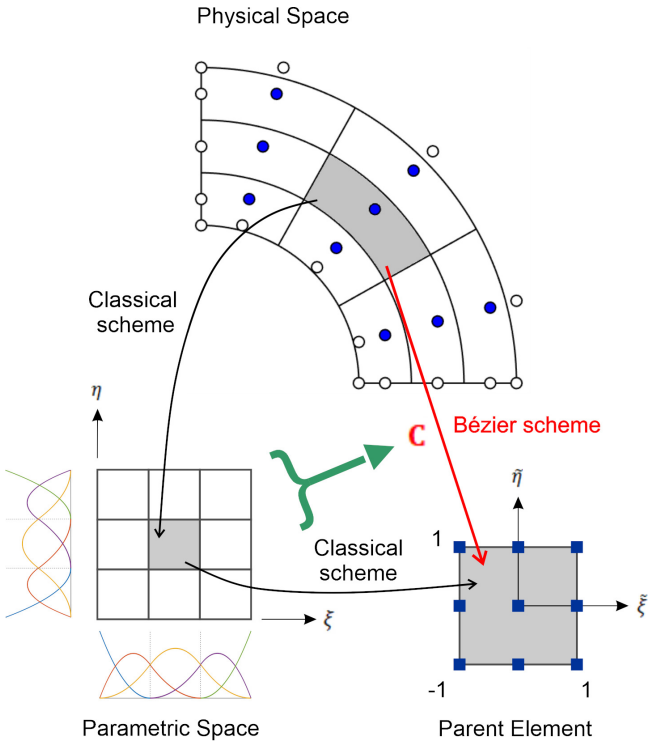

Figure 2.1: The elementwise mapping by virtue of Bézier extraction. A direct pull back from the physical space to the parent element is illustrated where Bézier extraction operator $\mathbf{C}$ contains the parametric space information. The classical approach entails two pull backs, where parametric space serves as the intermediary between the physical space and the parent element.

where $\boldsymbol{\xi} = \{\xi_1, \xi_2, \cdots\} = \{\xi, \eta, \cdots\}$ and $i, j = 1, 2, \cdots, n_{dim}$. n_{dim} is the number of dimensions, two for a bivariate NURBS. The derivatives of the weighted function in Equations (2.24a) and (2.24b) are:

$$\frac{\partial W^b(\boldsymbol{\xi})}{\partial \xi_i} = \mathbf{w}^e \mathbf{C}^e \frac{\partial \boldsymbol{\mathcal{B}}^e(\boldsymbol{\xi})}{\partial \xi_i} \tag{2.25a}$$

$$\frac{\partial^2 W^b(\boldsymbol{\xi})}{\partial \xi_i \partial \xi_j} = \mathbf{w}^e \mathbf{C}^e \frac{\partial^2 \boldsymbol{\mathcal{B}}^e(\boldsymbol{\xi})}{\partial \xi_i \partial \xi_j} \tag{2.25b}$$

where $\boldsymbol{\mathcal{B}}$ is the bivariate basis functions of Bernstein polynomials,

$$\mathcal{B}^{p,q}_{k,l}(\xi, \eta) = \mathcal{B}_{k,p}(\xi) \otimes \mathcal{B}_{l,q}(\eta). \tag{2.26}$$

The derivatives of Bernstein basis functions are used in the derivatives of the weighted function, which are defined as

$$\frac{\partial \mathcal{B}_{k,l}^{p,q}(\xi,\eta)}{\partial \xi} = \frac{1}{2} p \left\{ \mathcal{B}_{k-1,p-1}(\xi) + \mathcal{B}_{k,p-1}(\xi) \right\} \otimes \mathcal{B}_{l,q}(\eta) \tag{2.27a}$$

$$\frac{\partial \mathcal{B}_{k,l}^{p,q}(\xi,\eta)}{\partial \eta} = \frac{1}{2} q \mathcal{B}_{k,p}(\xi) \otimes \left\{ \mathcal{B}_{l-1,q-1}(\eta) + \mathcal{B}_{l,q-1}(\eta) \right\} \tag{2.27b}$$

$$\frac{\partial^2 \mathcal{B}_{k,l}^{p,q}(\xi,\eta)}{\partial \xi^2} = \frac{1}{4} p(p-1) \left\{ \mathcal{B}_{k-2,p-2}(\xi) - 2\mathcal{B}_{k-1,p-2}(\xi) + \mathcal{B}_{k,p-2}(\xi) \right\} \otimes \mathcal{B}_{l,q}(\eta) \tag{2.27c}$$

$$\frac{\partial^2 \mathcal{B}_{k,l}^{p,q}(\xi,\eta)}{\partial \eta^2} = \frac{1}{4} q(q-1) \mathcal{B}_{k,p}(\xi) \otimes \left\{ \mathcal{B}_{l-2,q-2}(\eta) - 2\mathcal{B}_{l-1,q-2}(\eta) + \mathcal{B}_{l,q-2}(\eta) \right\} \tag{2.27d}$$

$$\frac{\partial^2 \mathcal{B}_{k,l}^{p,q}(\xi,\eta)}{\partial \xi \partial \eta} = \frac{\partial^2 \mathcal{B}_{k,l}^{p,q}(\xi,\eta)}{\partial \eta \partial \xi} = \frac{1}{4} pq \left\{ \mathcal{B}_{k-1,p-1}(\xi) + \mathcal{B}_{k,p-1}(\xi) \right\} \otimes \left\{ \mathcal{B}_{l-1,q-1}(\eta) + \mathcal{B}_{l,q-1}(\eta) \right\}. \tag{2.27e}$$

2.1.5 Point Projection

In cohesive fracture, a line integration is required to integrate the traction which acts at the discontinuity. Gauss integration is used for this purpose. As observed in Figure 2.1, Bézier extraction maps a point in the physical space onto the parameter domain in the Bernstein parent element. Nevertheless, finding the corresponding natural coordinates of a physical known point necessitates a point projection [100], see Figure 2.2. Herein, a Newton-Raphson scheme has been utilised for the point projection algorithm.

(1) Define the curve in terms of natural coordinates $C(\xi,\eta) = \sum_{i=1}^{n} R_i(\xi,\eta) X_i$ where n and X are the number and location of control points for an element, respectively, and R is the basis function of a NURBS.

(2) Define the residual $r(\xi,\eta) = C(\xi,\eta) - P(x,y)$, see Figure 2.2.

(3) Solve $J_j \delta_j = \kappa_j$

$$J_j = \begin{bmatrix} f_{,\xi} & f_{,\eta} \\ g_{,\xi} & g_{,\eta} \end{bmatrix} = \begin{bmatrix} |C_{,\xi}|^2 + r \cdot C_{,\xi\xi} & C_{,\xi} \cdot C_{,\eta} + r \cdot C_{,\xi\eta} \\ C_{,\xi} \cdot C_{,\eta} + r \cdot C_{,\xi\eta} & |C_{,\eta}|^2 + r \cdot C_{,\eta\eta} \end{bmatrix} \tag{2.28}$$

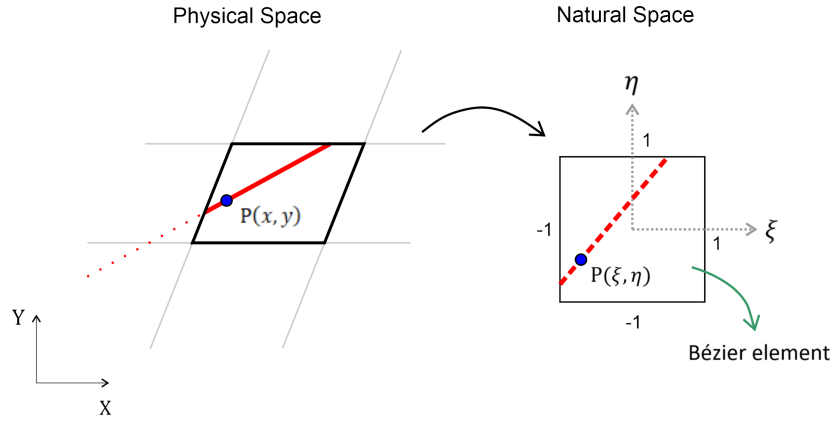

Figure 2.2: Finding ξ and η which correspond to the known physical point $\mathrm{P}(x, y)$ along the crack.

$$\delta_j = \begin{bmatrix} \Delta\xi \\ \Delta\eta \end{bmatrix} = \begin{bmatrix} \xi_{j+1} - \xi_j \\ \eta_{j+1} - \eta_j \end{bmatrix} \tag{2.29}$$

$$\kappa_j = - \begin{bmatrix} f(\xi_j, \eta_j) \\ g(\xi_j, \eta_j) \end{bmatrix} \tag{2.30}$$

where

$$f(\xi,\eta) = r(\xi,\eta).C_{,\xi}\,(\xi,\eta) = \left(\sum_{i=1}^{n} R_i(\xi,\eta)X_i - P(x,y)\right) \cdot \sum_{i=1}^{n} \frac{\partial R_i(\xi,\eta)}{\partial \xi} X_i \tag{2.31a}$$

$$g(\xi,\eta) = r(\xi,\eta).C_{,\eta}\,(\xi,\eta) = \left(\sum_{i=1}^{n} R_i(\xi,\eta)X_i - P(x,y)\right) \cdot \sum_{i=1}^{n} \frac{\partial R_i(\xi,\eta)}{\partial \eta} X_i \tag{2.31b}$$

$$|C_{,\xi}\,|^2 + r \cdot C_{,\xi\xi} = |\sum_{i=1}^{n} \frac{\partial R_i(\xi,\eta)}{\partial \xi} X_i|^2 + \left(\sum_{i=1}^{n} R_i(\xi,\eta)X_i - P(x,y)\right) \cdot \sum_{i=1}^{n} \frac{\partial^2 R_i(\xi,\eta)}{\partial \xi^2} X_i \tag{2.32a}$$

$$C_{,\xi}\cdot C_{,\eta}+r\cdot C_{,\xi\eta}=\sum_{i=1}^{n}\frac{\partial R_i(\xi,\eta)}{\partial\xi}X_i\cdot\sum_{i=1}^{n}\frac{\partial R_i(\xi,\eta)}{\partial\eta}X_i+\left(\sum_{i=1}^{n}R_i(\xi,\eta)X_i-P(x,y)\right)\cdot\sum_{i=1}^{n}\frac{\partial^2 R_i(\xi,\eta)}{\partial\xi\partial\eta}X_i \tag{2.32b}$$

$$|C_{,\eta}|^2+r\cdot C_{,\eta\eta}=|\sum_{i=1}^{n}\frac{\partial R_i(\xi,\eta)}{\partial\eta}X_i|^2+\left(\sum_{i=1}^{n}R_i(\xi,\eta)X_i-P(x,y)\right)\cdot\sum_{i=1}^{n}\frac{\partial^2 R_i(\xi,\eta)}{\partial\eta^2}X_i \tag{2.32c}$$

(4) Check the criterion for convergence:

$$res_1=|(\Delta\xi)C_{,\xi}(\xi,\eta)+\Delta\eta)C_{,\eta}(\xi,\eta)| \tag{2.33}$$

$$res_2=|r(\xi,\eta)| \tag{2.34}$$

$$res_3=\frac{|C_{,\xi}(\xi,\eta)\cdot r(\xi,\eta)|}{|C_{,\xi}(\xi,\eta)||r(\xi,\eta)|} \tag{2.35a}$$

$$res_4=\frac{|C_{,\eta}(\xi,\eta)\cdot r(\xi,\eta)|}{|C_{,\xi}(\xi,\eta)||r(\xi,\eta)|} \tag{2.35b}$$

IF $res_1\le\epsilon_1$ OR $res_2\le\epsilon_1$ OR $res_3\le\epsilon_2$ and $res_4\le\epsilon_2$

- ξ_j,η_j are accepted as final solution

ELSE

- Calculation continues for $j+1$ with two new criterion

  IF $\xi_j<-1$

  - set $\xi_j=1-(-1-\xi_j)$

  ELSEIF $\xi_j>1$

  - set $\xi_j=-1+(\xi_j-1)$

  END

IF $\eta_j < -1$
• set $\eta_j = 1 - (-1 - \eta_j)$
ELSEIF $\eta_j > 1$
• set $\eta_j = -1 + (\eta_j - 1)$
END

• Return to (1)
END

2.2 Generalised/eXtended Finite Element Analysis

The partition of unity property holds for Lagrange interpolation functions, typically used within standard finite element methods, as well as for B-splines and NURBS, which are the prototypical basis functions used in isogeometric analysis. Exploiting this property the total displacement field can be written as the sum of two sub-fields, as follows:

$$u(\mathbf{x}) = \sum_{i=1}^{n} \Psi_i(\mathbf{x}) \left(a_i + \sum_{j=1}^{m} b_{ij} \Upsilon_j(\mathbf{x}) \right) \tag{2.36}$$

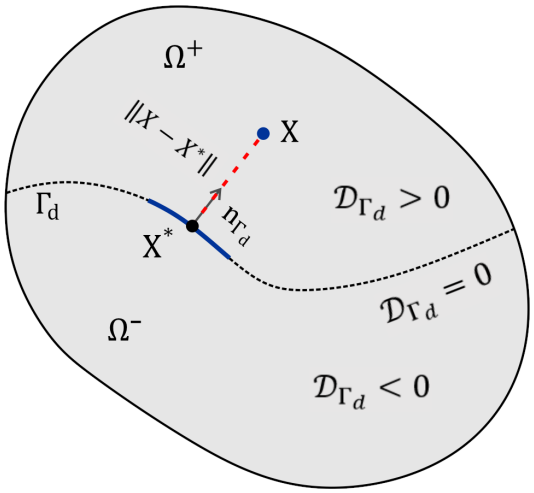

Figure 2.3: Determination of the signed distance. The point $\mathbf{X}^*$ is the closest projection of the point $\mathbf{X}$ onto the discontinuity Γ_d.

In Equation (2.36), Ψ_i are the regular basis functions, Υ_j is an enriched basis with m terms, a_i and b_{ij} are the regular and the enhanced nodal degrees of freedom, respectively. For the purpose pursued in this thesis a single additional term suffices, so that $m = 1$. However, cases with $m > 1$ have been studied [112, 146] for different reasons, including robust conditioning or an improved convergence rate. In standard finite element methods,

the enhanced basis is empty, unlike in eXtended or Generalised Finite Element methods (XFEM or GFEM) in order to improve the approximation. Employing a standard finite element notation for an n-noded element with one enriched term, Equation (2.36) can be written in matrix-vector form as:

$$\mathbf{u}(\mathbf{x}) = \mathbf{N}(\mathbf{x})\mathbf{a} + \tilde{\mathbf{N}}(\mathbf{x})\mathbf{N}_{\gamma}(\mathbf{x})\mathbf{H}\mathbf{b} \tag{2.37}$$

where $\mathbf{N}$ contains the standard finite element shape functions and $\mathbf{N}_{\gamma}$ is the matrix which contains the enhancement, while $\mathbf{a}$ and $\mathbf{b}$ are the regular and enhanced degrees of freedom, respectively. To generalise the formulation, a different set of basis functions $\tilde{\mathbf{N}}$ has been used in the extended part. $\mathbf{H}$ is a diagonal matrix to include or remove enriched nodes by switching the corresponding diagonal entries between 0 and 1, so that Equation (2.37) implies a bijective relation between the standard and enhanced degrees of freedom for each node which enables activation or deactivation of the enriched part [131]. This feature provides a conventional finite element displacement field with a customised local enrichment.

2.2.1 Level-set technique

As not uncommon in extended finite element methods, we have adopted level sets for tracking the crack as a moving interface [127, 17, 92, 129]. A zero level set denotes the interface itself and higher levels represent the propagation of the interface. This eliminates the necessity to explicitly define the interface geometry. The most common level set function is the signed distance defining the position of an arbitrary point with respect to the interface, see Figure 2.3 [77]:

$$\mathcal{D}_{\Gamma_d}(\mathbf{x}) = \|\mathbf{x} - \mathbf{x}^*\| \ \text{sign}\left(\mathbf{n}_{\Gamma_d} \cdot (\mathbf{x} - \mathbf{x}^*)\right) \tag{2.38}$$

where $\|\cdot\|$ denotes the Euclidean norm, $\mathbf{x}^*$ is the closest projection of point $\mathbf{x}$ onto the interface, and $\mathbf{n}_{\Gamma_d}$ is the normal vector at point $\mathbf{x}^*$ on the interface. Based on Equation (2.38), the level set function divides the domain into three zones:

$$\mathcal{D}_{\Gamma_d}(\mathbf{x}) = \begin{cases} -\|\mathbf{x} - \mathbf{x}^*\| & \text{if} \quad \mathbf{x} \in \Omega^- \\ 0 & \text{if} \quad \mathbf{x} \in \Gamma_d \\ +\|\mathbf{x} - \mathbf{x}^*\| & \text{if} \quad \mathbf{x} \in \Omega^+ \end{cases} \tag{2.39}$$

2.2.2 Physics of discontinuity: strong and weak enrichments

The choice for the (discontinuous) enrichment function differs depending on the physics of discontinuity. Two main groups are common in this regard: strong and weak discontinuities. The main difference between these two approaches lies in the continuity of the displacement field for weak discontinuities, while it is discontinuous for the strong discontinuity, see Figure

2.4. For the displacement gradients, however, both of these approaches lead to a discontinuous strain field. Using the sign function defined in Equation (2.38) the Heaviside function adopted in this paper is defined as:

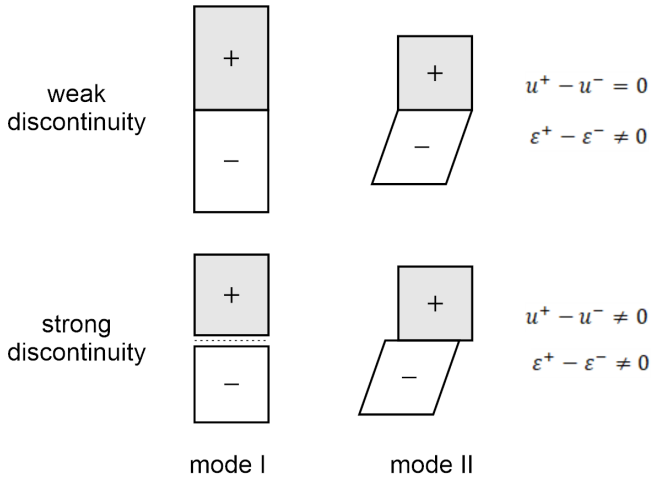

Figure 2.4: Weak and strong discontinuities. Top row illustrates the weak discontinuity, where a continuous displacement is joined by a discontinuous strain field ε. For the strong discontinuity, however, both displacement field and its gradient are discontinuous, shown at the bottom row.

$$\mathcal{H}_{\Gamma_d}(\mathbf{x}) = \mathbf{n}_{\Gamma_d} \cdot \nabla \mathcal{D}_{\Gamma_d}(\mathbf{x}) = \begin{cases} -1 & \text{if} \quad \mathcal{D}_{\Gamma_d}(\mathbf{x}) < 0 \\ 0 & \text{if} \quad \mathcal{D}_{\Gamma_d}(\mathbf{x}) = 0 \\ +1 & \text{if} \quad \mathcal{D}_{\Gamma_d}(\mathbf{x}) > 0 \end{cases} \tag{2.40}$$

Herein, a crack is considered, which is modelled as a strong discontinuity, but weak discontinuities can be modelled as well [51, 77].

2.2.3 Cohesive-zone model

In this thesis we adopt the cohesive crack concept, in which the inelastic deformations in the fracture process zone are cast in the form of tractions concentrated in a fictitious extention of the crack line.

Traction-separation relation

Mode-I will be the governing fracture mode considered in the ensuing chapters. It is assumed that the tractions normal to a discontinuity can be captured using an exponential decay function of the crack opening:

$$\mathbf{t}_n^{\text{loc}} = f_t \exp\left(-\frac{f_t}{G_f}\kappa\right). \tag{2.41}$$

where κ denotes the history parameter, f_t indicates the (tensile) fracture strength and G_f is the fracture energy. A Kuhn-Tucker condition governs the loading/unloading conditions:

$$f\left(\llbracket u_n \rrbracket, \kappa\right) = \llbracket u_n \rrbracket - \kappa \leq 0 \qquad \dot{\kappa} \geq 0 \qquad \dot{\kappa} f = 0 \tag{2.42}$$

where $\llbracket u_n \rrbracket$ is the normal displacement jump. By differentiating Equation 2.41 with respect to time, the normal cohesive tangent in the local coordinates results,

$$\mathbf{T}_d = -\frac{f_{\mathrm{t}}^2}{G_{\mathrm{f}}} \exp\left(-\frac{f_{\mathrm{t}}}{G_{\mathrm{f}}}\kappa\right). \tag{2.43}$$

A secant stiffness is assumed for unloading.

Since the traction-relative displacement relation is cast in a local coordinate frame, a transformation to global coordinates is necessary:

$$\mathbf{t}_n = \mathbf{Q}^{\mathrm{T}} \cdot \mathbf{t}_n^{\mathrm{loc}}\left(\llbracket u_n \rrbracket, \kappa\right) \tag{2.44}$$

where $\mathbf{Q} = (\mathbf{s}_{\Gamma_d}, \mathbf{n}_{\Gamma_d})$ is the rotation matrix, and $\mathbf{s}_{\Gamma_d}$ indicates the tangential vector at the discontinuity. Next, this is belinearised for use in a Newton-Raphson iterative scheme. To obtain a symmetric tangent stiffness matrix the shear stiffness must be neglected, which is permissible in mode-I dominated fracture problems.

2.2.4 Direction of the extension of the discontinuity

Even though isogeometric analysis vastly improves the stress prediction [22], particularly compared to Lagrange polynomials, the direction of crack propagation can be highly influenced by small accuracies in the principal stresses, which determine the crack extension. This local distribution of stresses varies significantly in the vicinity of the crack tip, suggesting a smoothing scheme to be employed. Therefore, a nonlocal approximation of the stresses around the crack tip is adopted, similar to the approach considered earlier in XFEM [144]. It is emphasised that only Gauss points in front of the crack tip are considered, i.e. the red-coloured Gauss points in Figure 2.5. The Gaussian distribution function is used as the weighting function for the nonlocal approximation [73]:

$$w = \frac{1}{(2\pi)^{3/2} l^3} \exp\left(-\frac{r^2}{2l^2}\right) \tag{2.45}$$

where r and l are the distance vector of each Gauss point and a length parameter, respectively, see Figure 2.5. The length parameter is typically taken 2-3 times the length of a diagonal of a typical element [144]. From the physics viewpoint, the length parameter is related to the micro-structure of a material. It is, for instance, defined as inter-atomic spacing for gradient-

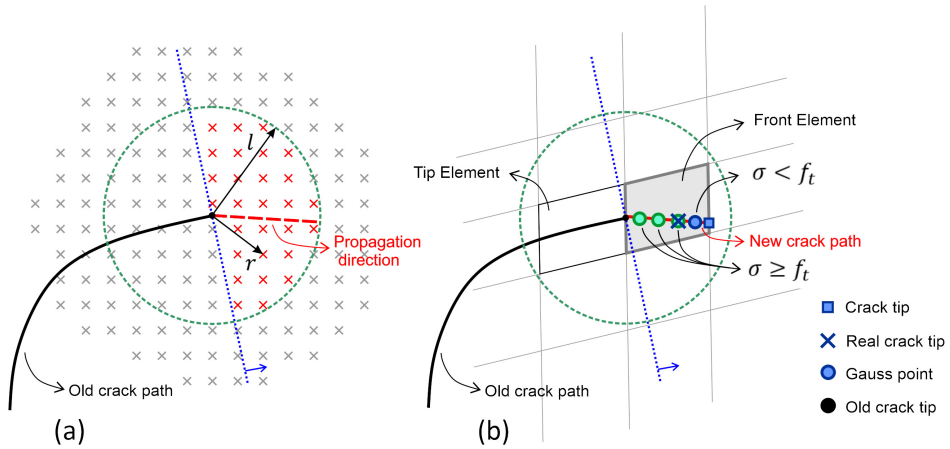

Figure 2.5: Nonlocal calculation of the crack propagation direction. The blue arrow illustrates the direction of the crack tip front. In (a), the green dashed circle determines the Gauss points considered for nonlocal computation, while red marks denotes the Gauss points used in the computation of the nonlocal stress. In (b), the crack tip and real crack tip are defined, which is determined by comparing the principal stress σ with the fracture strength f_t. They are different in the case that fracture criterion is not satisfied at the crack tip on the edge of the element, see the green marks on the crack path in (b) indicating a successful pass of the fracture criterion.

enhanced theories in carbon nanotubes [7]. Calculating the nonlocal stress components for the crack tip, the new crack propagation direction can be located based on the principal stresses (dashed red line in Figure 2.5). After determining the crack direction, the end point of the crack can be located, since the crack is assumed as a straight line passing throughout the element.

Chapter 3

Extended IsoGeometric Analysis for Cohesive Fracture

The objective of this chapter[1] is to present an extended isogeometric formulation for cohesive fracture. The approach exploits the higher-order inter-element continuity property of IsoGeometric Analysis (IGA), in particular the higher accuracy that results for the stress prediction, which yields an improved estimate for the direction of crack propagation compared to customary Lagrangian interpolations utilised in finite element method. Shifting technique is used to ensure compatibility with the surrounding discretisation, where, different from eXtended Finite Element Methods (XFEM), the affected elements stretch over several rows perpendicular to the crack path. To avoid fine meshes around the crack tip in case of cohesive fracture, a blending function is used in the extension direction of the crack path. To comply with standard finite element data structures Bézier extraction is used. The absence of the Kronecker-delta property in the higher continuity-orders of isogeometric analysis impedes the enrichment scheme and compatibility enforcement. These issues are studied comprehensively at the hand of several examples, while crack propagation analyses show the viability of the approach.

3.1 Research Background

Fracture is an important topic of study in the mechanics of solids and a good understanding is pivotal for the proper assessment of structural integrity. Fracture mechanics encompasses a wide spectrum of experimental and theoretical studies, and involves different physical phenomena. The fracture process-zone, a limited zone in front of the crack tip where inelastic

[1]This chapter is directly adopted from:

Fathi, F., Chen, L. and de Borst, R., 2020. Extended isogeometric analysis for cohesive fracture. International Journal for Numerical Methods in Engineering, 121(20), pp.4584-4613.

deformations take place, is an important concept, which is central in deciding which modelling approach should be adopted. When the size of the fracture process-zone is small compared to a typical structural dimension, Linear Elastic Fracture Mechanics (LEFM) [57, 69] is the method of choice. However, when the fracture process-zone becomes non-negligible, cohesive-zone models [10, 41, 64] are often more applicable from a physics point of view. This holds, for instance, for many problems in fractured, fluid-saturated porous media [107].

The incorporation of a displacement discontinuity like a crack, into a continuum mechanics framework can basically be accomplished in two different ways: either the discontinuity is captured rigorously and additional degrees of freedom are created, or the discontinuity is embedded in an element, and the displacement discontinuity is transformed into an additional, incompatible, Dirac-delta like strain mode inside an element [122], and different variants of this approach have been put forward. The downside of the latter approach, however, is that the discontinuity is not directly resolved. Moreover, although the approach mitigates the notorious mesh sensitivity issue in strain softening solids, the underlying issue of a loss of well-posedness of the boundary value problem is not solved [35].

Interface elements are the conventional way to capture a (potential) crack as an interelement discontinuity which fully preserves the discontinuous crack [114, 72, 141]. They are simple to implement and robust in terms of computational performance. Yet, the approach suffers from the need to know the crack direction beforehand. Re-meshing is an obvious remedy and has been applied successfully, including in cohesive fracture [28, 29, 27].

In a different approach, an arbitrarily shaped discontinuity can be inserted by adding an additional set of discontinuous functions with own degrees of freedom to the regular displacement field by exploiting the partition of unity property of finite element basis functions. This method has been coined the eXtended Finite Element Method (XFEM) and can be considered as a generalisation of interface elements, as these elements are retrieved as the limiting case of XFEM when the discontinuity is put at the edge of an element. Yet, some major differences exist. First, crack propagation can be entirely arbitrary, free of the underlying, original mesh lay-out. Secondly, the dummy stiffness, which is needed in interface elements to keep the discontinuity closed prior to local crack initiation, is not needed in XFEM because locally new degrees of freedom are created only when the crack has propagated to this point, [35, 77, 93]. While the eXtended Finite Element Method was originally proposed in conjunction with Linear Elastic Fracture Mechanics [15, 91], applications of XFEM to cohesive-zone models have also been proposed [144, 145].

The latter contributions were also the first to utilise a higher-order XFEM for both the regular and the extended parts. Six-noded triangular elements were employed, even though the crack was still conceived as a set of straight discontinuities approximated with lines, which

restriction was dropped by Stazi *et al.* [126], who used a quadratic discretisation for the regular part and for approximating the geometry of the curved crack, while the interpolation of the extended part remained linear. A convergence study for higher-order extended finite element methods [83] showed that the same polynomial order has to be utilised in the standard as well as in the extended part in order to resolve the displacement field properly.

IsoGeometric Analysis (IGA) was proposed with the aim to have the same set of basis functions for the design process and for the analysis [30]. Aside from capturing the geometry exactly, the method has the major advantage that provides a higher-order inter-element continuity, enabling, for instance, to have a continuous stress field across element boundaries. The enhanced accuracy in stress prediction is particularly important in the vicinity of crack tips, where traditional Lagrange basis functions usually perform rather poorly. This is most relevant for free crack propagation, where the direction of crack extension is directly influenced by the accuracy of the local stress field.

An eXtended IsoGeometric Analysis method (XIGA) was first proposed by De Luycker *et al.* [39] for LEFM. Two types of continuity-orders were investigated: the same NURBS order for both parts, and a higher continuity-orders for the standard part combined with a linear interpolation for the extended part. Different from XFEM, XIGA cannot handle a linear interpolation in the extended part [39] when the standard part has a higher-order NURBS. Moreover, a conflict in the blending element where the tip and the Heaviside enrichments coincide, has been observed. As a remedy, $\mathcal{C}^0$-lines have been suggested for the standard as well as the extended part, such that Non-Uniform Rational B-splines (NURBS) reduce to Lagrange basis functions, or in other words, XIGA coincides with XFEM. As an alternative remedy, a least square technique was utilised in the weight (blending) functions for the tip and Heaviside enrichments. Convergence rates for the case of the same polynomial orders in the standard and extended parts have been reported by De Luycker *et al.* [39] and Ghorashi *et al.* [53].

Herein, an XIGA formulation is proposed for cohesive fracture. To enforce compatibility in the direction perpendicular to the crack path a shifting technique will be utilised. The use of shifting in isogeometric analysis is more complicated than in standard finite element analysis, as, due to the higher-order continuity, the area in which compatibility has to be enforced is several rows of elements wide instead of a single row. Another issue is the fact that the Kronecker delta property does not hold when using B-splines or Non-Uniform Rational B-Splines (NURBS), the basis functions in isogeometric analysis. In the direction of the crack, i.e. ahead of the crack tip, a blending technique has been used to avoid the required very fine meshes ahead of the crack tip, which is particularly relevant for cohesive fracture. Finally, to achieve compatibility with standard finite element data structures, Bézier extraction has

been used similar to an XIGA application in LEFM [123]. Rate-independent, isotropic linear elasticity has been used for the bulk material, while the displacement gradients are assumed to be small throughout.

This chapter continues with a succinct discussion of the strong and weak forms of the governing equations to set the scene for the ensuing discussion on a Bézier extraction based linearised discrete equations. Aspects of compatibility and implemenation are covered as well. Next is an assessment of the properties of the approach, including the effect of the NURBS order, and the order of the continuity. The chapter concludes with case studies of a plate with a circular void, and crack propagation along straight and curved paths.

3.2 Governing Equations

Kinematics of a discontinuity within a continuum formulation is now briefly discussed. The enhanced displacement field and the traction-separation relationship at the discontinuity are defined, followed by the derivation of the corresponding weak forms. The latter are the starting point for the discretisation in an isogeometric framework.

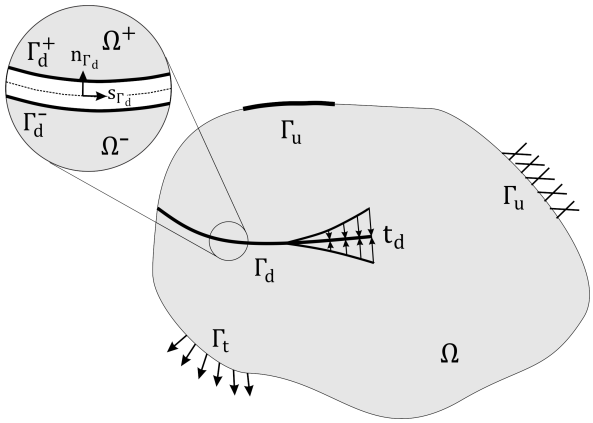

Figure 3.1: Body Ω with a discontinuity Γ_d.

As mentioned previously in Chapter 2, the partition of unity property holds for B-splines and NURBS, which are the prototypical basis functions used in isogeometric analysis. We consider the body of Figure 3.1. Recalling Equation (2.37) the regular degrees of freedom $\mathbf{a}$ represent the continuous displacement field, and the enhanced degrees of freedom $\mathbf{b}$ can represent a discontinuity in a displacement field:

$$\mathbf{u}(\mathbf{x}) = \mathbf{N}(\mathbf{x})\mathbf{a} + \mathcal{H}_{\Gamma_d}(\mathbf{x})\tilde{\mathbf{N}}(\mathbf{x})\mathbf{b}, \tag{3.1}$$

where $\mathbf{N}$ contains the standard finite element shape functions and $\tilde{\mathbf{N}}$ is the basis function

governing the enhanced section, different from the standard part. The matrix containing the enrichment function, defined as $\mathbf{N}_\gamma$ in Equation (2.37), is replaced by a Heaviside sign function $\mathcal{H}_{\Gamma_d}(\mathbf{x})$ to account for strong discontinuities. Recalling the small strain assumption, the strain field can be calculated by taking the gradient of Equation (3.1):

$$\boldsymbol{\epsilon} = \mathbf{B}\mathbf{a} + \mathcal{H}_{\Gamma_d}\tilde{\mathbf{B}}\mathbf{b} + 2\left(\delta_{\Gamma_d}\mathbb{n}_{\Gamma_d}\right)\tilde{\mathbf{N}}\mathbf{b}, \tag{3.2}$$

where $\tilde{\mathbf{B}}$ is the matrix of derivatives corresponding to the set of basis functions $\tilde{\mathbf{N}}$ in the extended part. δ_{Γ_d} is the Dirac-delta and $\mathbb{n}_{\Gamma_d}$ is the matrix containing the components of the normal vector to the discontinuity:

$$\mathbb{n}^{\mathrm{T}}_{\Gamma_d} = \begin{bmatrix} (n_{\Gamma_d})_x & 0 & (n_{\Gamma_d})_y \\ 0 & (n_{\Gamma_d})_y & (n_{\Gamma_d})_x \end{bmatrix}. \tag{3.3}$$

In the absence of the acceleration and body forces, the equilibrium equation reads:

$$\begin{cases} \nabla\cdot\boldsymbol{\sigma} = & 0 & \mathbf{x}\in\Omega \\ \mathbf{u} = & \overline{\mathbf{u}} & \mathbf{x}\in\Gamma_u \\ \mathbf{n}\cdot\boldsymbol{\sigma} = & \overline{\mathbf{t}} & \mathbf{x}\in\Gamma_t \\ \mathbf{n}_{\Gamma_d}\cdot\boldsymbol{\sigma} = & \mathbf{t}_d & \mathbf{x}\in\Gamma_d \end{cases}, \tag{3.4}$$

where $\boldsymbol{\sigma}$ is the Cauchy stress tensor, $\mathbf{n}$ is the normal vector to the external traction surface and $\mathbf{n}_{\Gamma_d}$ is the vector normal to the crack surface, see Figure 3.1. The prescribed displacement and traction are defined as $\overline{\mathbf{u}}$ and $\overline{\mathbf{t}}$, respectively. The stress-strain relation for the bulk material is assumed to be linear-elastic:

$$\boldsymbol{\sigma} = \mathbf{D} : \boldsymbol{\epsilon}, \tag{3.5}$$

where $\mathbf{D}$ is the fourth-order linear-elastic stiffness tensor.

3.2.1 Variational formulation

To generalise the variational formulation, η ($\hat{\eta}$ for standard and $\tilde{\eta}$ for extended part) is used to cover all admissible variables, including u. Employing the principle of virtual work, the equilibrium equation from (3.4) can be written in a weak form:

$$\int_\Omega \nabla^s\boldsymbol{\zeta} : \boldsymbol{\sigma}\mathrm{d}\Omega - \int_{\Gamma_t}\boldsymbol{\zeta}\cdot\bar{\mathbf{t}}\mathrm{d}\Gamma = 0 \tag{3.6}$$

which must hold for all admissible variations, and where in line with Equation (3.1), the variations of the displacement are decomposed into the regular displacement $\hat{\boldsymbol{\zeta}}$ and the dis-

placement jump $\tilde{\boldsymbol{\zeta}}$ as [144]:

$$\boldsymbol{\zeta} = \hat{\boldsymbol{\zeta}} + \mathcal{H}_{\Gamma_d}\tilde{\boldsymbol{\zeta}}. \tag{3.7}$$

Inserting Equation (3.7) into Equation (3.6) yields:

$$\int_\Omega \nabla^{\mathrm{s}}(\hat{\boldsymbol{\zeta}} + \mathcal{H}_{\Gamma_d}\tilde{\boldsymbol{\zeta}}) : \boldsymbol{\sigma}\mathrm{d}\Omega = \int_{\Gamma_u} (\hat{\boldsymbol{\zeta}} + \mathcal{H}_{\Gamma_d}\tilde{\boldsymbol{\zeta}}) \cdot \bar{\mathbf{t}}\mathrm{d}\Gamma. \tag{3.8}$$

The gradient of the displacement field in Equation (3.8) reads:

$$\nabla^{\mathrm{s}}\boldsymbol{\zeta} = \nabla^{\mathrm{s}}\hat{\boldsymbol{\zeta}} + \mathcal{H}_{\Gamma_d}(\nabla^{\mathrm{s}}\tilde{\boldsymbol{\zeta}}) + 2\delta_{\Gamma_d}(\tilde{\boldsymbol{\zeta}} \otimes \mathbf{n}_{\Gamma_d})^{\mathrm{s}}. \tag{3.9}$$

Inserting Equation (3.9) into Equation (3.8) and using the identity $\int_\Omega \delta_{\Gamma_d}(\mathbf{x})\phi(\mathbf{x})d\Omega = \int_\Gamma \phi(\mathbf{x})d\Gamma$, leads to the following weak form:

$$\int_\Omega \nabla^{\mathrm{s}}\hat{\boldsymbol{\zeta}} : \boldsymbol{\sigma}\mathrm{d}\Omega + \int_\Omega \mathcal{H}_{\Gamma_d}(\nabla^{\mathrm{s}}\tilde{\boldsymbol{\zeta}}) : \boldsymbol{\sigma}\mathrm{d}\Omega + 2\int_{\Gamma_d} \left(\tilde{\boldsymbol{\zeta}} \otimes \mathbf{n}_{\Gamma_d}\right)^{\mathrm{s}} : \boldsymbol{\sigma}\mathrm{d}\Gamma = \int_{\Gamma_u} (\hat{\boldsymbol{\zeta}} + \mathcal{H}_{\Gamma_d}\tilde{\boldsymbol{\zeta}}) \cdot \bar{\mathbf{t}}\mathrm{d}\Gamma, \tag{3.10}$$

where $\left(\tilde{\boldsymbol{\zeta}} \otimes \mathbf{n}_{\Gamma_d}\right) : \boldsymbol{\sigma}$ can be rewritten as $\tilde{\boldsymbol{\zeta}} \cdot (\boldsymbol{\sigma} \cdot \mathbf{n}_{\Gamma_d})$, which yields:

$$\int_\Omega \nabla^{\mathrm{s}}\hat{\boldsymbol{\zeta}} : \boldsymbol{\sigma}\mathrm{d}\Omega + \int_\Omega \mathcal{H}_{\Gamma_d}(\nabla^{\mathrm{s}}\tilde{\boldsymbol{\zeta}}) : \boldsymbol{\sigma}\mathrm{d}\Omega + 2\int_{\Gamma_d} \tilde{\boldsymbol{\zeta}} \cdot \mathbf{t}_d\mathrm{d}\Gamma = \int_{\Gamma_u} (\hat{\boldsymbol{\zeta}} + \mathcal{H}_{\Gamma_d}\tilde{\boldsymbol{\zeta}}) \cdot \bar{\mathbf{t}}\mathrm{d}\Gamma. \tag{3.11}$$

This results in two separate variational equations for $\hat{\zeta}$ and $\tilde{\zeta}$:

$$\int_\Omega \nabla^{\mathrm{s}}\hat{\boldsymbol{\zeta}} : \boldsymbol{\sigma}\mathrm{d}\Omega = \int_{\Gamma_u} \hat{\boldsymbol{\zeta}} \cdot \bar{\mathbf{t}}\mathrm{d}\Gamma \tag{3.12a}$$

$$\int_\Omega \mathcal{H}_{\Gamma_d}(\nabla^{\mathrm{s}}\tilde{\boldsymbol{\zeta}}) : \boldsymbol{\sigma}\mathrm{d}\Omega + 2\int_{\Gamma_d} \tilde{\boldsymbol{\zeta}} \cdot \mathbf{t}_d\mathrm{d}\Gamma = \int_{\Gamma_u} \mathcal{H}_{\Gamma_d}\tilde{\boldsymbol{\zeta}} \cdot \bar{\mathbf{t}}\mathrm{d}\Gamma. \tag{3.12b}$$

3.2.2 Linearised discretised equations

Substituting Equations (3.1) and (3.2) for the displacement and strain fields expressed in discrete values, into the weak forms of Equations (3.12a) and (3.12b), the discrete form of the equation of motion can be derived:

$$\int_\Omega \mathbf{B}^{\mathbf{T}}\boldsymbol{\sigma}\mathrm{d}\Omega = \int_{\Gamma_u} \mathbf{R}^{\mathbf{T}}\bar{\mathbf{t}}\mathrm{d}\Gamma \tag{3.13a}$$

$$\int_\Omega \mathcal{H}_{\Gamma_d}\tilde{\mathbf{B}}^{\mathbf{T}}\boldsymbol{\sigma}\mathrm{d}\Omega + 2\int_{\Gamma_d} \tilde{\mathbf{R}}^{\mathbf{T}}\mathbf{t}_d\mathrm{d}\Gamma = \int_{\Gamma_u} \mathcal{H}_{\Gamma_d}\tilde{\mathbf{R}}^{\mathbf{T}}\bar{\mathbf{t}}\mathrm{d}\Gamma. \tag{3.13b}$$

where $\mathbf{R}$ and $\mathbf{B}$ are the NURBS basis function and the corresponding strain-displacement matrix substituted for those from finite element in Equations (3.1) and (3.2), respectively.

Considering Equation (3.5), the stress in the bulk away from the discontinuity reads:

$$\boldsymbol{\sigma} = \mathbf{D}\boldsymbol{\epsilon} = \mathbf{D}\left(\mathbf{B}\mathbf{a} + \mathcal{H}_{\Gamma_d}\tilde{\mathbf{B}}\mathbf{b}\right) \tag{3.14}$$

and the traction at the discontinuity is defined in Equation (2.44) where the displacement jump based on the adopted Heaviside sign function in Equation (2.40) is:

$$[\![u_d]\!] = 2\sum_{k=1}^{n_{enr}} \tilde{R}_k(\xi) b_k \tag{3.15}$$

with n_{enr} the number of enriched nodes. $\tilde{R}_k$ is the NURBS set of basis functions corresponding to the extended part. Employing linearisation and discretisation results in the following matrix-vector equation:

$$\begin{bmatrix} \mathbf{K}_{\mathrm{aa}} & \mathbf{K}_{\mathrm{ab}} \\ \mathbf{K}_{\mathrm{ab}} & \mathbf{K}_{\mathrm{bb}} \end{bmatrix} \begin{bmatrix} \Delta\mathbf{a} \\ \Delta\mathbf{b} \end{bmatrix} = \begin{bmatrix} \mathbf{f}_{\mathrm{a}}^{\mathrm{ext}} \\ \mathbf{f}_{\mathrm{b}}^{\mathrm{ext}} \end{bmatrix} - \begin{bmatrix} \mathbf{f}_{\mathrm{a}}^{\mathrm{int}} \\ \mathbf{f}_{\mathrm{b}}^{\mathrm{int}} \end{bmatrix} \tag{3.16}$$

with the arrays

$$\mathbf{f}_{\mathrm{a}}^{\mathrm{ext}} = \int_{\Gamma_{\mathrm{u}}} \mathbf{R}^{\mathrm{T}}\bar{\mathbf{t}}\,\mathrm{d}\Gamma \tag{3.17a}$$

$$\mathbf{f}_{\mathrm{b}}^{\mathrm{ext}} = \int_{\Gamma_{\mathrm{u}}} \mathcal{H}_{\Gamma_d}\tilde{\mathbf{R}}^{\mathrm{T}}\bar{\mathbf{t}}\,\mathrm{d}\Gamma \tag{3.17b}$$

$$\mathbf{f}_{\mathrm{a}}^{\mathrm{int}} = \int_{\Omega} \mathbf{B}^{\mathrm{T}}\boldsymbol{\sigma}\,\mathrm{d}\Omega \tag{3.17c}$$

$$\mathbf{f}_{\mathrm{b}}^{\mathrm{int}} = \int_{\Omega} \mathcal{H}_{\Gamma_d}\tilde{\mathbf{B}}^{\mathrm{T}}\boldsymbol{\sigma}\,\mathrm{d}\Omega + 2\int_{\Gamma_d} \tilde{\mathbf{R}}^{\mathrm{T}}\mathbf{t}_d\,\mathrm{d}\Gamma \tag{3.17d}$$

and stiffness matrices:

$$\mathbf{K}_{\mathrm{aa}} = \int_{\Omega} \mathbf{B}^{\mathbf{T}}\mathbf{D}\mathbf{B}\mathrm{d}\Omega \tag{3.18a}$$

$$\mathbf{K}_{\mathrm{ab}} = \int_{\Omega} \mathcal{H}_{\Gamma_d}\mathbf{B}^{\mathbf{T}}\mathbf{D}\tilde{\mathbf{B}}\mathrm{d}\Omega \tag{3.18b}$$

$$\mathbf{K}_{\mathrm{ba}} = \int_{\Omega} \mathcal{H}_{\Gamma_d}\tilde{\mathbf{B}}^{\mathbf{T}}\mathbf{D}\mathbf{B}\mathrm{d}\Omega \tag{3.18c}$$

$$\mathbf{K}_{\mathrm{bb}} = \int_{\Omega} \tilde{\mathbf{B}}^{\mathrm{T}}\mathbf{D}\tilde{\mathbf{B}}\,\mathrm{d}\Omega + 4\int_{\Gamma_d} \tilde{\mathbf{R}}^{\mathrm{T}}\mathbf{Q}^{\mathrm{T}}\mathbf{T}_d\mathbf{Q}\tilde{\mathbf{R}}\,\mathrm{d}\Gamma \tag{3.18d}$$

while it is recalled that $\mathbf{Q}$ is the rotation matrix.

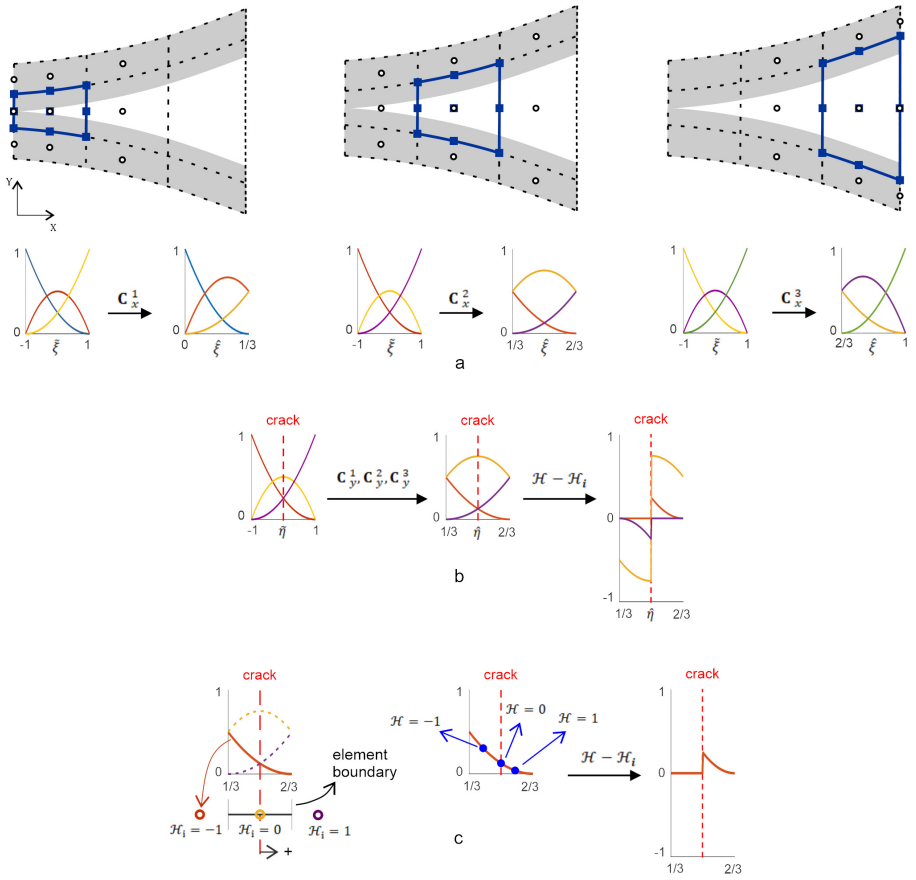

Figure 3.2: Effect of shifting on the basis functions for quadratic Bézier elements under mode-I fracture (a) in the X-direction and (b) in the Y-direction. The shifting technique is demonstrated in (c) where $\mathcal{H}$ corresponds to the Heaviside function of the Gauss point location and $\mathcal{H}_i$ indicates the Heaviside value for control points. The borders of each Bézier element is differentiated with the solid blue lines. ■ is the Bézier point, and ◯ indicates the control point. Only basis functions in the y-direction are affected by shifting. C is the Bézier extraction operator.

3.3 Compatibility Enforcement

Numerous contributions have been devoted on how to enforce compatibility of the standard and the enhanced displacement fields in the in XFEM [17, 93, 77]. Enforcing compatibility in XIGA, however, is a challenge which has hardly been addressed. Nevertheless, the issue is even more pressing, and complicated, due to the very reason that isogeometric analysis can enhance the order of continuity at element boundaries. De Luycker *et al.* [39] have studied the limitations and the difficulties of the blending technique in a comprehensive manner, but have mentioned another possible technique to enforce compatibility, namely *shifting*, only in passing. Herein, shifting technique is adopted to localise the effect of the enhanced region in

the direction normal to the crack profile, which is illustrated in Figure 3.2c for higher-order NURBS. Figure 3.2 illustrates the effect of the Bézier extraction operator on the Bernstein basis functions containing the discontinuity with shifting.

Remark 1: In this chapter, any continuity order is related to the element boundaries, unless mentioned otherwise. For example, $\mathcal{C}^0$ element is not necessarily linear order but all the continuity-orders with $\mathcal{C}^0$-continuity at element boundaries, e.g. $quadratic^0$ means a quadratic element with $\mathcal{C}^1$-continuity inside the element and $\mathcal{C}^0$-continuity at element boundaries.

Remark 2: B-splines generally do not provide Kronecker-delta property. However, similar to open knot vectors, Bézier B-spline elements partially provide this property at element boundaries. Therefore, *"weak Kronecker-delta property"* is aimed when Kronecker-delta property is utilised in the remainder of the chapter.

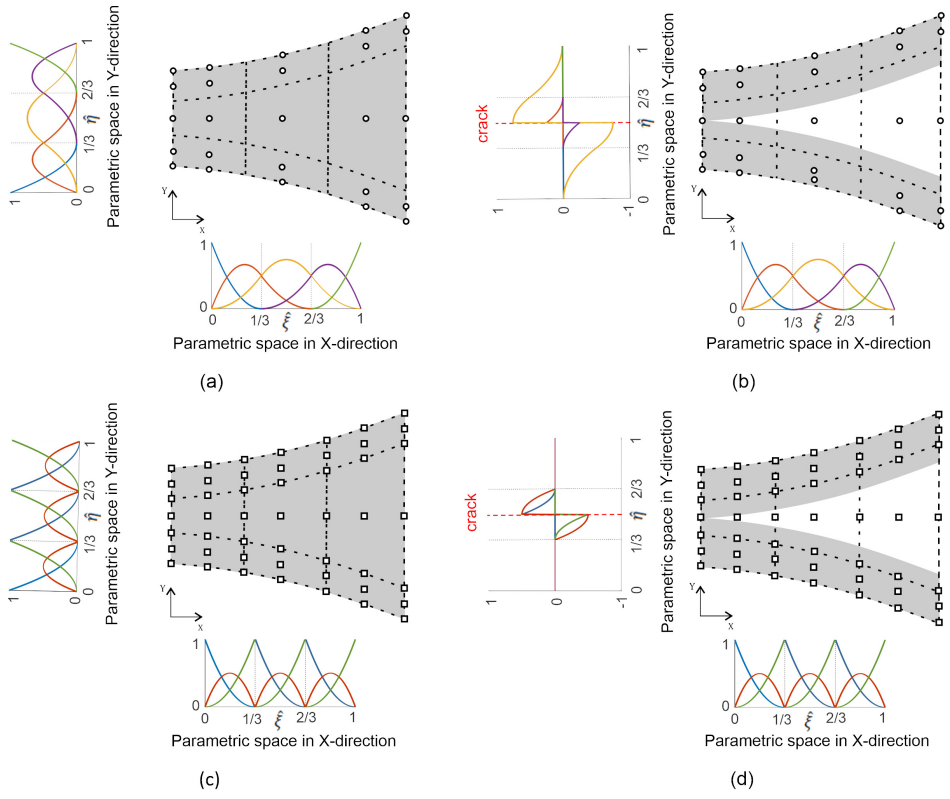

Figure 3.3: Comparison between control and Bézier points for a cracked set of quadratic elements: (a) regular basis functions for the control points, (b) extended basis functions for the control points, (c) regular basis functions for Bézier points and (d) extended basis functions for Bézier points. Here, (a) and (c) present the basis functions employed for the regular part in Equation (3.1), while (b) and (d) present the basis functions used for the extended part in Equation (3.1).

In conventional finite element methods the $\mathcal{C}^0$-continuity which underlies the Lagrangian

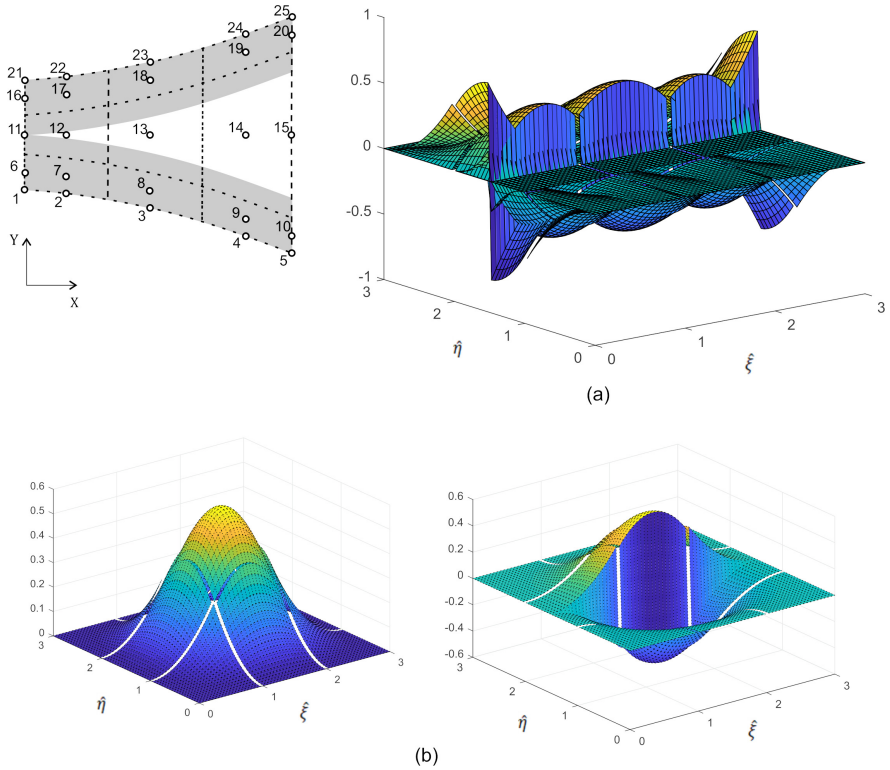

Figure 3.4: Two-dimensional basis functions for control points used in the description of a cracked medium: (a) Effect of the crack on the extended basis functions (b) Comparison between the regular (left) and the extended (right) basis functions for the point in the middle of the domain, control point 13 (see Figure 3.2b for a comparison with one dimensional basis functions). It is noted that Basis functions in (a) are resulted from the tensor product of the basis functions in X and Y-direction in Figure 3.3b

interpolation provides the Kronecker-delta property which is ideal for the shifting technique. With the Kronecker-delta property at hand and employing shifting, the Heaviside function will be confined to the cracked element where the nodal points are also interpolatory. On the other hand, the blending technique brings the effect of the Heaviside function to the adjacent rows of elements. A drawback of this technique is indeed the presence of additional terms in nodal points, which was circumvented by the corrected XFEM [50]. This approach effectively utilises shifting and blending concurrently perpendicular to the crack path, in order to confine the Heaviside effect and to maintain nodal points interpolatory.

Owing to the absence of the Kronecker-delta property in IGA, shifting, which affects the extended part, will also involve adjacent rows of elements similar to blending. The number of control point rows involved perpendicular to the crack path is entirely dependent on the position of the control points and the adopted continuity-order. For example, for quadratic and cubic NURBS one row of control points at each side of the crack will be affected, while

quartic and quintic NURBS will affect even two rows of control points at each side. In sum, the spread of the Heaviside effect to the adjacent elements is inevitable regardless of the technique adopted to enforce compatibility. Nevertheless, shifting and blending are still possible techniques to enforce compatibility. It is noted that the Kronecker-delta property can be brought back when considering Bézier points instead of control points, which will be at the expense of lowering the continuity at element boundaries to $\mathcal{C}^0$. The effect of the shifting technique for these two sets of points is compared in Figure 3.3. By virtue of the tensor product of the univariate bases, bivariate bases can be generated, see Figure 3.4 for the effect of a crack on a bivariate basis function.

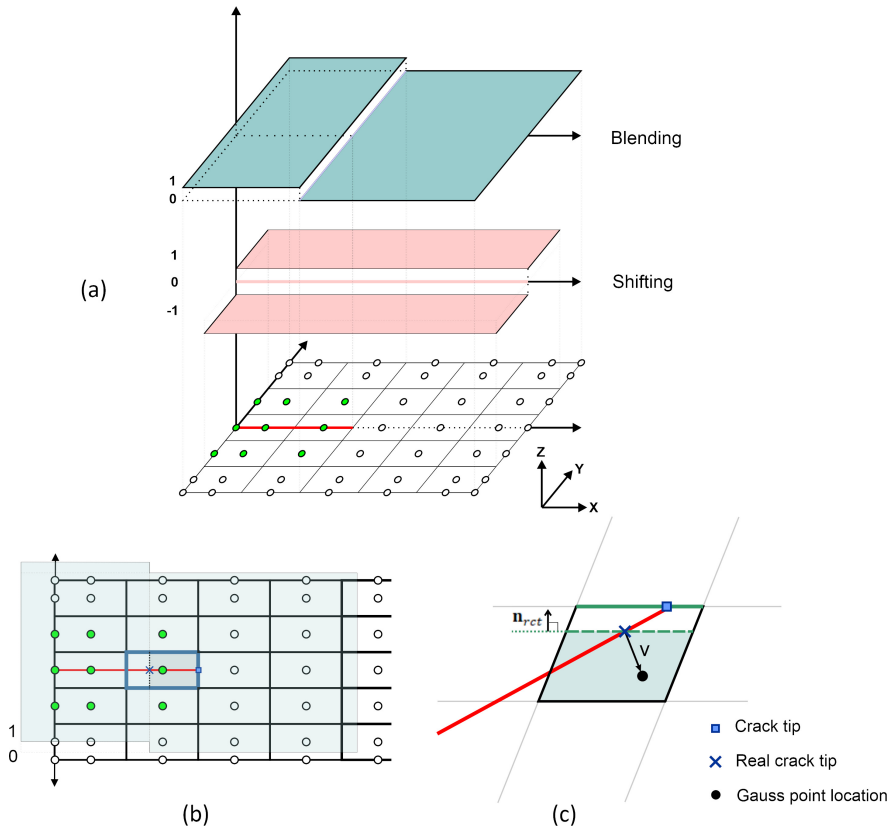

Figure 3.5: Compatibility enforcement for a quadratic order under mode-I fracture: (a) shifting and blending technique for a fully cracked element, (b) blending technique for a partially cracked element while the crack is aligned with the mesh and (c) blending technique for a partially cracked element with an inclined discontinuity. The integration border, dashed green line in (c), is defined as the edge shifted from the green solid line.

The shifting technique adopted here is analogous to the blending technique employed in the extended finite element method in the direction perpendicular to the crack path, see Figures 3.5a, 3.3b and 3.3d, which illustrate how the presence, respectively the absence of

the Kronecker-delta property affect the proposed shifting technique. Due to the fact that the crack is considered as a straight line passing through an entire element, the element size plays a significant role, since some parts of the crack may still violate the crack initiation criterion. Thus, to fulfill the initiation criterion along the crack path, yet to avoid ultra-fine meshes, a blending technique has been adopted to partially apply the cohesive rule inside a cracked element, see Figure 3.5. This blending technique utilises another Heaviside function in the tangential direction, a step function as a new blending, to remove integration points in front of the real crack tip, see Figures 3.5b and 3.5c. Here, the real crack tip is given in Figure 2.5. It is noteworthy that the enrichment is still based on the crack tip at the end of the element, compare Figure 3.5a where the real crack tip coincides with the end of the discontinuity and Figure 3.5b, where the real crack tip is inside the element, but both have the same enrichment. It is noted that by setting a more stringent propagation criterion, when all Gauss points on the new crack path satisfy fracture criterion, the real crack tip coincides with the crack tip at the edge of the element.

Finally, Equation (3.1) is rewritten for shifting and blending technique to enforce compatibility for NURBS.

$$\mathbf{u}(\mathbf{x}) = \sum_{\mathcal{I}\in\mathcal{N}} \mathbf{R}_{\mathcal{I}}(\mathbf{x})\mathbf{a}_{\mathcal{I}} + \sum_{\mathcal{I}^*\in\mathcal{N}^{\mathcal{H}}} \mathcal{H}^{Bl}_{\Gamma_d}(\mathbf{x}) \left(\mathcal{H}^{GP}_{\Gamma_d}(\mathbf{x}) - \mathcal{H}^{\mathcal{I}^*}_{\Gamma_d}\right) \tilde{\mathbf{N}}_{\mathcal{I}^*}(\mathbf{x})\mathbf{b}_{\mathcal{I}^*} \tag{3.19}$$

where $\mathcal{N}^{\mathcal{H}} \subset \mathcal{N}$ denoting the subset enriched by Heaviside, and $\mathcal{H}^{GP}_{\Gamma_d}$ is the Heaviside value of Gauss points, see Equation (2.40). $\mathcal{H}^{\mathcal{I}^*}_{\Gamma_d}$ indicates the Heaviside value for the control point $\mathcal{I}^*$, and $\mathcal{H}^{Bl}_{\Gamma_d}$ is a step function defined on the location of the Gauss point with respect to real crack tip rather than crack tip in Figures 3.5b and 3.5c:

$$\mathcal{H}^{Bl}_{\Gamma_d} = \begin{cases} 0 \quad \text{if} \quad \dfrac{\mathbf{v}\cdot\mathbf{n}_{rct}}{\|\mathbf{v}\|\|\mathbf{n}_{rct}\|} \geq 0 \\ \\ 1 \quad \text{if} \quad \dfrac{\mathbf{v}\cdot\mathbf{n}_{rct}}{\|\mathbf{v}\|\|\mathbf{n}_{rct}\|} < 0 \end{cases} \tag{3.20}$$

3.4 Implementation Aspects: Enhancement and Integration Schemes

The implementation of the formulation in a finite element data structure requires care, since isogeometric analysis involves interelement sharing of control points. Moreover, the possibility to adjust the order of continuity, and consequently the number of control points shared by two adjacent elements complicates a unique solution to the problem. Therefore, we have examined various options to check these issues. We note that elements are here defined as

sections generated by intersecting $\mathcal{C}^0$ lines in the physical space.

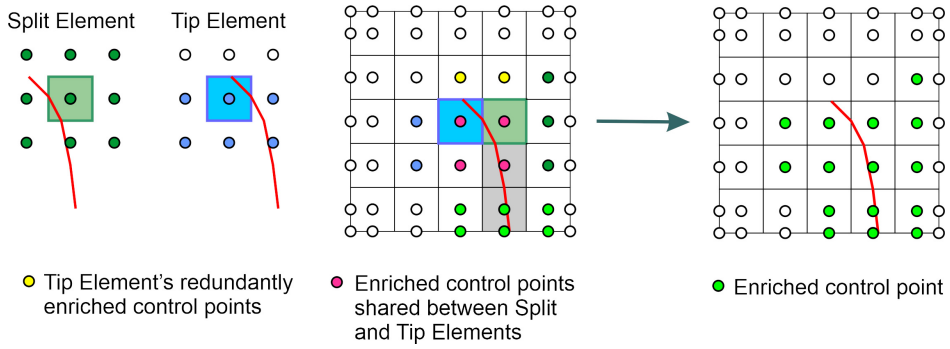

Figure 3.6: Enrichment scheme for a quadratic discretisation. The yellow control points which are shared between split elements (green) and tip element (blue) have been removed from the enrichment.

While the inter-element sharing of control points complicates element-wise enrichment in isogeometric analysis, the Kronecker-delta property of the Bernstein basis functions mitigates the problems encountered in enrichment procedure. Since we deal with cohesive-zone models there is no singularity at the crack tip, and hence no need to apply asymptotic tip enrichment functions. As is also customary in extended finite element analysis using cohesive-zone models, the crack is assumed to cross the element entirely and the crack tip is not considered as opened. The edge where the crack tip lies is denoted as *tip edge*. For $\mathcal{C}^0$ elements with the Kronecker-delta property, the control points corresponding to the tip edge are not enriched. However, for elements with higher-order continuity, the enrichment relies on the continuity order at element boundaries. The control points located at, or in front of the tip edge should be neglected for the enrichment, see Figure 3.6. Our experiments reveal divergence of the solution if only the last column of control points is omitted in the enrichment, which is described in the ensuing sections.

To approximate the discontinuous field in a cracked element, an adequate integration scheme at each side of the discontinuity should be applied. A frequently used scheme is sub-triangulation. This approach is believed to be superior to other methods, e.g. the cell approach, since it is separately defined for each section generated by the crack. Therefore, adopting a required minimum number of Gauss points for each sub-triangle guarantees a sufficient number of Gauss points at each side, even if the discontinuity splits the element into disproportionate segments, e.g. if the crack path is close to the corner of an element. Geometrical mapping for these triangles within an isogeometric analysis framework has been presented by Ghorashi *et al.* [53].

3.5 Assessment of the Formulation

We now assess the correctness and the properties of the formulation and implementation aspects at the hand of various examples.

3.5.1 Continuity order: uniform opening

The first example challenges the capability of the extended isogeometric formulation to handle different NURBS orders for the standard and the extended contributions. This is done using a simple tension test and is compared to a solution obtained using standard interface elements. The geometry and material properties are shown in Figure 3.7. A dummy stiffness has been adopted to constrain the interface before opening.

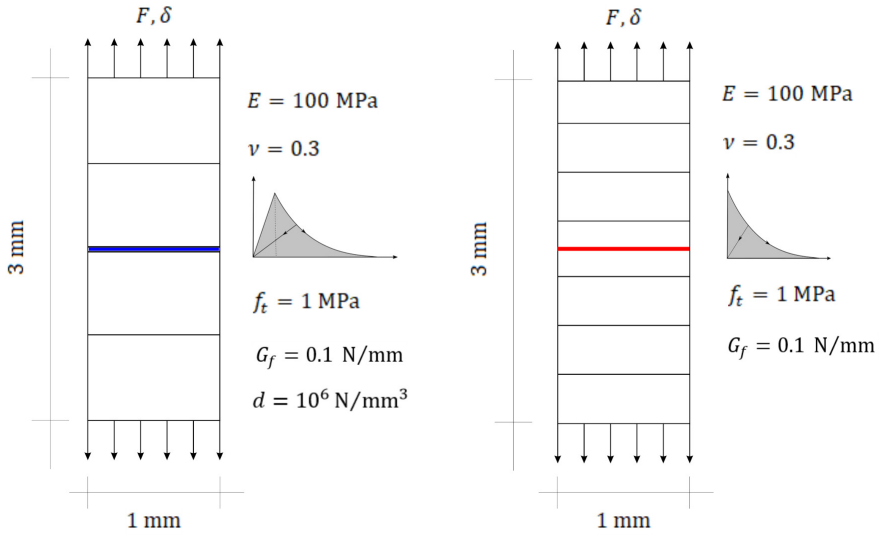

Figure 3.7: Geometry and traction-separation relation employed in the interface element model (left figure) and the XIGA model (right figure). The dummy stiffness d is utilised to keep the interface element closed until the criterion for fracturing is met. F and δ denote force and displacement, respectively. They are utilised with the same definition in the coming examples.

For higher-order XFEM the same order of NURBS can be adopted for the regular and the enhanced parts [77, 83]. For different orders the method only works when a linear interpolation is applied to the extended part [77, 126]. Otherwise, when using blending for the direction perpendicular to the discontinuity, the error in the blending elements will increase and affect the solution accordingly [77]. The Corrected XFEM [50] is a remedy [77], and involves a shifting for the interpolations which possess the Kronecker-delta property.

For eXtended IsoGeometric Analysis, De Luycker *et al.* [39] have arrived at the same conclusions for the case of the same NURBS orders, and have chosen a linear order for the

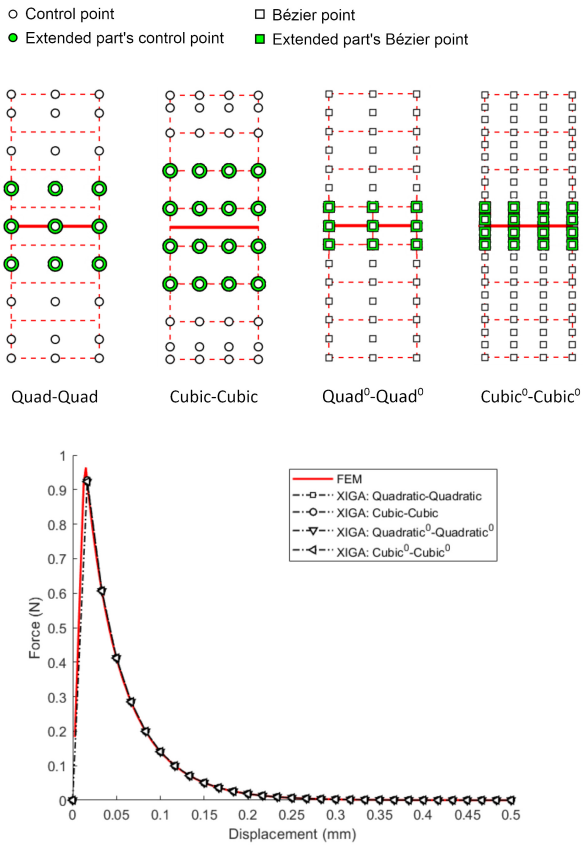

Figure 3.8: Discretisation and load-displacement curve for the uniform opening problem with the same order for standard and extended parts. The first and second NURBS order terms (left to right) in the figure belong to the standard and extended parts, respectively. A superscript zero denotes the Bézier elements. Circles indicate the control points and squares denote the Bézier points. Enriched points are specified with the filled green marker. It is noted that the enriched control points coincide with those belonging to the cracked element. It is noted that FEM solution denotes the interface element model in the remainder of the manuscript, see Figure 3.7left.

extended part in the case of different orders of NURBS. Nevertheless, they have reported convergence issues even with linear order for the extended part, and have suggested $\mathcal{C}^0$ lines as a possible remedy.

Same NURBS order is investigated first for the standard and the extended parts. This is examined for higher-order continuity as well as $\mathcal{C}^0$ continuity at the boundaries of the element. The load-displacement curve in Figure 3.8 agrees with the conclusions reported before [83, 77, 39].

Next, different NURBS orders are examined for the standard and extended parts. Again, the cases of higher-order continuity and $\mathcal{C}^0$ continuous elements are investigated. Figure 3.9

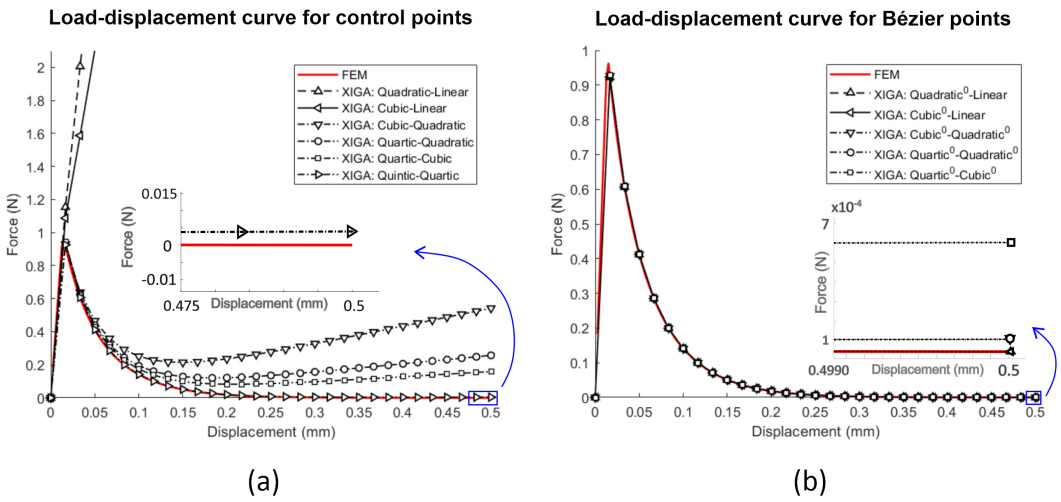

Figure 3.9: Discretisation and load-displacement curve when different NURBS orders are adopted for the standard and extended parts. Higher-order continuity (left) and the Kronecker-delta property (right) are compared through different orders adopted for the standard and extended part. A superscript zero denotes the Bézier elements.

shows that, when higher-order continuity is used for both parts, the error is considerable. When using $\mathcal{C}^0$ continuity, however, the errors are small and the solution is acceptable. Yet, only a linear NURBS for the extended part reproduces the finite element results. Accordingly, the use of linear NURBS for the extended part, which produces perfect results for extended finite element methods [77, 126] is fully correct in extended isogeometric analysis only when $\mathcal{C}^0$-continuity is adopted [39]. This is reminiscent of results for isogeometric interface elements, where traction oscillations could also be prevented by only when inserting $\mathcal{C}^0$ lines [141], as a possible remedy.

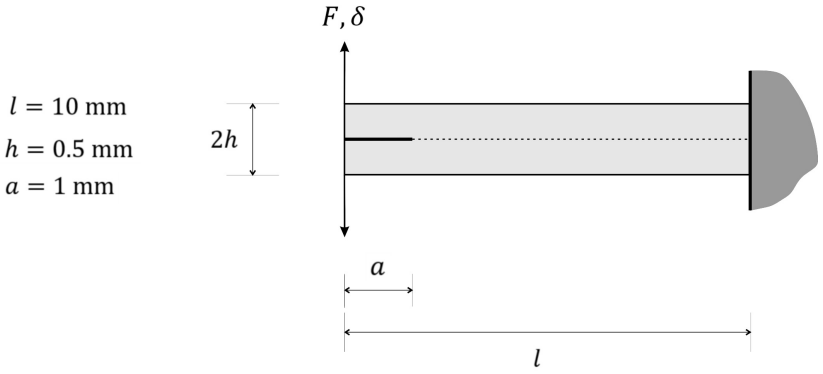

Figure 3.10: Double Cantilever Beam with an initial notch subjected to mode-I loading.

3.5.2 Effect of the order of continuity on the enrichment: peeling test

A Double Cantilever Beam (DCB) peeling test is now investigated to assess the effect of the NURBS order on the enrichment scheme. The geometry is shown in Figure 3.10. The Young's modulus, Poisson's ratio, tensile strength and fracture energy are $E = 100$ MPa, $\nu = 0.3$, $f_t = 1$ MPa and $G_f = 0.1$ Nmm^{-1}, respectively. For the interface elements, which serve as the benchmark, the dummy stiffness, $d = 10^6$ Nmm^{-3}, is used to keep the interface closed until the crack propagation criterion is satisfied.

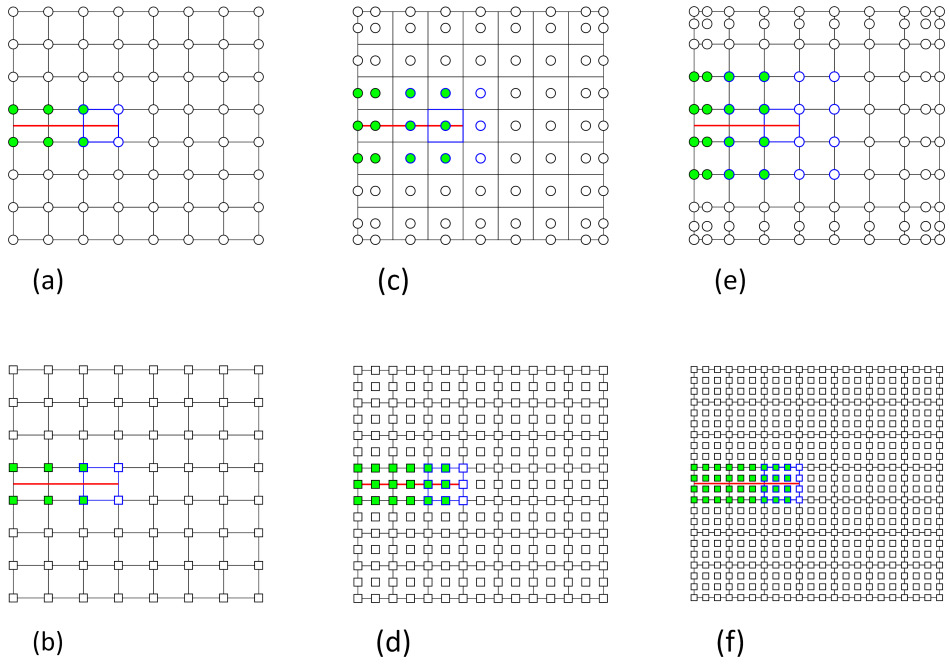

Figure 3.11: Comparison of the enrichment for different NURBS orders: (a) linear control points, (b) linear Bézier points, (c) quadratic control points, (d) quadratic^0 Bézier points, (e) cubic control points, (f) cubic^0 Bézier points. Control/Bézier points belonging to the tip element are differentiated in blue, while the enriched points are filled with green. Note that (a) and (b) are the same and are only presented separately for the sake of compatibility with other cases.

A comparison between the enrichment schemes for different orders of continuity is given in Figure 3.11. For presentation purposes, the enrichment is illustrated for a $7\times$ 7 mesh, instead of the DCB. Following Section 3.4, control points with a location at or in front of the tip edge are removed from the enrichment. When utilising $\mathcal{C}^0$ continuity, however, only one column of control points at the tip edge will be eliminated from enrichment regardless to NURBS order, see Figure 3.11, where the control points and Bézier points are represented by circles and squares, respectively. We observe that, when using control points, only one row at the tip edge is not enriched for linear case. This is the same for quadratic order: remove one column of control points in front of the crack tip. For cubic NURBS, however, two columns

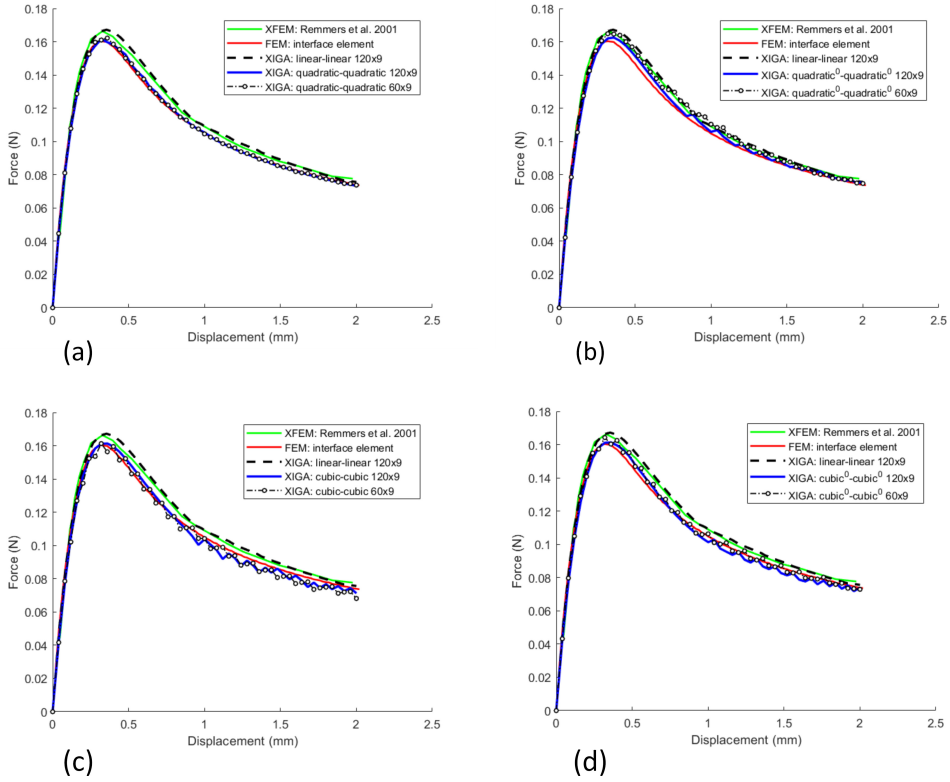

Figure 3.12: Results of the peeling test for a DCB with the same order adopted for both standard and extended part. (a) Results for quadratic order, (b) results for quadratic^0 order, (c) results for cubic order, (d) results for cubic^0 order.

of control points are not enriched. Control/Bézier points belonging to the tip element are differentiated in blue, while the enriched points are filled with green, see Figure 3.11.

The results are given in Figure 3.12. For a quadratic NURBS (Figure 3.11c), $\mathcal{C}^1$-continuity at the element boundaries provides smoother results compared to $\mathcal{C}^0$-continuity (Figure 3.11d). It can be inferred that, when enriching the same number of control/Bézier points, smoother results are obtained in the case of control points. For a cubic NURBS, however, a jagged response results for the 60×9 (the first and the second digits denote the number of element in length and width of the Double Cantilever Beam, respectively) and 120×9 meshes alike. This is because one extra column of control points is removed for the enrichment in the case of a $\mathcal{C}^2$-continuity compared to a $\mathcal{C}^0$-continuity, see Figure 3.11.

To clarify the reason behind the jagged response reported in Figure 3.12c, higher NURBS orders are compared separately in Figure 3.13. For cubic-cubic and quartic-quartic results, it is observed that when the crack propagates to the next element, the last split element releases suddenly along with the last crack tip (which is the new split element adjacent to the new tip element). The release of two elements instead of one (the last crack tip) causes

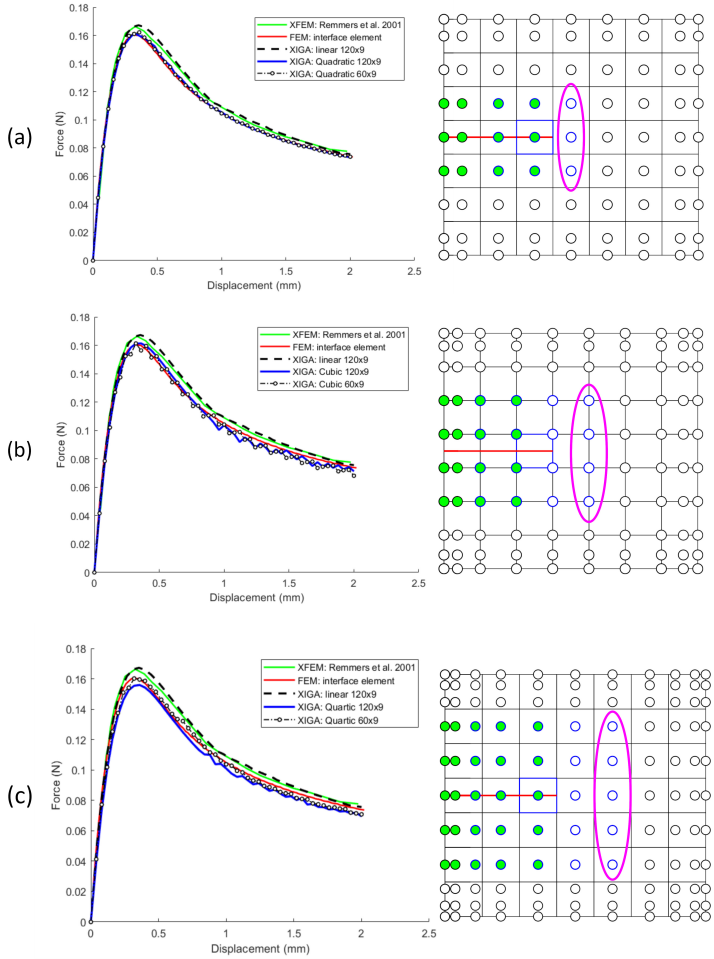

Figure 3.13: Comparison between (a) quadratic-quadratic, (b) cubic-cubic and (c) quartic-quartic orders for a Double Cantilever Beam. The last column of control points are illustrated with the magenta marker.

the jagged response. Therefore, a drop is observed whenever the crack propagates to a new element. This is not the case for quadratic-quadratic since all the control points associated with the split element adjacent to the tip element are enriched. Hence, this phenomenon is related to the number of control point columns. If there is more than one column of control points removed from the enrichment we will have a split element that is not fully enriched. For the same number of control point columns removed, the quartic NURBS has a smoother behaviour than the cubic NURBS, as observed in Figure 3.13. As mentioned before, a divergence of the solution would reveal for cubic-cubic and quartic-quartic orders in Figure 3.13 had only the last column of control points been exempted from enrichment.

Regarding Figures 3.12b and 3.12d, some slight oscillations are observed. This is due to the propagation criterion considered for only the half of the number of Guass points along

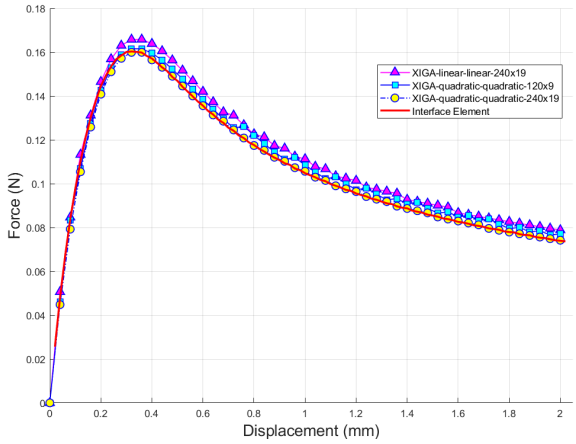

Figure 3.14: Double Cantilever Beam with an ultra-fine mesh and all GPs for crack propagation inside an element.

the crack path, since otherwise the element would have remained intact. This is also the reason why two tips are defined: one ending at the element edge *crack tip*, and another located at the nearest Gauss point to the tip which has met the fracture criterion $\sigma \geq f_t$ as *real crack tip*, see Figure 2.5b. Notice that the *crack tip* is utilised for enrichment of control points, while the *real crack tip* is defined for the blending technique to avoid considering the section of the crack where the fracture criterion has not yet been satisfied (blue Gauss points in Figure 2.5b with $\sigma < f_t$). As mentioned in the preceding, an ultra-fine mesh is required, where all Gauss points along the hypothetical crack path have met the propagation criterion, in order to obtain a smooth force-displacement response. The results of such an approach are shown in Figure 3.14. For the quadratic-quadratic case, the difference between blue and yellow marks shows the sensitivity of the solution to the size of the mesh. Since the quadratic $-$ quadratic and quadratic^0 $-$ quadratic^0 show the least jagged responses, we have used them in the ensuing sections.

3.5.3 Infinite plate with a circular void

While several meshing techniques are available in finite element analysis, the discretisation in IGA is less straightforward, and may involve multi-patches even for fairly simple geometries. Since multi-patches typically require additional care to deal with stress continuity between shared surfaces/edges, it can affect the robustness of the solution. Accordingly, techniques such as the immersed/embedded finite elements or Level Sets may be competitive for modelling, e.g., voids.

Herein, we apply the Level Set technique to a void. The geometry is given in Figure 3.15. Quadratic NURBS has been adopted for both standard and extended parts. For the void level set, the degrees of freedom corresponding to control points which have no influence on the

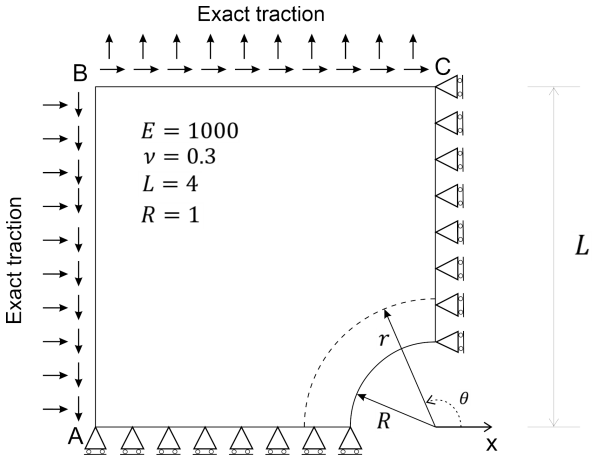

Figure 3.15: Infinite plate with a circular hole subjected to tractions at the boundaries, $\bar{\mathbf{t}}_{\mathrm{AB}} = (-\sigma_{xx}, -\sigma_{xy})$ and $\bar{\mathbf{t}}_{\mathrm{BC}} = (\sigma_{xy}, \sigma_{yy})$.

elements of the solid, should be removed from the system of equations, and those belonging to the elements outside the void should be treated as normal degrees of freedom, see Figure 3.16a. The remaining elements are those crossed by the discontinuity (void's edge), therefore they are partially inside the void. Control points corresponding to this type of elements will be enriched and a weighting function should be defined to partially inactivate the section inside the void. To this end, a step function similar to the blending Heaviside function, Equation (3.20), is defined, where control points inside the void take the value 0, while those outside take the value 1.

If the discontinuity crosses an element such that it is divided disproportionally (e.g. close to a corner), the stiffness matrix can become singular. Defining positive and negative parts as in Figure 2.3 for the elements crossed by the discontinuity, enrichment should only be done if:

$$\frac{A^{\Omega^-}}{A^{\Omega^- \cup \Omega^+}} \quad \text{and} \quad \frac{A^{\Omega^+}}{A^{\Omega^- \cup \Omega^+}} > \mathrm{TOL}_0 \tag{3.21}$$

where $\mathrm{TOL}_0 = 10^{-3}$ has been used, since smaller values resulted in singularity of the tangent stiffness matrix. Accordingly, some elements were exempted from the enrichment, namely the dashed magenta elements in Figure 3.16b, while the elements with blue edges are enriched. Priority in enrichment for the shared control points is given to the blue-edged elements. To further clarify, the enrichment of two adjacent elements with shared control points are illustrated in Figure 3.16b. We observe that the yellow element should not be enriched, but the shared control points between this element and the green element are enriched because of the priority given to the blue-edged element. This will result in the only magenta control point not being enriched for the yellow element, see the specified yellow element at the right hand side of the zoom Figure 3.16b.

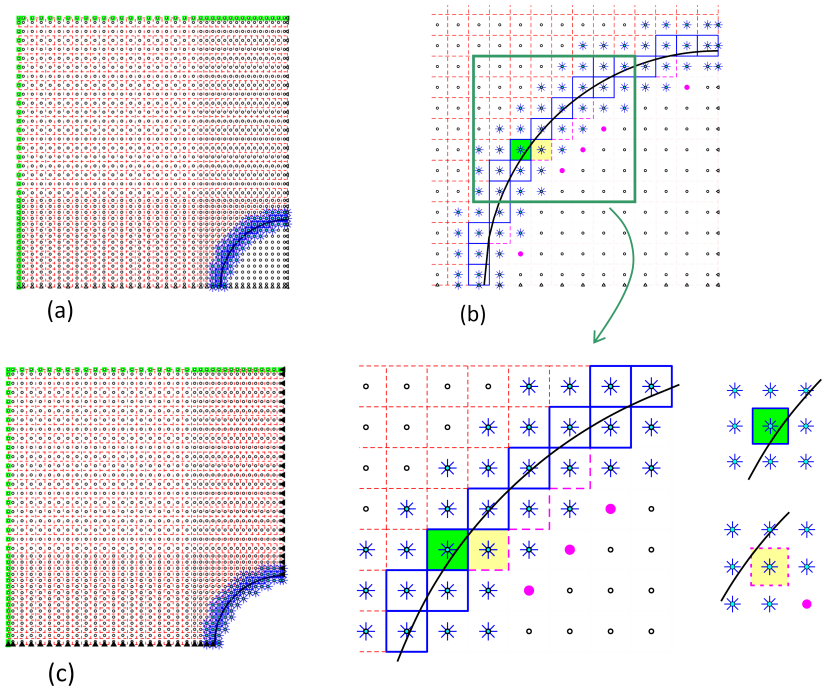

Figure 3.16: Void level set for a perforated plate. (a) Control points of the elements passed by the discontinuity are enriched and those inside the void are not; (b) Removed elements and enrichment owing to a disproportionate split: dashed magenta edges and their corresponding control points (filled with magenta) belong to eliminated elements, while the solid blue edges indicate the enriched elements; (c) Degrees of freedom belonging to control points inside the hole are eliminated from the system of equations. $\mathcal{C}^1$ quadratic NURBS has been adopted for both standard and extended parts.

The results of the void level set approach are compared with those where the void has been modelled explicitly, also using NURBS shape functions and show a good agreement between both approaches in terms of displacements and stresses, Figure 3.17.

3.6 More complicated 2D fracture problems

Below two further cases will be considered, to demonstrate the capability of the formulation to handle crack and void concurrently, and to assess the ability to analyse the propagation of curved cracks. The traction-separation relation of Equation (2.41) has been employed.

3.6.1 Straight crack propagation: wedge splitting test

A wedge with an initial void and a notch is considered. Although the crack path is known, the crack is allowed to propagate freely. The geometry is illustrated in Figure 3.18 with a thickness of 400 mm. A void level set has been used to generate the notch. Also, a $\mathcal{C}^0$ line

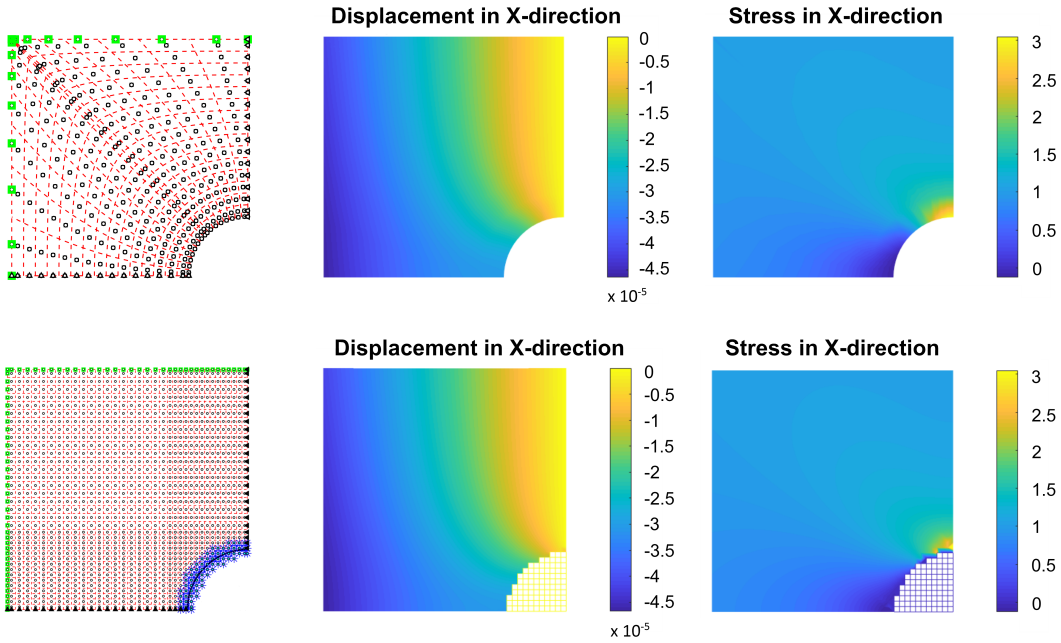

Figure 3.17: Comparison between explicit modelling of the void (first row) and modelling the void using extended isogeometric analysis (second row).

has been added at the location of the force to enforce the Neumann boundary condition. The material properties are as follows: Young's modulus $E = 28,300$ MPa, Poisson's ratio $\nu = 0.18$, tensile $f_t = 2.11$ MPa and fracture energy $G_f = 0.482$ Nmm^{-1}. A quadratic order with $\mathcal{C}^1$-continuity at element boundaries has been adopted.

Figure 3.18 compares the current results with those obtained using an XFEM-like approach [134], although a dummy stiffness was used to keep the crack closed before crack opening, similar to interface elements. Using the same material properties, the present results appear to be closer to the experiment.

3.6.2 Arbitrary crack propagation: L-shaped beam

Finally, free crack propagation is examined for an L-shaped beam, shown in Figure 3.19, with a thickness equal to 100 mm. Material properties are given as: Young's modulus $E = 20$ GPa, Poisson's ratio $\nu = 0.18$, tensile strength $f_t = 2.5$ MPa and fracture energy $G_f = 0.13$ Nmm^{-1}. A void level set has been used to generate the geometry, see Figure 3.19. A $\mathcal{C}^0$ line (in magenta) has been added at the location of the force to easily enforce the Neumann boundary condition. The other $\mathcal{C}^0$ lines (in black) have been added to align the mesh with the void in order to avoid crack-void interaction.

Based on the results of Figure 3.12 a quadratic^0 – quadratic^0 NURBS has been chosen. The difficulty of the example lies in the role of the stress distribution, where small variations can lead to significant changes in the direction of crack propagation. Although isogeometric

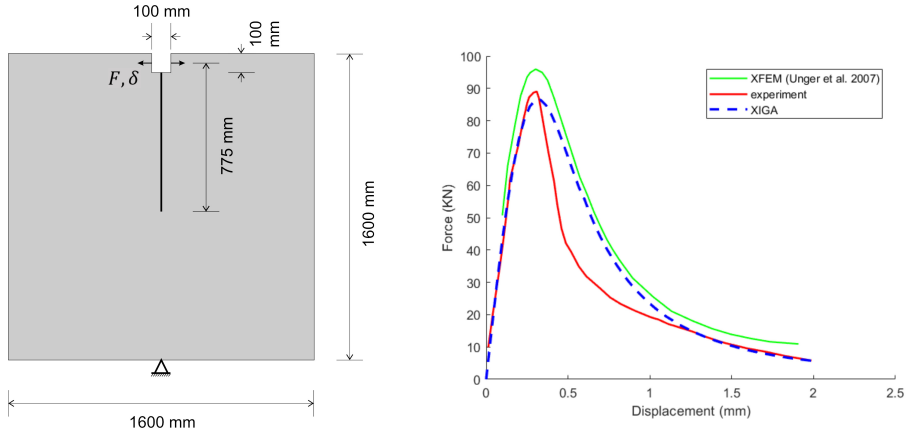

Figure 3.18: Wedge splitting test: geometry and results.

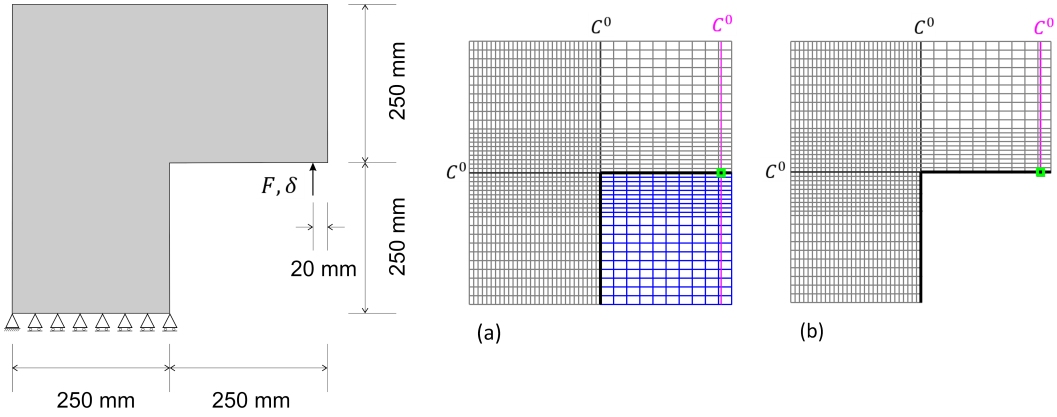

Figure 3.19: Geometry and descretisation of the L-shaped beam: (a) exploiting void level set to form the geometry, (b) final geometry after element removal. The magenta C^0 line is added to pinpoint the load location. Black lines have been added to align the mesh with the void.

analysis exploiting B-splines vastly improves the stress prediction, using a nonlocal averaging method as detailed before can often be beneficial to improve the crack path. Indeed, the crack extension is highly sensitive to the computed stress distribution around the crack tip [42, 134]. In turn, the stress distribution depends on numerical issues like the length scale over which averaging is done, the number of Gauss points and the adopted continuity order. Therefore, even nonlocal averaging of stresses may not lead to sufficiently accurate measures to properly predict the crack path [134]. This can result in drastic changes in the crack path which have been already reported for XFEM [42, 134], and can include a doubling back of the crack on its original path

The results are shown in Figure 3.20. A behaviour similar to XFEM [42] and Powell-Sabin B-splines [27] is observed. An abrupt change occurs in the propagation direction, as shown in Figure 3.20a, which is not the case for T-splines [29]. Apart from the sensitivity of the

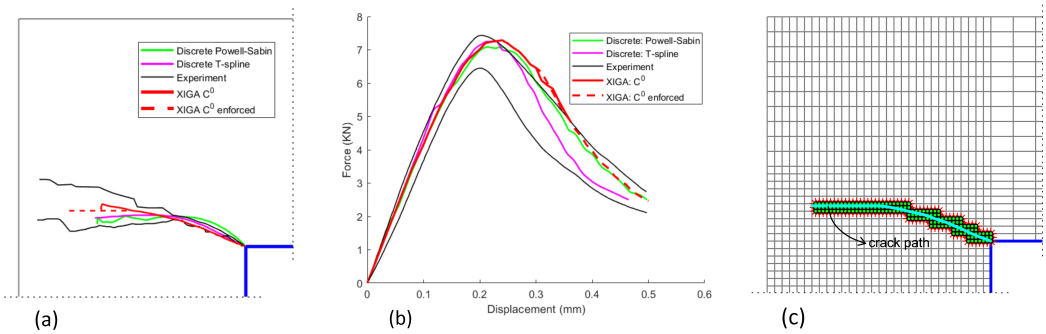

Figure 3.20: Results for L-shaped beam: (a) crack propagation profile, (b) mechanical behaviour and (c) enrichment for the XIGA $\mathcal{C}^0$ enforced case. XIGA $\mathcal{C}^0$ here denotes quadratic^0 – quadratic^0 order.

nonlocal approach to find the proper crack extension direction, the order of NURBS adopted for the crack path therefore also appears to play a role. T-splines exploit their higher-order continuity property [29], resulting in a smooth crack path, as illustrated in Figure 3.21.

To validate the XIGA approach for curved crack propagation, and to examine the behaviour of the smooth crack path, the crack path is therefore enforced to become straight before an erratic change in the path, that is, the red dashed line deviating from the solid red line in Figure 3.20a and the cyan solid line in Figure 3.20c. Then, results are obtained which are close to those obtained using Powell-Sabin B-splines, see the red dashed line in Figure 3.20b, while the red solid line has been terminated around 5 KN.

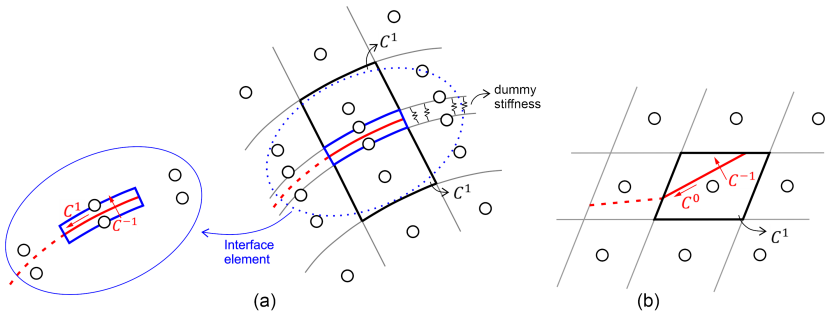

Figure 3.21: Effect of the order of continuity at element boundaries on the crack propagation direction: (a) $\mathcal{C}^1$ continuity along the crack path for a discrete method with a smoother change than (b) $\mathcal{C}^0$ continuity along the crack path of XIGA. A quadratic NURBS is used for both methods for the sake of comparison.

3.7 Concluding remarks

An extended isogeometric analysis (XIGA) procedure has been developed for cohesive fracture by adding an additional blending technique which is also capable of locating a more realistic

crack tip position inside an element. Moreover, in the direction perpendicular to the crack path, shifting has been utilised to ensure compatibility with the remainder of the mesh. To ensure compatibility with standard finite element data structures Bézier extract has been used and in this way the method comes close to an extended finite element method. Compared to the latter, complications ensue, however, since the higher-order continuity of B-splines and NURBS used in extended isogeometric analysis affect more rows of elements parallel to the crack when using a shifting technique to ensure compatibility of the cracked elements with the neighbouring elements, and since the Kronecker-delta property does not hold anymore. The latter observation is the reason why blending has been introduced ahead of the crack tip.

The accuracy with respect to different orders of continuity for the regular and extended parts of the displacement field has been investigated at the hand of a simple tension test. It has been shown that, when using the same order for both parts, the extended isogeometric analysis approach works perfectly irrespective of the order of continuity at the boundaries of the elements. For a different order of continuity, however, Bézier points ($\mathcal{C}^0$-continuity at element boundaries) should be used for both parts. The differences encountered when either enriching control or Bézier points have been assessed for a peel test. The method has also been shown to give good results for a plate with a hole, for crack-void interaction and for arbitrary crack propagation in an L-shaped beam.

Chapter 4

Geometrically Nonlinear XIGA

In this chapter[1], a geometrically nonlinear extended isogeometric analysis approach is proposed for cohesive fracture. A shifting technique is used to enforce compatibility in the direction perpendicular to the crack path, while a blending technique has been adopted to remove the effect of the discontinuity in the extension of the cohesive crack. Bézier extraction is employed to cast the formulation in a finite element datastructure. The use of a sign function instead of a Heaviside step function removes the need to make an assumption for the normal to the crack at its centreline. Examples are given to illustrate the methodology, including buckling of a delaminated structure and an assessment of the interface contribution to the tangent stiffness matrix.

4.1 Research Background

Simulation has become an integral part of engineering and applications nowadays extend far beyond the original area of structural engineering. They encompass, to name a few, fluid flow in progressively fracturing porous medium [70], damage in ductile fracture [25], biological composites [43], or delamination in layered composites. Various approaches have been pursued to solve the latter problem, with interface elements [4, 114, 115, 3, 1] being the classical (and still very effective) method. Exploiting the partition-of-unity property of finite element shape functions [9] allows for modelling propagating of discontinuities, independent of the original, underlying discretisation [91, 15]. It is commonly known as the eXtended Finite Element Method (XFEM) and has also been applied to delamination in composites

[1]This chapter is directly adopted from:

Fathi, F. and de Borst, R., 2021. Geometrically nonlinear extended isogeometric analysis for cohesive fracture with applications to delamination in composites. Finite Elements in Analysis and Design, 191, p.103527.

[143].

XFEM utilises standard Lagrangian shape functions, and so does the application to delamination [143], which results in $\mathcal{C}^0$-continuity across element boundaries. More recently, Non-Uniform Rational B-Splines (NURBS) have been proposed as a replacement of Lagrangian functions in finite element analysis [30]. The resulting modelling approach, coined IsoGeometric Analysis (IGA) possesses some significant advantages. It enables an exact parametrisation of the geometry, as well as a higher-order inter-element continuity, which is especially beneficial for numerically solving higher-order differential equations, e.g. the Cahn-Hilliard equation [54, 76].

Blending IGA and the XFEM, eXtended IsoGeometric Analysis (XIGA) has been proposed in [39]. It has been widely developed for Linear Elastic Fracture Mechanics (LEFM), e.g. thin shell analysis of Kirchhoff-Love theory [95]. In a further development, this approach has been extended from LEFM to cohesive fracture [44].

Herein, XIGA is extended to geometric nonlinearity and is applied to a number of typical delamination problems. As in [44] a shifting technique will be utilised to enforce compatibility in the direction perpendicular to the crack path. The inter-element share of control points governing Non-Uniform Rational B-Splines (NURBS) complicates this technique. Indeed, the lack of the Kronecker-delta property in isogeometric analysis extends the discontinuous domain to multiple rows of elements perpendicular to the crack path. This is different from the single row of elements in XFEM [44]. To remove the effect of the discontinuity in the extension of the cohesive crack a blending technique has been adopted, as also proposed in [44]. Finally, Bézier extraction has been exploited to cast XIGA in an element-wise format compatible with finite element data structure. While the XFEM formulation to simulate delamination has employed a step function [143], necessitating an additional assumption for the vector normal to the crack, making an assumption is avoided here by instead using a sign function to define the normal vectors for the sides and for the centreline of the crack.

This chapter continues with a summary of the kinematics of a displacement discontinuity, followed by the equilibrium equations which govern the bulk and the discontinuity, respectively. The weak forms are discussed as well as the discretisation for XIGA using Bézier extraction-based NURBS. Aspects of compatibility and implementation are reviewed next. The paper concludes with case studies which demonstrate the capability to simulate delamination and its propagation, followed by an analysis of buckling instability in delaminated composites and an assessment of the contribution of the interface to the tangential stiffness matrix.

4.2 Kinematic and Constitutive Equations

The equation of motion $\Phi(\mathbf{X}, t)$ maps a point $\mathbf{X}$ in the reference configuration onto the corresponding point $\mathbf{x}$ in the spatial configuration ($t > 0$), see Figure 4.1. To model a displacement discontinuity we use an extended approach, where the standard displacement field is augmented by an enhanced field. In the following the equilibrium, kinematic and constitutive equations in the bulk and at the discontinuity are detailed.

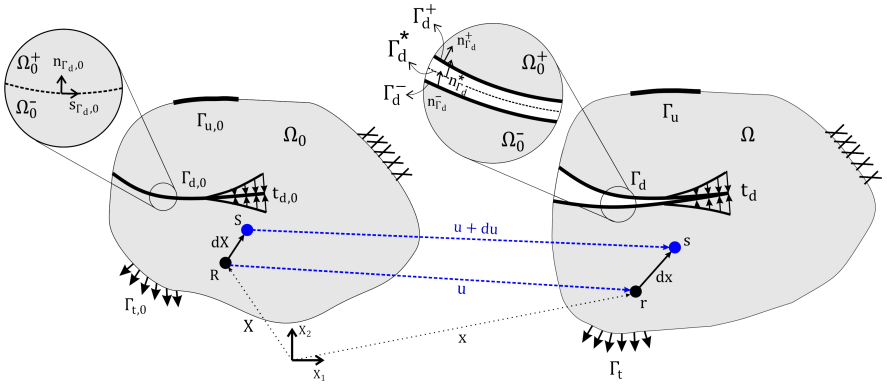

Figure 4.1: Boundary value problem with cohesive tractions. The reference configuration (left) is mapped onto the spatial configuration (right) through the motion $\Phi(\mathbf{X}, t)$. The mapping of a vector from the material to current configuration is also illustrated. u and u+du are functions of the regular displacement û and the displacement jump ũ.

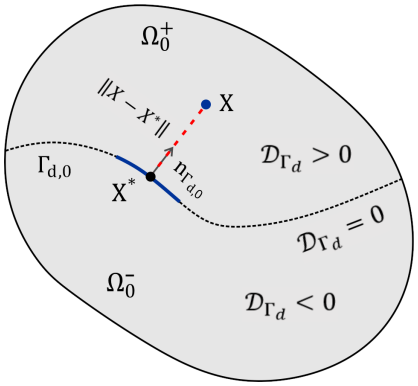

Figure 4.2: Signed distance function in the material description. The point $\mathbf{X}^*$ is the closest projection of the point $\mathbf{X}$ onto the discontinuity $\Gamma_{d,0}$

.

4.2.1 Kinematics of displacement discontinuity

Exploiting the partition of unity property of the interpolants for the displacement field, the displacement field can be separated into a standard part and a so-called extended contribu-

tion:

$$\Phi(\mathbf{X},t) := \mathbf{x}(\mathbf{X},t) = \mathbf{X} + \hat{\mathbf{u}}(\mathbf{X},t) + \mathcal{H}_{\Gamma_{\mathrm{d},0}}(\mathbf{X})\tilde{\mathbf{u}}(\mathbf{X},t) \tag{4.1}$$

where $\hat{\mathbf{u}}(\mathbf{X},t) = \mathbf{N}(\mathbf{X})\mathbf{a}(\mathbf{X},t)$ and $\tilde{\mathbf{u}}(\mathbf{X},t) = \mathbf{N}(\mathbf{X})\mathbf{b}(\mathbf{X},t)$, with $\mathbf{N}$ denoting the set of finite element shape functions. $\mathbf{a}$ and $\mathbf{b}$ contain the regular and the enhanced degrees of freedom, respectively. The Heaviside function in the reference configuration, $\mathcal{H}_{\Gamma_{d,0}}$, is defined using the signed distance function $\mathcal{D}_{\Gamma_{d,0}}$ [44], see also Figure 4.2:

$$\mathcal{H}_{\Gamma_{d,0}}(\mathbf{X}) := \mathbf{n}_{\Gamma_{d,0}} \cdot \nabla\mathcal{D}_{\Gamma_{d,0}}(\mathbf{X}) = \begin{cases} -1 & \text{if} \quad \mathcal{D}_{\Gamma_{d,0}}(\mathbf{X}) < 0 \\ 0 & \text{if} \quad \mathcal{D}_{\Gamma_{d,0}}(\mathbf{X}) = 0 \\ +1 & \text{if} \quad \mathcal{D}_{\Gamma_{d,0}}(\mathbf{X}) > 0 \end{cases} \tag{4.2}$$

where $\mathbf{n}_{\Gamma_{d,0}}$ is the vector normal to the discontinuity in the reference configuration. It is noted that the step function used in Wells *et al.* [143] has been replaced and the implications will be discussed in what follows. Taking the gradient of Equation (4.1) the deformation gradient results:

$$\mathbf{F} := \nabla_{\mathbf{X}}\Phi = \hat{\mathbf{F}} + \mathcal{H}_{\Gamma_{\mathrm{d},0}}(\mathbf{X})\tilde{\mathbf{F}} + 2\delta_{\Gamma_{\mathrm{d},0}}(\tilde{\mathbf{u}} \otimes \mathbf{n}_{\Gamma_{\mathrm{d},0}}) \tag{4.3}$$

with $\hat{\mathbf{F}} = \mathbf{1} + \nabla_{\mathbf{X}}\hat{\mathbf{u}}$ and $\tilde{\mathbf{F}} = \nabla_{\mathbf{X}}\tilde{\mathbf{u}}$, while $\mathbf{1}$ denotes the identity matrix.

As can be observed from Figure 4.1 the vector normal to the crack centreline and those to the sides will differ from each other when accounting for geometrically nonlinear effects. When using a step function the vectors normal to the sides of the crack are defined by Nanson's relation [143], and the mean can be used to define the crack centreline [143]. This is different when exploiting a sign function. Now, the normal to the crack centreline is defined unambiguously:

$$\mathbf{n}^{-}_{\Gamma_{\mathrm{d}}} = \det(\hat{\mathbf{F}} - \tilde{\mathbf{F}}) \left((\hat{\mathbf{F}} - \tilde{\mathbf{F}})^{\mathrm{T}}\right)^{-1} \mathbf{n}_{\Gamma_{d,0}} \frac{\mathrm{d}\Gamma_{\mathrm{d},0}}{\mathrm{d}\Gamma^{-}_{\mathrm{d}}}, \tag{4.4a}$$

$$\mathbf{n}^{*}_{\Gamma_{\mathrm{d}}} = \det(\hat{\mathbf{F}})(\hat{\mathbf{F}})^{-\mathrm{T}}\mathbf{n}_{\Gamma_{d,0}} \frac{\mathrm{d}\Gamma_{\mathrm{d},0}}{\mathrm{d}\Gamma^{*}_{\mathrm{d}}}, \tag{4.4b}$$

$$\mathbf{n}^{+}_{\Gamma_{\mathrm{d}}} = \det(\hat{\mathbf{F}} + \tilde{\mathbf{F}}) \left((\hat{\mathbf{F}} + \tilde{\mathbf{F}})^{\mathrm{T}}\right)^{-1} \mathbf{n}_{\Gamma_{d,0}} \frac{\mathrm{d}\Gamma_{\mathrm{d},0}}{\mathrm{d}\Gamma^{+}_{\mathrm{d}}} \tag{4.4c}$$

with $*$ denoting the crack centreline, see Figure 4.1.

4.2.2 Governing equations of the bulk

As is customary in finite deformations hyperelasticity is used, which is fully defined by a strain energy functional [20]:

$$\Psi(\mathbf{F}(\mathbf{X}),\mathbf{X}) = \int_{t_0}^{t} \mathbb{P}(\mathbf{F}(\mathbf{X}),\mathbf{X}) : \dot{\mathbf{F}}\mathrm{d}t, \quad \dot{\Psi} = \mathbb{P} : \dot{\mathbf{F}} \tag{4.5}$$

where $\mathbb{P}$ denotes the first Piola-Kirchhoff stress tensor which is conjugate to the deformation gradient $\mathbf{F}$. A Neo-Hookean material model has been adopted with $\Psi = \frac{\mu}{2}(I_1 - 3) - \mu \ln J + \frac{\lambda}{2}(\ln J)^2$, μ and λ being Lamé's coefficients, $J = \det\mathbf{F}$, and $I_1 = \text{trace}(\mathbf{C})$ denotes an invariant with $\mathbf{C} = \mathbf{F}^{\mathrm{T}}\mathbf{F}$ the right Cauchy tensor [20].

In the absence of the acceleration and body forces, the strong form of the equilibrium equation in the reference configuration reads:

$$\begin{cases} \nabla_{\mathbf{X}} \cdot \mathbb{P} = & 0 & \mathbf{X} \in \Omega_0 \\ \mathbf{u} = & \overline{\mathbf{u}}_0 & \mathbf{X} \in \Gamma_{\mathrm{u},0} \\ \mathbf{n}_0 \cdot \mathbb{P} = & \overline{\mathbf{t}}_0 & \mathbf{X} \in \Gamma_{\mathrm{t},0} \\ \mathbf{n}_{\Gamma_{\mathrm{d},0}} \cdot \mathbb{P} = & \mathbf{t}_{\mathrm{d},0} & \mathbf{X} \in \Gamma_{\mathrm{d},0} \end{cases}, \tag{4.6}$$

$\overline{\mathbf{u}}_0$ and $\overline{\mathbf{t}}_0$ indicate the prescribed displacements and tractions, respectively.

4.2.3 Cohesive-zone model

Similar to Section 2.2.3, mode-I will be the governing fracture mode considered in the ensuing examples. It is assumed that the tractions normal to a discontinuity can be captured using an exponential decay function of the crack opening. A Kuhn-Tucker condition governs the irreversibility of the fracture opening.

4.3 Variational Formulation

Adopting the principle of virtual work, the weak form of Equation (4.6) in the reference configuration reads:

$$\int_{\Omega_0} \nabla_{\mathbf{X}}\boldsymbol{\zeta} : \mathbb{P}\, \mathrm{d}\Omega - \int_{\Gamma_{\mathrm{t},0}} \boldsymbol{\zeta} \cdot \bar{\mathbf{t}}\, \mathrm{d}\Gamma = 0, \tag{4.7}$$

which must hold for all admissible variations $\boldsymbol{\zeta}$, which is comprised of two components, $\hat{\boldsymbol{\zeta}}$ and $\tilde{\boldsymbol{\zeta}}$, respectively. The test function and its gradient read:

$$\boldsymbol{\zeta} = \hat{\boldsymbol{\zeta}} + \mathcal{H}_{\Gamma_{\mathrm{d},0}}\tilde{\boldsymbol{\zeta}}, \tag{4.8a}$$

$$\nabla_{\mathbf{X}}\boldsymbol{\zeta} = \nabla_{\mathbf{X}}\hat{\boldsymbol{\zeta}} + \mathcal{H}_{\Gamma_{\mathrm{d},0}}(\nabla_{\mathbf{X}}\tilde{\boldsymbol{\zeta}}) + 2\delta_{\Gamma_{\mathrm{d},0}}(\tilde{\boldsymbol{\zeta}} \otimes \mathbf{n}_{\Gamma_{\mathrm{d},0}}). \tag{4.8b}$$

Inserting Equations (4.8a) and (4.8b) into Equation (4.7) and utilising the identity $\int_\Omega \delta_{\Gamma_\mathrm{d}}(\mathbf{x})\phi(\mathbf{x})d\Omega = \int_\Gamma \phi(\mathbf{x})d\Gamma$ leads to separate weak forms:

$$\int_{\Omega_0} \nabla_{\mathbf{X}}\hat{\boldsymbol{\zeta}} : \mathbb{P}\, \mathrm{d}\Omega_0 = \int_{\Gamma_{\mathrm{t},0}} \hat{\boldsymbol{\zeta}} \cdot \bar{\mathbf{t}}_0\, \mathrm{d}\Gamma_0 \tag{4.9a}$$

$$\int_{\Omega_0} \mathcal{H}_{\Gamma_{\mathrm{d},0}}(\nabla_{\mathbf{X}}\tilde{\boldsymbol{\zeta}}) : \mathbb{P}\,\mathrm{d}\Omega_0 + 2\int_{\Gamma_{\mathrm{d},0}} \tilde{\boldsymbol{\zeta}} \cdot \mathbf{t}_{\mathrm{d},0}\,\mathrm{d}\Gamma_0 = \int_{\Gamma_{\mathrm{t}}} \mathcal{H}_{\Gamma_{\mathrm{d},0}}\tilde{\boldsymbol{\zeta}} \cdot \bar{\mathbf{t}}_0\,\mathrm{d}\Gamma_0. \tag{4.9b}$$

It is noted that the First Piola-Kirchhoff stress tensor $\mathbb{P}$ is non-symmetric. To obtain a symmetric stress matrix defined entirely in the material configuration, the Second Piola-Kirchhoff stress tensor is defined by pulling back the spatial force of the First Piola-Kirchhoff stress tensor [20]: $\boldsymbol{\Sigma} = \mathbf{F}^{-1}\mathbb{P}$. Substituting this relation in the weak forms in Equation (4.9) yields:

$$\int_{\Omega_0} \nabla_{\mathbf{X}}\hat{\boldsymbol{\zeta}} : (\mathbf{F}\boldsymbol{\Sigma})\,\mathrm{d}\Omega_0 = \int_{\Gamma_{\mathrm{t},0}} \hat{\boldsymbol{\zeta}} \cdot \bar{\mathbf{t}}_0\,\mathrm{d}\Gamma_0, \tag{4.10a}$$

$$\int_{\Omega_0} \mathcal{H}_{\Gamma_{\mathrm{d},0}}(\nabla_{\mathbf{X}}\tilde{\boldsymbol{\zeta}}) : (\mathbf{F}\boldsymbol{\Sigma})\,\mathrm{d}\Omega_0 + 2\int_{\Gamma_{\mathrm{d},0}} \tilde{\boldsymbol{\zeta}} \cdot (\mathbf{F}\boldsymbol{\Sigma}\mathbf{n}_{\Gamma_{\mathrm{d},0}})\,\mathrm{d}\Gamma_0 = \int_{\Gamma_{\mathrm{t},0}} \mathcal{H}_{\Gamma_{\mathrm{d},0}}\tilde{\boldsymbol{\zeta}} \cdot \bar{\mathbf{t}}_0\,\mathrm{d}\Gamma_0. \tag{4.10b}$$

4.4 Linearised Discrete Equations

To derive the governing equations in matrix-vector notation, the weak forms are first linearised.

4.4.1 Linearisation of the equilibrium equations

In the reference configuration the rate of the internal virtual work in the left hand side of Equation (4.10) reads,

$$\delta\dot{W}^{\mathbf{a}}_{\mathrm{int}} = \int_{\Omega_0} \nabla_{\mathbf{X}}\hat{\boldsymbol{\zeta}} : (\dot{\mathbf{F}}\boldsymbol{\Sigma})\mathrm{d}\Omega_0 + \int_{\Omega_0} \nabla_{\mathbf{X}}\hat{\boldsymbol{\zeta}} : (\mathbf{F}\dot{\boldsymbol{\Sigma}})\mathrm{d}\Omega_0 \tag{4.11}$$

$$\begin{aligned}\delta\dot{W}^{\mathbf{b}}_{\mathrm{int}} = &\int_{\Omega_0} \mathcal{H}_{\Gamma_{\mathrm{d},0}}(\nabla_{\mathbf{X}}\tilde{\boldsymbol{\zeta}}) : (\dot{\mathbf{F}}\boldsymbol{\Sigma})\mathrm{d}\Omega_0 + \int_{\Omega_0} \mathcal{H}_{\Gamma_{\mathrm{d},0}}(\nabla_{\mathbf{X}}\tilde{\boldsymbol{\zeta}}) : (\mathbf{F}\dot{\boldsymbol{\Sigma}})\mathrm{d}\Omega_0 \\ &+ 2\int_{\Gamma_{\mathrm{d},0}} \tilde{\boldsymbol{\zeta}} \cdot (\dot{\mathbf{F}}\boldsymbol{\Sigma}\mathbf{n}_{\Gamma_{\mathrm{d},0}})\mathrm{d}\Gamma_0 + 2\int_{\Gamma_{\mathrm{d},0}} \tilde{\boldsymbol{\zeta}} \cdot (\mathbf{F}\dot{\boldsymbol{\Sigma}}\mathbf{n}_{\Gamma_{\mathrm{d},0}})\mathrm{d}\Gamma_0\end{aligned} \tag{4.12}$$

The rate of the deformation gradient, $\dot{\mathbf{F}}$, is given by:

$$\dot{\mathbf{F}} = \frac{\partial \mathbf{v}}{\partial \mathbf{X}} = \frac{\partial \mathbf{v}}{\partial \mathbf{x}}\frac{\partial \mathbf{x}}{\partial \mathbf{X}} = \mathbf{l}\mathbf{F} \tag{4.13}$$

where $\mathbf{v}$ and $\mathbf{l}$ are the velocity and the velocity gradient, respectively.

4.4.2 Discretised equations

Next, the linearised formulation is cast in the discrete matrix notation format. To this end NURBS are recalled from Section 2.1.4, where Bézier extraction was utilised to cast NURBS in terms of Bernstein polynomials. Using a Total Lagrangian approach the position field of

Equation (4.1) is rewritten as:

$$\mathbf{x} = \mathbf{X} + \mathbf{R}\mathbf{a} + \mathcal{H}_{\Gamma_{d,0}}\mathbf{R}\mathbf{b}, \tag{4.14}$$

where $\mathbf{R}$ contains the NURBS basis functions. The discretised format of the equilibrium equations can then be written as:

$$\begin{bmatrix} \mathbf{f}_{\mathrm{a}}^{\mathrm{int}} \\ \mathbf{f}_{\mathrm{b}}^{\mathrm{int}} \end{bmatrix} = \begin{bmatrix} \mathbf{f}_{\mathrm{a}}^{\mathrm{ext}} \\ \mathbf{f}_{\mathrm{b}}^{\mathrm{ext}} \end{bmatrix}, \tag{4.15}$$

where, in the reference configuration,

$$\mathbf{f}_{\mathrm{a}}^{\mathrm{ext}} = \int_{\Gamma_{\mathrm{t},0}} \mathbf{R}^{\mathrm{T}}\bar{\mathbf{t}}_0 \,\mathrm{d}\Gamma_0 \tag{4.16a}$$

$$\mathbf{f}_{\mathrm{b}}^{\mathrm{ext}} = \int_{\Gamma_{\mathrm{t},0}} \mathcal{H}_{\Gamma_{d,0}}\mathbf{R}^{\mathrm{T}}\bar{\mathbf{t}}_0 \,\mathrm{d}\Gamma_0 \tag{4.16b}$$

$$\mathbf{f}_{\mathrm{a}}^{\mathrm{int}} = \int_{\Omega_0} \mathbf{B}_{\mathrm{N}}^{\mathrm{T}}\boldsymbol{\Sigma} \,\mathrm{d}\Omega \tag{4.16c}$$

$$\mathbf{f}_{\mathrm{b}}^{\mathrm{int}} = \int_{\Omega_0} \mathcal{H}_{\Gamma_{\mathrm{d},0}}\mathbf{B}_{\mathrm{N}}^{\mathrm{T}}\boldsymbol{\Sigma} \,\mathrm{d}\Omega_0 + 2\int_{\Gamma_{\mathrm{d},0}} \mathbf{R}^{\mathrm{T}}\mathbf{t}_{d,0} \,\mathrm{d}\Gamma_0 \tag{4.16d}$$

and

$$\mathbf{B}_{\mathrm{N}} = \mathbf{L}_0\mathbf{N}, \tag{4.17a}$$

$$\mathbf{B}_{\mathrm{G}} = \bar{\mathbf{L}}_0\mathbf{N}. \tag{4.17b}$$

In Equations (4.17) the following matrices have been used:

$$\mathbf{L}_0^{\mathbf{T}} = \mathbf{F}\begin{bmatrix} \frac{\partial}{\partial \mathbf{X}_1} & 0 & \frac{\partial}{\partial \mathbf{X}_2} \\ 0 & \frac{\partial}{\partial \mathbf{X}_2} & \frac{\partial}{\partial \mathbf{X}_1} \end{bmatrix} = \begin{bmatrix} F_{11}\frac{\partial}{\partial \mathbf{x}_1} & F_{12}\frac{\partial}{\partial \mathbf{x}_2} & F_{11}\frac{\partial}{\partial \mathbf{x}_2} + F_{12}\frac{\partial}{\partial \mathbf{x}_1} \\ F_{21}\frac{\partial}{\partial \mathbf{x}_1} & F_{22}\frac{\partial}{\partial \mathbf{x}_2} & F_{21}\frac{\partial}{\partial \mathbf{x}_2} + F_{22}\frac{\partial}{\partial \mathbf{x}_1} \end{bmatrix}, \tag{4.18a}$$

and

$$\bar{\mathbf{L}}_0^{\mathbf{T}} = \begin{bmatrix} \frac{\partial}{\partial \mathbf{X}_1} & \frac{\partial}{\partial \mathbf{X}_2} & 0 & 0 \\ 0 & 0 & \frac{\partial}{\partial \mathbf{X}_1} & \frac{\partial}{\partial \mathbf{X}_2} \end{bmatrix}, \tag{4.18b}$$

with F_{11} etc the components of the deformation gradient $\mathbf{F}$.

Finally, the tangential stiffness matrix can be derived which conventionally consists of a material and a geometric contribution. The material stiffness matrix reads:

$$\mathbf{K}_{\mathrm{mat}} := \begin{bmatrix} \mathbf{K}_{\mathrm{mat}}^{\mathrm{aa}} & \mathbf{K}_{\mathrm{mat}}^{\mathrm{ab}} \\ \mathbf{K}_{\mathrm{mat}}^{\mathrm{ba}} & \mathbf{K}_{\mathrm{mat}}^{\mathrm{bb}} \end{bmatrix} \tag{4.19}$$

where

$$\mathbf{K}^{\mathrm{aa}}_{\mathrm{mat}} = \int_{\Omega_0} \mathbf{B}^{\mathbf{T}}_{\mathrm{N}} \mathbb{C} \mathbf{B}_{\mathrm{N}} \, \mathrm{d}\Omega_0 \tag{4.20}$$

$$\mathbf{K}^{\mathrm{ab}}_{\mathrm{mat}} = \int_{\Omega_0} \mathcal{H}_{\Gamma_{\mathrm{d},0}} \mathbf{B}^{\mathbf{T}}_{\mathrm{N}} \mathbb{C} \mathbf{B}_{\mathrm{N}} \, \mathrm{d}\Omega_0 \tag{4.21}$$

$$\mathbf{K}^{\mathrm{ba}}_{\mathrm{mat}} = \int_{\Omega_0} \mathcal{H}_{\Gamma_{\mathrm{d},0}} \mathbf{B}^{\mathbf{T}}_{\mathrm{N}} \mathbb{C} \mathbf{B}_{\mathrm{N}} \, \mathrm{d}\Omega_0 \tag{4.22}$$

$$\mathbf{K}^{\mathrm{bb}}_{\mathrm{mat}} = \int_{\Omega_0} \mathbf{B}^{\mathbf{T}}_{\mathrm{N}} \mathbb{C} \mathbf{B}_{\mathrm{N}} \, \mathrm{d}\Omega_0 + 4 \int_{\Gamma_{\mathrm{d},0}} \mathbf{R}^{\mathrm{T}} \mathbf{Q}^{\mathrm{T}} \mathbf{T}_d \mathbf{Q} \mathbf{R} \, \mathrm{d}\Gamma_0 \tag{4.23}$$

where $\mathbb{C}$ is the linearised material stiffness in the reference configuration, and $\mathbf{T}_d$ indicates the tangent of cohesive tractions. $\mathbf{Q}$ denotes the rotation matrix.

Defining

$$\bar{\mathbf{\Sigma}} := \begin{bmatrix} \Sigma_{11} & \Sigma_{12} & 0 & 0 \\ \Sigma_{21} & \Sigma_{22} & 0 & 0 \\ 0 & 0 & \Sigma_{11} & \Sigma_{12} \\ 0 & 0 & \Sigma_{21} & \Sigma_{22} \end{bmatrix} \tag{4.24}$$

$$\bar{\mathbf{R}} := \begin{bmatrix} \mathbf{R}_1 & \cdots & \mathbf{R}_{n_{\mathrm{enr}}} & 0 & \cdots & 0 \\ 0 & \cdots & 0 & \mathbf{R}_1 & \cdots & \mathbf{R}_{n_{\mathrm{enr}}} \end{bmatrix} \tag{4.25}$$

$$\bar{\mathbf{t}}_{\mathrm{d},0} := \begin{bmatrix} \bar{\mathrm{t}}_{\mathrm{d},0_1} & \bar{\mathrm{t}}_{\mathrm{d},0_2} & 0 & 0 \\ 0 & 0 & \bar{\mathrm{t}}_{\mathrm{d},0_1} & \bar{\mathrm{t}}_{\mathrm{d},0_2} \end{bmatrix} \tag{4.26}$$

where n_{enr} is the number of enriched control points within the element under consideration, the geometric stiffness matrix can be derived as:

$$\mathbf{K}_{\mathrm{geo}} := \begin{bmatrix} \mathbf{K}^{\mathrm{aa}}_{\mathrm{geo}} & \mathbf{K}^{\mathrm{ab}}_{\mathrm{geo}} \\ \mathbf{K}^{\mathrm{ba}}_{\mathrm{geo}} & \mathbf{K}^{\mathrm{bb}}_{\mathrm{geo}} \end{bmatrix} \tag{4.27}$$

$$\mathbf{K}^{\mathrm{aa}}_{\mathrm{geo}} = \int_{\Omega_0} \mathbf{B}^{\mathbf{T}}_{\mathrm{G}} \bar{\mathbf{\Sigma}} \, \mathbf{B}_{\mathrm{G}} \, \mathrm{d}\Omega_0 \tag{4.28}$$

$$\mathbf{K}^{\mathrm{ab}}_{\mathrm{geo}} = \int_{\Omega_0} \mathcal{H}_{\Gamma_{d,0}} \mathbf{B}^{\mathbf{T}}_{\mathrm{G}} \bar{\mathbf{\Sigma}} \, \mathbf{B}_{\mathrm{G}} \, \mathrm{d}\Omega_0 \tag{4.29}$$

$$\mathbf{K}^{\mathrm{ba}}_{\mathrm{geo}} = \int_{\Omega_0} \mathcal{H}_{\Gamma_{\mathrm{d},0}} \mathbf{B}^{\mathbf{T}}_{\mathrm{G}} \bar{\mathbf{\Sigma}} \, \mathbf{B}_{\mathrm{G}} \, \mathrm{d}\Omega_0 + 2 \int_{\Gamma_{\mathrm{d},0}} \bar{\mathbf{R}}^{\mathbf{T}} \, \bar{\mathbf{t}}_{\mathrm{d},0} \, \mathbf{B}_{\mathrm{G}} \, \mathrm{d}\Gamma_0 \tag{4.30}$$

$$\mathbf{K}^{\mathrm{bb}}_{\mathrm{geo}} = \int_{\Omega_0} \mathbf{B}^{\mathbf{T}}_{\mathrm{G}} \bar{\mathbf{\Sigma}} \, \mathbf{B}_{\mathrm{G}} \, \mathrm{d}\Omega_0 + 2 \int_{\Gamma_{\mathrm{d},0}} \mathcal{H}_{\Gamma_{\mathrm{d},0}} \bar{\mathbf{R}}^{\mathbf{T}} \, \bar{\mathbf{t}}_{\mathrm{d},0} \, \mathbf{B}_{\mathrm{G}} \, \mathrm{d}\Gamma_0. \tag{4.31}$$

Although the value of the Heaviside function at the crack path $\Gamma_{\mathrm{d},0}$ equals zero, the last term in the Equation 4.31 remains owing to compatibility enforcement.

4.5 Implementation Aspects

For isogeometric analysis the shared inter-element control points complicate the enrichment and the imposition of compatibility between multiple displacement fields which are adopted for XIGA. To keep the chapter self-contained, the key points are summarised concisely below [44].

4.5.1 Compatibility enforcement

Shifting and *blending* techniques [44] are utilised to enforce compatibility. Unlike extended finite element analysis, where the Lagrange interpolation localises the shifted Heaviside function within the cracked elements, shifting now narrows this effect to the adjacent elements perpendicular to the crack path, see Figure 3.3. This is caused by the $\mathcal{C}^0$-continuity in standard finite elements and the higher-order NURBS in isogeometric analysis at the element boundaries. The latter leads to a stretch of the discontinuity effect over multiple rows of elements, which is different from the single row of cracked elements in XFEM. Shifting should be applied to all the discontinuous terms, i.e. to all the Heaviside terms in the discretised equations. For the same reason the Heaviside function which appears in front of the crack tip is redundant and should be removed. Therefore, a step function must be used as the blending technique [44]. Shifted basis functions are illustrated for a univariate and bivariate NURBS bases in Figures 3.3 and 3.4 for intact and cracked media.

A plate with 7 equally distanced elements is shown in Figure 4.3. The crack is located in the centre of the plate, inside the 4th element. The enhanced control points are illustrated by red asterisks. As noted before, compatibility enforcement aims to localise the effect of the Heaviside function to the cracked element, but this fails when using B-splines owing to the fact that control points are shared. Figure 4.3 illustrates the values of the shifted Heaviside function for the enhanced points (red asterisks), which are supposed to be zero. For the asterisks above and below the crack path, however, these values render the undesired enhanced field to become non-zero at the location of the control points, see the last term in Equation (4.14). Our observations suggest omitting this undesired term during the position field update. Otherwise, it slows down the convergence rate, possibly leading to a divergence of the solution. This suggests that the compatibility between the two fields has not been enforced fully.

It is recalled that the discretised formulation which derives from the variational formulation is neither shifted nor blended, and these technique affect only after discretisation [44]. Accordingly, for shifting technique, the Heaviside function becomes $\mathcal{H}_{\Gamma_{\mathrm{d},0}} - \mathcal{H}_0^{\mathbb{B}}$, where $\mathcal{H}_0^{\mathbb{B}}$ denotes the value of the Heaviside function for control points in the reference configuration. Therefore, based on the Heaviside sign function, $\mathcal{H}_{\Gamma_{\mathrm{d},0}}$ becomes zero, but $\mathcal{H}_0^{\mathbb{B}}$ will contain

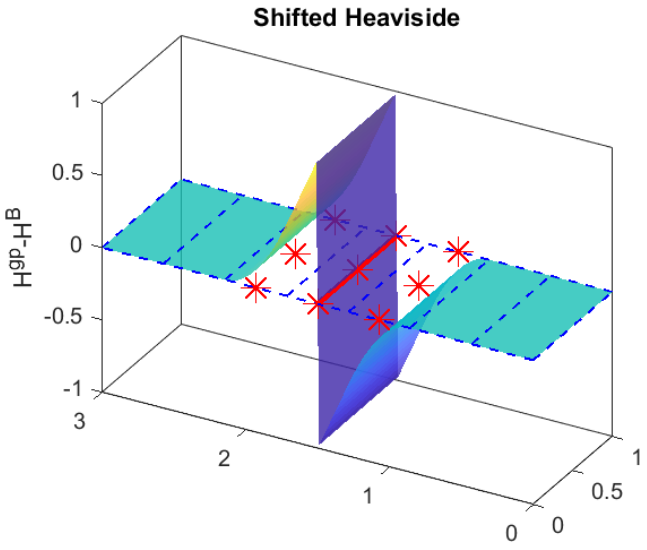

Figure 4.3: Domain excess of the shifted Heaviside from the cracked element. Red asterisks denote the enhanced control points, where the shifted Heaviside value differs from zero. H^{gp} and $H^{\mathbb{B}}$ denote Heaviside values for Gauss points and control points, respectively.

either of the values -1, 0 or 1, which makes that this term is preserved.

4.5.2 Other implementation aspects

Crack extension Several factors must be considered when propagating a crack, e.g. the direction of crack extension, the propagation criterion and the geometry of the extension. Similar to XFEM [143] and XIGA [44], a nonlocal approach is adopted here to mitigate an inaccurate local estimation of the stresses, even though isogeometric analysis already improves the stress fields [44]. Once the crack path has been found, the stresses along the path are compared with the fracture strength. Herein, propagation is assumed to occur when half of the Gauss points along the crack path satisfy $\sigma_y^{loc} \geq f_t$. Then, the crack propagates as a straight line through the element and the crack tip is defined at the intesection of crack path and the edge of the element, see Figure 3.5b. It is noted that in a part of the new crack path the fracture criterion may not yet have been met. Adopting a blending technique, these sections will be omitted from the integration process [44].

Enhancement of individual control points As mentioned before, the crack crosses the element entirely in the form of a straight line, finishing at the edge of the element. Enrichment of the element follows the crack tip[2]: points at or in front of the crack tip will be precluded

[2]Note the difference between crack tip and real crack tip shown in Section 3.3

for cohesive fracture. It is emphasised that the inter-element sharing of the control points causes this complication, which is different for XFEM because of the $\mathcal{C}^0$-continuity.

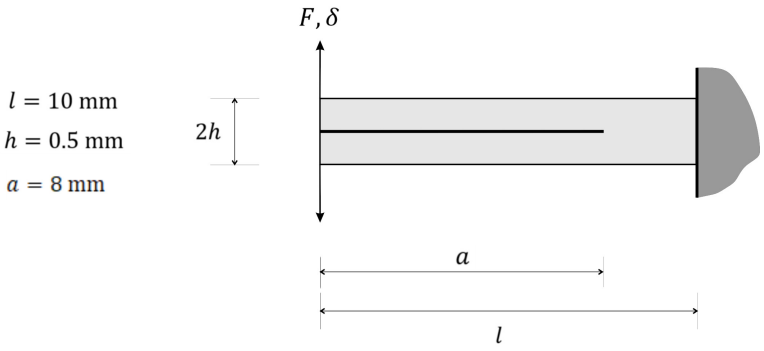

Figure 4.4: Double Cantilever Beam with a traction-free initial slit. Propagation is prevented. F and δ are the force and displacement, respectively.

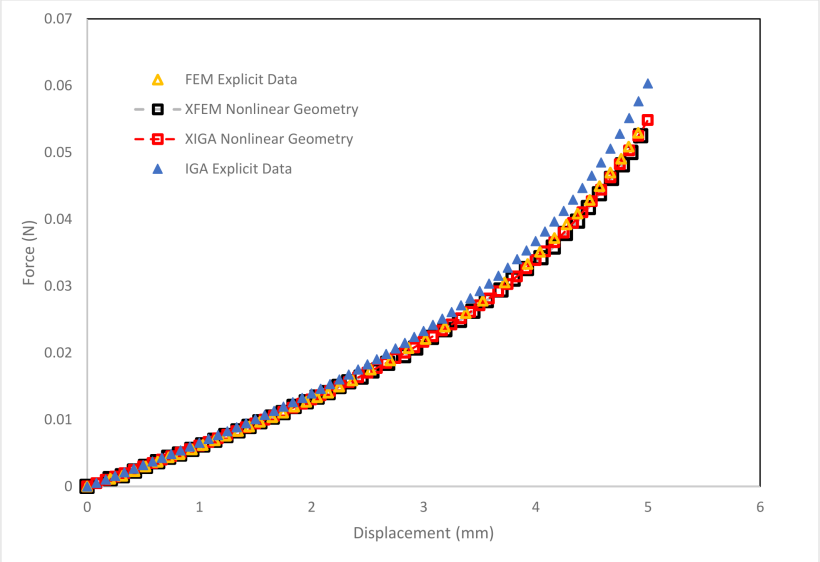

Figure 4.5: Results of the explicitly modelled fixed interface for a DCB.

Intergration scheme and point projection Herein, Gauss integration scheme is adopted for any integration operation. A sub-triangulation technique is utilised for elements crossed by the crack path to guarantee a sufficient number of Gauss points at each side of the crack. To impose the cohesive tractions on the crack path, line integration is required. Exploiting interface elements [1, 114, 141, 28], degrees of freedom are defined explicitly for the crack path, i.e. there exists a physical definition of the discontinuity. In an extended approach, however, the discontinuity is embedded inside the element. The mesh can be unstructured and degrees of freedom belong to the element, not to the discontinuity. Hence, in order to

integrate the line on the element's degrees of freedom, natural coordinates on the parent line should be mapped onto the parent square while the location of crack inside the element being considered. This requires a point projection scheme [44], discussed in Section 2.1.5.

4.6 Numerical examples

Some numerical examples are presented to validate and illustrate the method and the implementation aspects. The examples each aim to verify a specific aspect, one at a time. The results are compared with findings from XFEM [143].

4.6.1 Explicit and enhanced discontinuity modelling: Double Cantilever Beam

The first example assesses the geometric nonlinearity in the presence of a discontinuity. This is done in two ways, by means of a non-progressing, explicit interface and by a peel test. A Double Cantilever Beam (DCB) is exploited for both cases.

Explicit interface

A traction-free slit is modelled, see Figure 4.4, while crack propagation is prevented. Young's modulus and Poisson's ratio are taken as $E = 100$ MPa and $\nu = 0.3$, respectively. The analysis comprises of two approaches, interface elements and the extended approach. The results are compared with those from corresponding finite element analyses.

Overall, there is an excellent agreement between the results from XIGA and those from XFEM. There is a slight difference between IGA and FEM interface elements at the last few loading steps, but this is negligible (see Figure 4.5). The reason lies in the use of dummy stiffness to prevent delamination in front of the slit. Since control points are shared between elements in isogeometric analysis, the use of a dummy stiffness renders the last delaminated interface element semi-open (because of the last control point of this element being shared with the first intact element after delamination). This results in a stiffer response from IGA interface element approach when the opening reaches the end of the delamination, i.e. at the last loading steps. Since a dummy stiffness is not needed in extended approaches, there is no difference between the results from XFEM and XIGA.

Peel test

Next, the crack is allowed to propagate. The initial slit is now 1 mm, see the geometry of Figure 4.6. The same material properties have been adopted as in the previous section, while the tensile stress and the fracture energy are taken as $f_t = 1$ MPa and $G_f = 0.05$ N $\cdot$ mm^{-1}, respectively. Only the extended approach is now used.

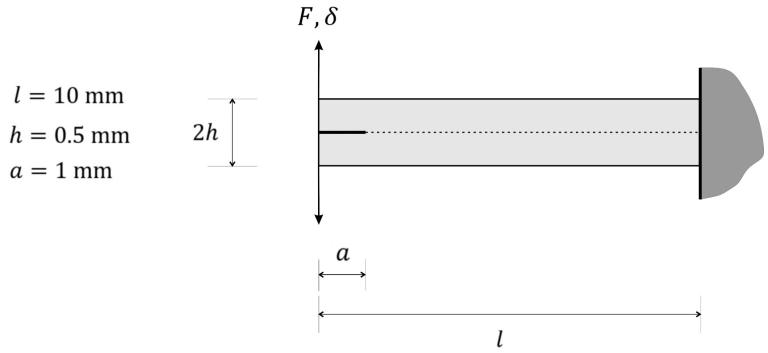

Figure 4.6: Crack propagation for a Double Cantilever Beam under mode-I loading.

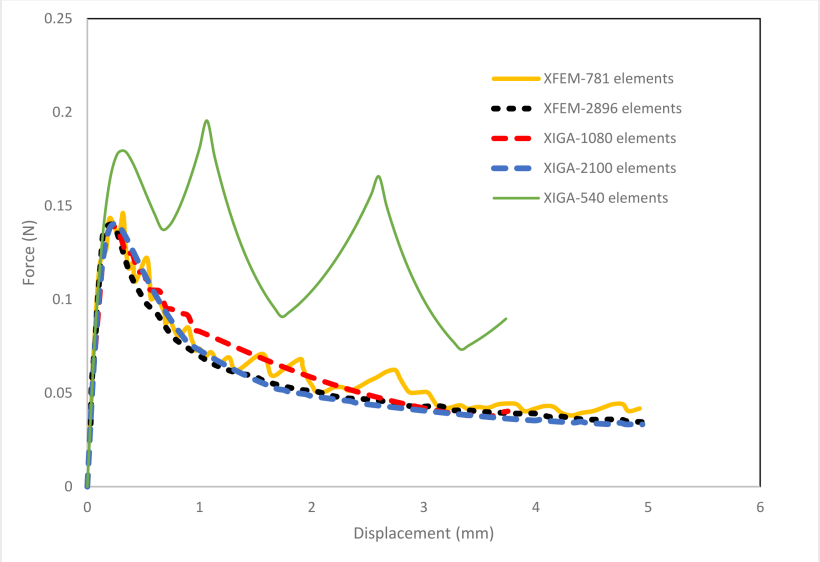

Figure 4.7: Results of the peel test for a Double Cantilever Beam.

The results are shown in Figure 4.7. We observe that XIGA converges, concluded with the finest mesh (blue dashed line with 2100 elements) coarser than the finest mesh utilised in XFEM (black dashed line with 2896 elements). Also the red dashed line (XIGA 1080 elements) is smoother than the yellow line (XFEM 781 elements). Though the peak loads are the same, the responses are slightly different. The coarsest mesh for XIGA (540 elements denoted by the green line) widely differs from the other results, indicating that the spatial resolution is insufficient. Preserving the higher-order continuity across element boundaries in IGA, the shifting technique is unable to fully localise the enhanced term to the cracked elements (see Figure 4.3). This undesired excess of the enhanced field introduces a source of error whose effect is proportional to the element size, i.e. errors become negligible with fairly fine meshes. This trend is observed for the XIGA results in Figure 4.7. Noteworthy

is that such error is absent in XFEM due to $\mathcal{C}^0$-continuity of the Lagrange interpolation at element boundaries, where shifting technique confines the enhanced field to the cracked elements. Nevertheless, the finest XIGA mesh is still coarser than that of XFEM, indicating the slightly better performance of XIGA compared to XFEM.

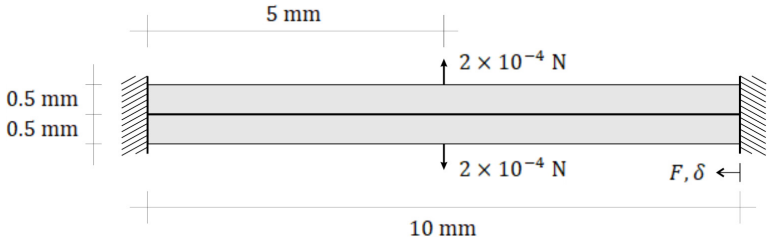

Figure 4.8: Axial compression applied to a Double Cantilever Beam to trigger a buckling mode.

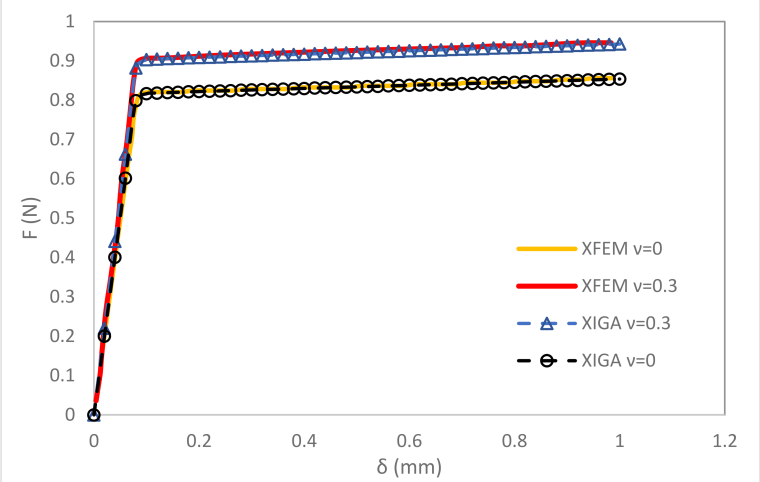

Figure 4.9: Numerical results for the buckling test.

4.6.2 Geometric instability: buckling in composites

To investigate the capability of the formulation to handle geometric instabilities, a buckling test is examined. The Double Cantilever Beam of Figure 4.8 with a small perturbation (two small lateral loads) is subjected to an axial compressive load. It is assumed that the delamination has happened throughout the beam, as illustrated by the solid black line, and no cohesive tractions exist at the interface. Young's modulus is again taken as $E = 100$ MPa, while two values are adopted for Poisson's ratio: $\nu = 0$ and $\nu = 0.3$.

An excellent agreement is observed between the present results for XIGA and those for XFEM [143] for both values of Poisson's ratio, see Figure 4.9. Noteworthy is that fewer elements are needed in the XIGA simulation (355 elements) compared to that of XFEM (781

elements), which is to be expected given the higher inter-element continuity in XIGA. The critical load (for a single beam) for $\nu = 0$ matches the Euler buckling load: $P_{\text{crit}} = \frac{4\pi^2 EI}{L^2} \approx 0.4112$. The deformed configuration is given in Figure 4.10.

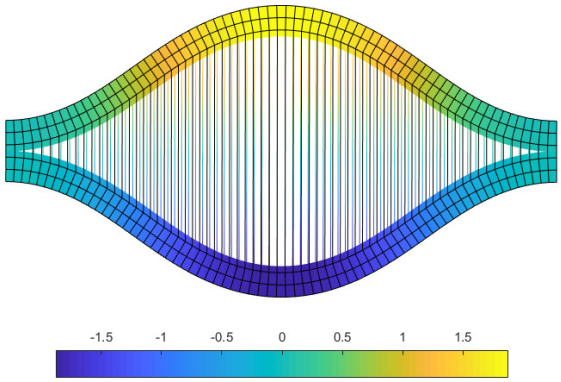

Figure 4.10: Deformed shape of the buckling test. Colours indicate the displacement in the y-direction, and numbers in the colour bar are given in millimeters.

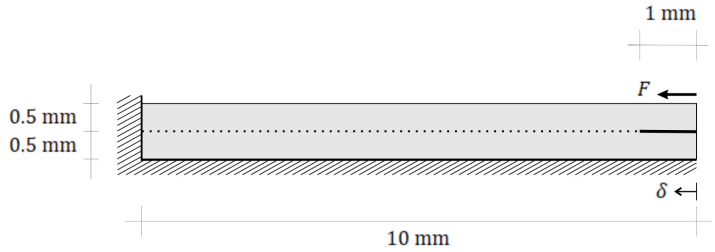

Figure 4.11: A peel test from a stiff substrate.

Table 4.1: Energy residuals including/excluding the Linearised Interface Tangent (LIT).

i	XIGA with LIT	XIGA without LIT	XFEM with LIT	XFEM without LIT
0	7.64×10^{-2}	8.40×10^{-2}	3.13×10^{0}	3.04×10^{0}
1	6.08×10^{-5}	4.30×10^{-4}	5.62×10^{-2}	3.58×10^{-2}
2	1.13×10^{-6}	2.53×10^{-7}	4.13×10^{-5}	4.72×10^{-4}
3	3.72×10^{-10}	2.05×10^{-13}	4.38×10^{-8}	3.00×10^{-6}
4			5.56×10^{-11}	1.06×10^{-8}
5				4.35×10^{-11}

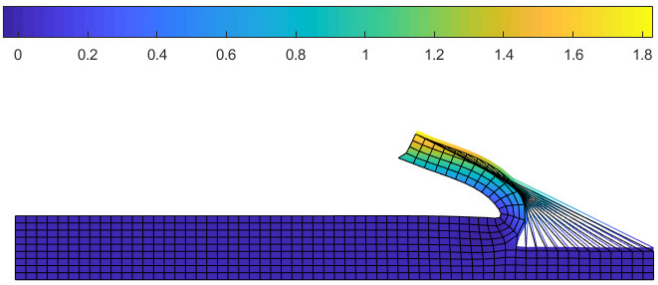

Figure 4.12: Deformed shape of a peel test from a stiff substrate at $u = 4$ mm (no magnification). Values of the colour bar are given in millimeters, and colours denote the displacement in the y-direction.

4.6.3 Effect of the linearised interface tangent: Peel test from a stiff substrate

The last example tests the linearisation of the stiffness terms at the interface. For this purpose, a layer is peeled from a stiff substrate, resulting in severe rotations. There is an initial slit of 1 mm, see Figure 4.11, and from there the delamination follows the path indicated by the dotted. A cohesive-zone model has now been adopted with a constant residual value equal to the fracture strength. This is to fully maintain the geometric contribution of cohesive tractions and their linearised tangent terms. Hence, at the onset of the peeling the normal tractions equal f_t and the material contribution to the interface tangent stiffness matrix becomes zero [143]. The material properties read: Young's modulus $E = 100$ MPa, Poisson's ratio $\nu = 0.3$ and fracture strenght $f_t = 2$ MPa. The deformed shape is illustrated in Figure 4.12.

From Table 4.1 XIGA clearly converges faster than XFEM, which can probably be attributed to the smoother stress distribution in the XIGA simulations. Another possible explanation is that compatibility is not completely enforced in the linearised interface tangent terms in XFEM, as mentioned before. Compatibility enforcement directly affects the nodal points to become interpolatory and subsequently makes the convergence optimal.

4.7 Concluding remarks

EXtended IsoGeometric Analysis has been formulated for geometric nonlinearity and cohesive fracture. The use of a sign function rather than a Heaviside step function has removed the need to make an assumption for the normal to the centreline of the crack. The formulation has been elaborated using a Total Lagrangian Formalism and the corresponding weak forms have been derived. This also facilitates avoiding the undesired enhanced field in the elements adjacent to the cracked ones to contribute to updating the position field in the

Updated Lagrangian formalism, i.e. elimination of a source of error which may aggravate the convergence. Moreover, using the reference configuration removes any difficulty about the computation of the crack opening and subsequently the traction-opening relationship in the current configuration, especially while severe rotations are confronted. The isogeometric formulation has been cast in a standard finite element framework using Bézier extraction. Difficulties related to the higher-order continuity of the isogeometric formulation have been discussed, including compatibility enforcement.

A main area of application is the analysis of failure of fibre-reinforced, laminated composites. A variety of examples have been examined including buckling of a delaminated beam and peeling a strip from a stiff substrate, which involves large rotations and assesses the good performance of the sign function compared to the step function. In terms of degrees of freedom and convergence of the nonlinear solver the isogeometric formulation seems slightly superior to a standard formulation using Lagrangian interpolants.

Chapter 5

IGA Enhanced with Local Maximum Entropy

In this chapter[1], an extended approach is developed by blending isogeometric analysis and the first-order local maximum entropy for the standard and the enhanced fields, respectively. Isogeometric analysis facilitates the accurate parametrisation of the geometry in general, particularly the exact geometric parametrisation of the conic curves and quadratic surfaces using NURBS. On the other hand, the local maximum entropy leads to an improved estimate for the enhanced part due to its infinite continuity. Moreover, local maximum entropy paves the way to a non-elementwise crack propagation owing to its meshfree characteristic. To enforce compatibility, the shifting technique is amended for the meshfree enhanced part to localise the effect of the Heaviside function to a narrow region around the crack. Next, a blending technique is exploited to remove the effect of the discontinuity in front of the crack tip. The viability of the approach is illustrated at the hand of several examples comprising straight and curved crack propagation.

5.1 Research Background

The classical approach to simulate discrete fracture is the use of interface elements [114, 72, 141, 28]. The method is suitable and straightforward when the crack path is known *a priori*. For arbitrary crack paths the method is more cumbersome, as advanced remeshing schemes have to be used, but successful applications have been reported, in the context of Linear Elastic Fracture Mechanics (LEFM) [68] as well as for cohesive fracture [118].

[1]This chapter is directly adopted from:

Fathi, F., Chen, L. and de Borst, R., 2021. X-IGALME: Isogeometric analysis extended with local maximum entropy for fracture analysis. International Journal for Numerical Methods in Engineering.

The eXtended Finite Element Method (XFEM) offers an elegant alternative and can capture an arbitrary-shaped discontinuity independent of the original mesh layout by exploiting the partition of unity property of the shape functions. The approach utilises an additional set of discontinuous functions with extra degrees of freedom, potentially different from the regular degrees of freedom, and discontinuities can run through elements. As for remeshing, the method has been developed for LEFM [15, 91, 51] as well as for cohesive fracture [144, 103]. It is finally noted that the method can be considered as a generalisation of interface elements, where discontinuity is put at the edge of elements rather than inside.

The finite element normally uses Lagrange shape functions, which leads to a $\mathcal{C}^0$-continuity across element boundaries. To provide a higher-continuity across element boundaries and, especially, to capture the geometry exactly, Lagrange interpolation functions have been replaced by Non-Uniform Rational B-Splines (NURBS), and the resulting method has been named Isogeometric Analysis (IGA) [30]. Unfortunately, the tensor-product structure of NURBS makes them not very suitable for the simulation of discrete crack propagation. There are several solutions, including the use of T-splines [138, 29], splines which are based on triangles, so-called Powell-Sabin B-Splines [87, 27] and an approach which is similar to that of XFEM and exploits the partition-of-unity property of NURBS. This method has been coined eXtended Isogeometric Analysis (XIGA). It was originally proposed by De Luycker *et al.* [39] for LEFM. Recently, the approach has been developed for cohesive fracture [44] and has been extended to geometric nonlinearity [46].

Maximum entropy (*max-ent*) – a principle to obtain the least biased statistical inference in the absence of sufficient knowledge – is a means to find the current state of an ensemble whose probabilities form a partition of unity [128]. Applications encompass diverse fields, including engineering, where it has been used to obtain the minimally biased interpolation on a polygonal domain [128, 108], among other applications. To localise the support of *max-ent* basis functions *Local* Maximum Entropy (LME) has been developed [6]. First-order LME approximants are non-negative on a convex hull of the ensemble, while for the extension to a higher-order approximants the non-negativity assumption is generally dropped [19]. Nevertheless, positivity and smoothness of the basis functions can be preserved for higher-order approximants, for instance within a second-order convex maximum entropy approach [110].

Among meshfree approaches *max-ent* holds some superior features, including positivity of the basis functions, robustness of the solution, a straightforward quadrature rule, and a weak Kronecker-delta property at boundaries, which facilitates the imposition of essential boundary conditions [6, 109]. The meshfree shape functions are unbounded, forming a local support around the point under consideration. This locality is adjustable through a parameter to

control the size of the support [6, 109, 65]. Therefore, the supports of the basis functions overlap, similar to isogeometric analysis.

As with other meshfree approaches, the main drawback is the poor approximation of complex boundaries. This has been solved by incorporating Isogeometric Analysis (IGA), e.g. by coupling IGA with the Reproducing Kernel Particle Method (RKPM) [135] and with *max-ent*-based approximants via a duality method [108]. From the computational cost perspective, meshfree approaches such as RKPM and EFG are less costly compared to LME, since they only solve a linear system of equations instead of a nonlinear problem. Recently, the LME strategy has been improved by anisotropy in the basis function support to account for directional variations in nodal spacing, and a remedy for the tensile instability observed in most meshfree approaches [82]. In the realm of Linear Elastic Fracture Mechanics, Local Maximum Entropy has been cast in the extended framework (XLME) for the standard and the enhanced sections [5]. XLME, indeed, improves the performance compared to XFEM, which is proven for different errors benchmarked against well-established LEFM problems. Compatibility enforcement [77, 39], however, has not been considered for XLME to confine the effect of the enhanced field perpendicular and parallel to the crack path [39, 44]. Moreover, while all the examples are merely limited to straight fracture with no propagation, the efficacy of this approach on arbitrary crack propagation in an iterative nonlinear problem is interesting to explore.

Herein, we aim to exploit IGA and LME in an extended approach, where the former is the standard part which represents the geometry exactly and the latter captures the localised high gradient which results from the discontinuity. Similar to the higher-order continuity $\mathcal{C}^p$, $p > 1$, provided by isogeometric analysis, smoothness of basis functions is an advantage of meshfree methods. In particular, *max-ent* returns $\mathcal{C}^\infty$-continuity which is better than in isogeometric analysis [109]. This, for instance, can be exploited when solving higher-order differential equations, e.g. the Cahn-Hilliard equation [54, 76]. Recent research on XIGA for cohesive fracture and the difficulties encountered for element-wise enrichment of the individual control points with higher-order continuities [44] have motivated this blending, coined X-IGALME. By setting LME as the enhanced part in the extended approach, an improved stress estimation and consequently, a better crack propagation direction is expected. This complements the improved estimation of the crack extension direction by the standard IGA part due to its higher-order inter-element continuity.

This chapter continues with a succinct discussion of the governing equations in the bulk and at the discontinuity. The IGA and LME formulations are presented for the standard and the enhanced parts as the main ingredients for X-IGALME. Next, implementation aspects, which encompass compatibility, enrichment and crack extension, are covered. The

chapter concludes with some case studies, which assess the NURBS order and the effect of the dimensionless aspect ratio on the energy dissipation for straight and curved crack profiles.

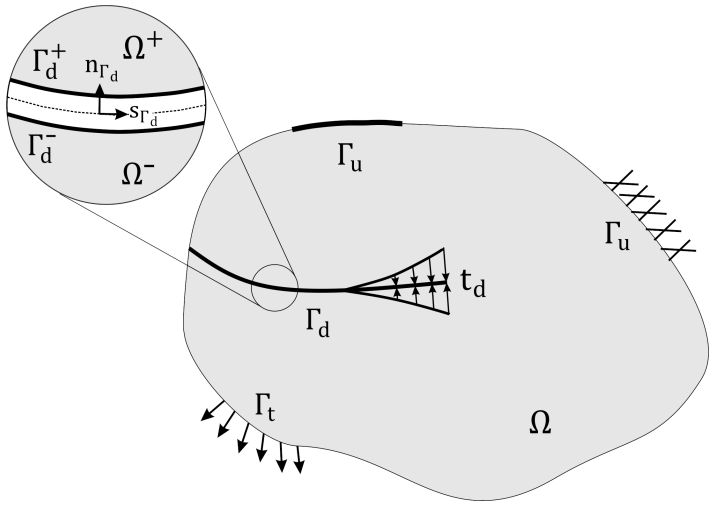

Figure 5.1: Boundary value problem Ω with the discontinuity Γ_d and cohesive tractions $\mathbf{t}_d$.

5.2 Governing Equations

A rate-independent, isotropic linear elasticity is adopted for the bulk, while a cohesive-zone model governs the behaviour at the discontinuity, see Figure 5.1.

5.2.1 Cohesive-zone model

As detailed in Section 2.2.3, an exponentially decaying function governs the relation between the local tractions normal to the discontinuity and the relative opening:

$$t_n^{\text{loc}} = f_t \exp\left(-\frac{f_t}{G_f}\kappa\right), \tag{5.1}$$

where κ denotes a history parameter. f_t and G_f indicate the fracture strength and the fracture energy, respectively. Using the rotation matrix this relation can be transformed from local to global coordinate system and can subsequently linearised for use in a Newton-Raphson iterative scheme. To obtain a symmetric stiffness matrix, the shear stiffness must be neglected, which holds true for mode-I dominated fracture problems, and is the case in all the examples. Kuhn-Tucker conditions govern loading/unloading behaviour:

$$f\left(\llbracket u_n \rrbracket, \kappa\right) = \llbracket u_n \rrbracket - \kappa \leq 0 \qquad \dot{\kappa} \geq 0 \qquad \dot{\kappa} f = 0 \ , \tag{5.2}$$

where $[\![u_n]\!]$ is the displacement jump normal to the crack and κ denotes the history parameter.

5.2.2 Kinematics of displacement discontinuity

In the absence of acceleration and body forces, the equilibrium equation and the boundary conditions read (see Figure 5.1):

$$\begin{cases} \nabla \cdot \boldsymbol{\sigma} = & 0 & \mathbf{x} \in \Omega \\ \mathbf{u} = & \overline{\mathbf{u}} & \mathbf{x} \in \Gamma_u \\ \mathbf{n} \cdot \boldsymbol{\sigma} = & \overline{\mathbf{t}} & \mathbf{x} \in \Gamma_t \\ \mathbf{n}_{\Gamma_d} \cdot \boldsymbol{\sigma} = & \mathbf{t}_d & \mathbf{x} \in \Gamma_d \end{cases}, \tag{5.3}$$

where $\boldsymbol{\sigma}$ is the Cauchy stress tensor, and $\overline{\mathbf{u}}$ and $\overline{\mathbf{t}}$ are the prescribed displacement and traction, respectively. The vector normal to the external traction surface is defined as $\mathbf{n}$, and $\mathbf{n}_{\Gamma_d}$ denotes the vector normal to the crack surface. The linear-elastic stress-strain relation for the bulk material is:

$$\boldsymbol{\sigma} = \mathbf{D} : \boldsymbol{\epsilon}, \tag{5.4}$$

where $\mathbf{D}$ is the fourth-order linear-elastic stiffness tensor.

In an extended finite element approach the displacement field is separated into regular and (possibly multiple) enhanced fields [15, 91, 144, 103, 51, 44]. It is noted that the partition of unity property of interpolation functions is the requirement for this separation, and also applies to shape functions used in meshless methods and in isogeometric analysis. The regular degrees of freedom $\mathbf{a}$ represent the regular continuous displacement field, and the enhanced degrees of freedom $\mathbf{b}$ are used for the parameterisation of the additional displacement field:

$$\mathbf{u}(\mathbf{x}) = \mathbf{N}(\mathbf{x})\mathbf{a} + \mathcal{H}_{\Gamma_d}(\mathbf{x})\tilde{\mathbf{N}}(\mathbf{x})\mathbf{b}, \tag{5.5}$$

where $\mathbf{N}$ and $\tilde{\mathbf{N}}$ contain the basis functions of the standard and the enhanced fields, respectively. $\mathcal{H}_{\Gamma_d}$ is the enrichment function which determines the character of the discontinuity. Herein, a sign function is utilised for modelling the crack as a strong discontinuity [44]. Assuming small strains, the symmetrised gradient of Equation (5.5) reads:

$$\boldsymbol{\epsilon} = \mathbf{B}\mathbf{a} + \mathcal{H}_{\Gamma_d}\tilde{\mathbf{B}}\mathbf{b} + 2\left(\delta_{\Gamma_d}\mathbb{n}_{\Gamma_d}\right)\tilde{\mathbf{N}}\mathbf{b}, \tag{5.6}$$

where $\mathbf{B}$ and $\tilde{\mathbf{B}}$ are the matrices which contain the derivatives of the set of basis functions $\mathbf{N}$ and $\tilde{\mathbf{N}}$, respectively. δ_{Γ_d} is the Dirac delta function and $\mathbb{n}_{\Gamma_d}$ contains components of $\mathbf{n}_{\Gamma_d}$ [44].

5.3 X-IGALME

Both IGA and LME form a partition of unity, which is required within an extended approach to employ multiple fields. Also, they both maintain higher continuity, although in a different manner. While this term usually denotes the presence of a higher inter-element continuity in IGA, it is defined locally in LME since the notion of an element is meaningless in a meshless approach. Therefore, the terminology "higher order" denotes the $\mathcal{C}^\infty$-continuity for the ensemble, or more precisely, for the support cloud of the nominated local point. This provides a potential for higher accuracy compared to finite element approaches, including IGA. Noteworthy is that the higher accuracy results is assured for smooth problems [6], while it is yet to be confirmed for non-smooth problems. The localisation parameter to control the width of the meshfree basis functions also provides a more versatile approach to enforce compatibility, which is of paramount importance for enriched approaches in returning the correct solution and/or optimum convergence [44, 46].

5.3.1 NURBS for the standard section

To define the ingredient for the standard part, NURBS is briefly reviewed similar to Section 2.1.2. NURBS basis functions, i.e. weighted B-spline basis functions, can accurately parametrise conic shapes, a characteristic which has led to the use of NURBS in state-of-the-art Computer Aided Design (CAD). The geometry can be written as a linear combination of the NURBS basis functions $R_k(\xi)$, which map a parametric coordinate ξ onto the physical domain:

$$\mathbf{x}(\xi) = \sum_{k=1}^{n_{\text{IGA}}} R_k(\xi)\mathbf{P}_k, \tag{5.7}$$

where $\mathbf{P}$ is the set of control point coordinates and n_{IGA} is the number of control points. The weight w_k makes the difference between a B-spline basis function N_k and a NURBS basis function:

$$R_{k,p}(\xi) = \frac{w_k N_{k,p}}{W(\xi)}, \tag{5.8}$$

with p denoting the order of the underlying knot vector and $W(\xi) = \sum_{k=1}^{n} N_k(\xi)w_k$. B-spline basis functions are recursively defined by the Cox-de Boor formula [35]. To provide an element-wise framework in compliance with standard finite element data structures, Bézier extraction has been exploited [22, 34]. This facilitates the numerical integration, which is illustrated in Figure 2.1. The element-wise NURBS basis functions are defined as:

$$\mathbf{R}^e(\boldsymbol{\xi}) = \mathbf{W}^e\mathbf{C}^e\frac{\boldsymbol{\mathcal{B}}^e(\boldsymbol{\xi})}{W^e(\boldsymbol{\xi})}, \tag{5.9}$$

where $\mathbf{W}^e$ is the diagonal matrix of weights, $\boldsymbol{\mathcal{B}}^e$ is the set of basis functions containing Bernstein polynomials, and $\mathbf{C}^e$ is the Bézier extraction operator [44].

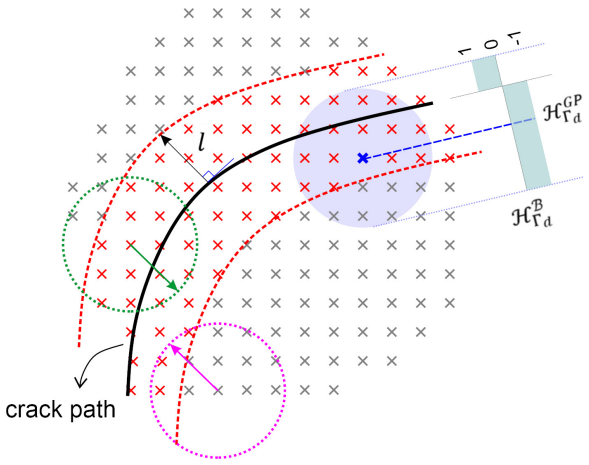

Figure 5.2: Compatibility enforcement via the shifting technique. Enriched points are indicated by red crosses, bounded by l-distanced offsets from the crack profile (see the dashed red lines). This region identifies those points with a support which intersects the crack path, i.e. comparing the dashed green circle with the magenta circle (both radius equals l). To represent the shifting technique, the values of the Heaviside function are illustrated for the blue point and its support (the purple shade). It is noted that $\mathcal{H}^{\mathcal{B}}_{\Gamma_d}$ and $\mathcal{H}^{GP}_{\Gamma_d}$ denote the Heaviside value for control points and the nominated Gauss point, respectively.

5.3.2 LME for the enhanced region

An ensemble $\mathbb{X}$ is considered as a subset of $\mathbb{R}^{n_{\text{dim}}}$, with n_{dim} is the dimension of the ensemble, so that the convex hull of the node-set reads [108],

$$\text{conv}\mathbb{X} = \left\{ \mathbf{x} \in \mathbb{R}^{n_{\text{dim}}} \mid \mathbf{x} = \sum_{l=1}^{n_{\text{LME}}} N_{\text{LME}_l} \mathbf{x}_l, \sum_{l=1}^{n_{\text{LME}}} N_{\text{LME}_l} = 1, N_{\text{LME}_l} \geq 0 \right\}, \tag{5.10}$$

where n_{LME} is the number of control points within the ensemble. The conditions in Equation (5.10) guarantee an exact approximation of an affine function [6]. Moreover, convexity is the requirement to maintain a weak Kronecker-delta property at the boundaries, which subsequently makes vanish the effect of internal bases at the boundary [108]. Therefore, similar to IGA, the geometry can be approximated as a linear combination of LME basis functions N_{LME_l}:

$$\mathbf{x} = \sum_{l=1}^{n_{\text{LME}}} N_{\text{LME}_l}(\mathbf{x})\, \mathbf{P}_l, \tag{5.11}$$

where $\mathbf{P}_l$ is the same set of control points defined for IGA which has been already adopted as the node-set $\mathbf{x}_l$ in Equation (5.10). LME basis function should form the zero-th and the

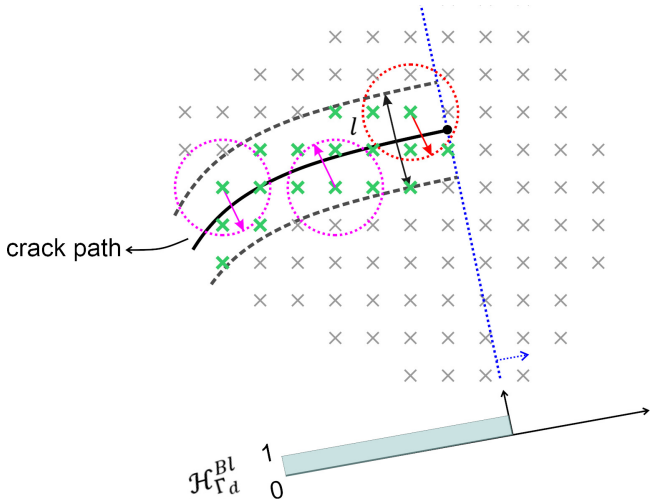

Figure 5.3: Compatibility enforcement via blending technique to impede the effect of enrichment in front of the crack tip (the black knot). Enrichment is also affected: points before the dotted blue line (the border between positive and negative tangential distance with respect to the crack tip) are enriched, which are indicated by green crosses. The blending Heaviside function acts like a weight function which removes the support excess of an enriched point with respect to the dashed blue line, e.g. the red dashed circle. The magenta dashed circles are completely inside the zone where $\mathcal{H}^{Bl}_{\Gamma_d} = 1$.

first-order consistency conditions in an $\varkappa$th-order equation:

$$\sum_{l=1}^{n_{\text{LME}}} N_{\text{LME}_l}(\mathbf{x})\, \mathbf{x}_l^{\varkappa} = \mathbf{x}^{\varkappa}, \qquad \varkappa = 0, 1. \tag{5.12}$$

The LME program can now be cast as a Pareto set, a platform to harmonise the unbiased estimation of *max-ent* and locality to control the width of basis functions [6]:

$$\begin{aligned} \text{LME}_\beta \qquad \text{For fixed } \mathbf{x} \text{ minimise} \qquad & \sum_{l=1}^{n_{\text{LME}}} N_{\text{LME}_l} \ln N_{\text{LME}_l} + \sum_{l=1}^{n_{\text{LME}}} \beta_l\, N_{\text{LME}_l}\, |\mathbf{x} - \mathbf{x}_l|^2 \\ \text{subject to} \qquad & N_{\text{LME}_l} \geq 0,\ l = 1, ..., n_{\text{LME}} \\ & \mathbf{x} = \sum_{l=1}^{n_{\text{LME}}} N_{\text{LME}_l}\, \mathbf{x}_l,\ \ \sum_{l=1}^{n_{\text{LME}}} N_{\text{LME}_l} = 1 \end{aligned} \tag{5.13}$$

where β is a non-negative parameter weighing which objective overrules the other. It can be defined in terms of a dimensionless aspect ratio[2] γ and the nodal spacing h_{node} as $\beta_l = \gamma_l / h^2_{\text{node}_l}$. The constraints subjected to the convex program guarantee non-negative meshfree

[2]It is reported as a dimensionless parameter which controls the locality of the basis function. No physical meaning has been reported to the author's best knowledge.

basis functions with $\mathcal{C}^\infty$-continuity [108]. Finally, the LME basis function reads [108, 6, 109],

$$N_{\mathrm{LME}_l}(\mathbf{x}) = \frac{1}{Z(\mathbf{x}, \boldsymbol{\lambda}^*)} \exp\left[-\beta_l |\mathbf{x} - \mathbf{x}_l|^2 + \boldsymbol{\lambda}^*(\mathbf{x}) \cdot (\mathbf{x} - \mathbf{x}_l)\right], \tag{5.14}$$

where

$$Z(\mathbf{x}, \boldsymbol{\lambda}) = \sum_{j=1}^{n_{\mathrm{LME}}} \exp\left[-\beta_j |\mathbf{x} - \mathbf{x}_j|^2 + \boldsymbol{\lambda}(\mathbf{x}) \cdot (\mathbf{x} - \mathbf{x}_j)\right] \tag{5.15}$$

and

$$\boldsymbol{\lambda}^*(\mathbf{x}) = \quad \arg \quad \min_{\boldsymbol{\lambda} \in \mathbb{R}^{n_{\mathrm{dim}}}} \quad \ln Z(\mathbf{x}, \boldsymbol{\lambda}). \tag{5.16}$$

Next, the derivatives of the LME basis functions are presented. To this end, the following functions are defined first [6, 109, 89]:

$$f_a(\mathbf{x}, \lambda, \beta_a) = -\beta_a |\mathbf{x} - \mathbf{x}_a|^2 + \lambda \cdot (\mathbf{x} - \mathbf{x}_a), \tag{5.17}$$

$$N_{\mathrm{LME}_a}(\mathbf{x}, \lambda, \boldsymbol{\beta}) = \frac{\exp[f_a(\mathbf{x}, \lambda, \beta_a)]}{Z(\mathbf{x}, \lambda, \boldsymbol{\beta})}, \tag{5.18}$$

where $Z(\mathbf{x}, \lambda, \boldsymbol{\beta}) = \sum_b \exp[f_b(\mathbf{x}, \lambda, \beta_b)]$ and

$$\mathbf{r}(\mathbf{x}, \lambda, \boldsymbol{\beta}) = \sum_a N_{\mathrm{LME}_a}(\mathbf{x}, \lambda, \boldsymbol{\beta})(\mathbf{x} - \mathbf{x}_a), \tag{5.19}$$

$$\mathbf{J}(\mathbf{x}, \lambda, \boldsymbol{\beta}) = \frac{\partial \mathbf{r}}{\partial \lambda} = \sum_a N_{\mathrm{LME}_a}(\mathbf{x}, \lambda, \boldsymbol{\beta})(\mathbf{x} - \mathbf{x}_a) \otimes (\mathbf{x} - \mathbf{x}_a) - \mathbf{r}(\mathbf{x}, \lambda, \boldsymbol{\beta}) \otimes \mathbf{r}(\mathbf{x}, \lambda, \boldsymbol{\beta}) \tag{5.20}$$

with a and b denoting the nodes. Recalling Equation 5.16, the superscript $*$ explicitly and implicitly relates the value of $\mathbf{x}$ and $\boldsymbol{\beta}$ [109]. Accordingly, any value within this superscript follows Equation 5.16 and falls into this dependency. It is noted that the LME basis function in Equation 5.14 is now denoted by N^*_{LME}. The first and second spatial derivatives (which equals the Hessian $\mathbb{H}$) read [89]:

$$\nabla N^*_{\mathrm{LME}_a} = N^*_{\mathrm{LME}_a}(\mathbf{r}_\beta - \mathbf{M}_a(\mathbf{x} - \mathbf{x}_a)) \tag{5.21}$$

and

$$\begin{aligned}\mathbb{H}N^*_{\mathrm{LME}_a} = N^*_{\mathrm{LME}_a}\left(\mathbf{r}_\beta - \mathbf{M}_a(\mathbf{x}-\mathbf{x}_a)\right)\otimes\left(\mathbf{r}_\beta - \mathbf{M}_a(\mathbf{x}-\mathbf{x}_a)\right) + 2N^*_{\mathrm{LME}_a}\left(\sum_b \beta_b N^*_{\mathrm{LME}_b} - \beta_a\right)\mathbf{1}\\ +N^*_{\mathrm{LME}_a}\left(\mathbf{r}_\beta\otimes\mathbf{r}_\beta + \mathbf{r}_\beta\otimes\mathbf{j}_a + \mathbf{j}_a\otimes\mathbf{r}_\beta + (\mathbf{r}_\beta\cdot\mathbf{j}_a)\mathbf{1}\right)\\ -N^*_{\mathrm{LME}_a}\sum_b N^*_{\mathrm{LME}_b}(1+\Delta_{ab})\mathbf{M}_b(\mathbf{x}-\mathbf{x}_b)\otimes\mathbf{M}_b(\mathbf{x}-\mathbf{x}_b)\end{aligned} \tag{5.22}$$

where

$$\mathbf{r}_\beta = 2\sum_a \beta_a N^*_{\mathrm{LME}_a}(\mathbf{x}-\mathbf{x}_a), \tag{5.23}$$

$$\mathbf{j}_a = (\mathbf{J}^*)^{-1}(\mathbf{x}-\mathbf{x}_a), \tag{5.24}$$

$$\Delta_{ab} = (\mathbf{x}-\mathbf{x}_b)\cdot(\mathbf{J}^*)^{-1}(\mathbf{x}-\mathbf{x}_a), \tag{5.25}$$

$$\mathbf{M}_a = 2\beta_a\mathbf{1} - (\mathbf{J}_\beta - \mathbf{1})(\mathbf{J}^*)^{-1} \tag{5.26}$$

while $\mathbf{1}$ indicates the identity matrix and

$$\mathbf{J}_\beta = 2\sum_a \beta_a N^*_{\mathrm{LME}_a}(\mathbf{x}-\mathbf{x}_a)\otimes(\mathbf{x}-\mathbf{x}_a). \tag{5.27}$$

5.3.3 Finite element-meshfree discretisation

The discretised governing equations are presented here. The weak form of Equation (5.3) reads:

$$\int_\Omega \nabla^s\delta\mathbf{u} : \boldsymbol{\sigma}\mathrm{d}\Omega - \int_{\Gamma_u}\delta\mathbf{u}\cdot\bar{\mathbf{t}}\mathrm{d}\Gamma = 0 \tag{5.28}$$

which must hold for all kinematically admissible variations $\delta\mathbf{u}$ and can be decomposed into the following weak forms, corresponding to the regular $\delta\hat{\mathbf{u}}$ and the enhanced $\delta\tilde{\mathbf{u}}$ displacement fields, respectively [44]:

$$\int_\Omega \nabla^{\mathrm{s}}\delta\hat{\mathbf{u}} : \boldsymbol{\sigma}\mathrm{d}\Omega = \int_{\Gamma_u}\delta\hat{\mathbf{u}}\cdot\bar{\mathbf{t}}\mathrm{d}\Gamma \tag{5.29a}$$

$$\int_\Omega \mathcal{H}_{\Gamma_d}(\nabla^{\mathrm{s}}\delta\tilde{\mathbf{u}}) : \boldsymbol{\sigma}\mathrm{d}\Omega + 2\int_{\Gamma_d}\delta\tilde{\mathbf{u}}\cdot\mathbf{t}_d\mathrm{d}\Gamma = \int_{\Gamma_u}\mathcal{H}_{\Gamma_d}\delta\tilde{\mathbf{u}}\cdot\bar{\mathbf{t}}\mathrm{d}\Gamma. \tag{5.29b}$$

Considering Equations 5.5 and 5.6, and the NURBS and LME approximations in Sections 5.3.1 and 5.3.2, the discretised formulations become:

$$\int_\Omega \mathbf{B}^{\mathrm{T}}_{\mathrm{IGA}}\,\boldsymbol{\sigma}\,\mathrm{d}\Omega = \int_{\Gamma_u}\mathbf{R}^{\mathrm{T}}\bar{\mathbf{t}}\,\mathrm{d}\Gamma, \tag{5.30a}$$

$$\int_\Omega \mathcal{H}_{\Gamma_d}\,\mathbf{B}_{\mathrm{LME}}^{\mathrm{T}}\,\boldsymbol{\sigma}\,\mathrm{d}\Omega + 2\int_{\Gamma_d}\mathbf{N}_{\mathrm{LME}}^{\mathrm{T}}\,\mathbf{t}_d\,\mathrm{d}\Gamma = \int_{\Gamma_u}\mathcal{H}_{\Gamma_d}\,\mathbf{N}_{\mathrm{LME}}^{\mathrm{T}}\,\bar{\mathbf{t}}\,\mathrm{d}\Gamma, \tag{5.30b}$$

where it is recalled that $\mathbf{R}$ and $\mathbf{N}_{\mathrm{LME}}$ are the NURBS and LME basis functions, respectively. The linearised set of equations then reads:

$$\begin{bmatrix} \mathbf{K}_{\mathrm{aa}} & \mathbf{K}_{\mathrm{ab}} \\ \mathbf{K}_{\mathrm{ab}} & \mathbf{K}_{\mathrm{bb}} \end{bmatrix} \begin{bmatrix} \Delta\mathbf{a} \\ \Delta\mathbf{b} \end{bmatrix} = \begin{bmatrix} \mathbf{f}_{\mathrm{a}}^{\mathrm{ext}} \\ \mathbf{f}_{\mathrm{b}}^{\mathrm{ext}} \end{bmatrix} - \begin{bmatrix} \mathbf{f}_{\mathrm{a}}^{\mathrm{int}} \\ \mathbf{f}_{\mathrm{b}}^{\mathrm{int}} \end{bmatrix} \tag{5.31}$$

with the arrays

$$\mathbf{f}_{\mathrm{a}}^{\mathrm{ext}} = \int_{\Gamma_{\mathrm{u}}}\mathbf{R}^{\mathrm{T}}\bar{\mathbf{t}}\,\mathrm{d}\Gamma \tag{5.32a}$$

$$\mathbf{f}_{\mathrm{b}}^{\mathrm{ext}} = \int_{\Gamma_{\mathrm{u}}}\mathcal{H}_{\Gamma_d}\mathbf{N}_{\mathrm{LME}}^{\mathrm{T}}\bar{\mathbf{t}}\,\mathrm{d}\Gamma \tag{5.32b}$$

$$\mathbf{f}_{\mathrm{a}}^{\mathrm{int}} = \int_\Omega \mathbf{B}_{\mathrm{IGA}}^{\mathrm{T}}\,\boldsymbol{\sigma}\,\mathrm{d}\Omega \tag{5.32c}$$

$$\mathbf{f}_{\mathrm{b}}^{\mathrm{int}} = \int_\Omega \mathcal{H}_{\Gamma_d}\mathbf{B}_{\mathrm{LME}}^{\mathrm{T}}\,\boldsymbol{\sigma}\,\mathrm{d}\Omega + 2\int_{\Gamma_d}\mathbf{N}_{\mathrm{LME}}^{\mathrm{T}}\mathbf{t}_d\,\mathrm{d}\Gamma \tag{5.32d}$$

and the stiffness matrices:

$$\mathbf{K}_{\mathrm{aa}} = \int_\Omega \mathbf{B}_{\mathrm{IGA}}^{\mathrm{T}}\mathbf{D}\mathbf{B}_{\mathrm{IGA}}\,\mathrm{d}\Omega \tag{5.33a}$$

$$\mathbf{K}_{\mathrm{ab}} = \int_\Omega \mathcal{H}_{\Gamma_d}\mathbf{B}_{\mathrm{IGA}}^{\mathrm{T}}\mathbf{D}\mathbf{B}_{\mathrm{LME}}\,\mathrm{d}\Omega \tag{5.33b}$$

$$\mathbf{K}_{\mathrm{ba}} = \int_\Omega \mathcal{H}_{\Gamma_d}\mathbf{B}_{\mathrm{LME}}^{\mathrm{T}}\mathbf{D}\mathbf{B}_{\mathrm{IGA}}\,\mathrm{d}\Omega \tag{5.33c}$$

$$\mathbf{K}_{\mathrm{bb}} = \int_\Omega \mathbf{B}_{\mathrm{LME}}^{\mathrm{T}}\mathbf{D}\mathbf{B}_{\mathrm{LME}}\,\mathrm{d}\Omega + 4\int_{\Gamma_d}\mathbf{N}_{\mathrm{LME}}^{\mathrm{T}}\mathbf{Q}^{\mathrm{T}}\mathbf{T}_d\mathbf{Q}\mathbf{N}_{\mathrm{LME}}\,\mathrm{d}\Gamma. \tag{5.33d}$$

Herein, $\mathbf{Q}$ is the rotation matrix and $\mathbf{T}_d = \partial\mathbf{t}_d/\partial[\![\mathbf{u}]\!]$ is the linearised tangent stiffness of the traction-relative displacement relation. It is noted that, based on the Heaviside sign function, the displacement jump becomes $[\![\mathbf{u}]\!] = 2\sum_{l=1}^{n_{\mathrm{enr}}} N_{\mathrm{LME}_l}(\mathbf{x})\,b_l$ [44], where n_{enr} is the number of enriched points.

5.4 Implementation Aspects

The extensive overlap in the supports of meshfree clouds impedes a straightforward enrichment of individual points during crack propagation. Also, employing an extended approach necessitates compatibility enforcement to localise the effect of the Heaviside function into a narrow region in the vicinity of the discontinuity (ideally removing the effect of the second function at the location of the control points). With overlapping basis functions, however, a

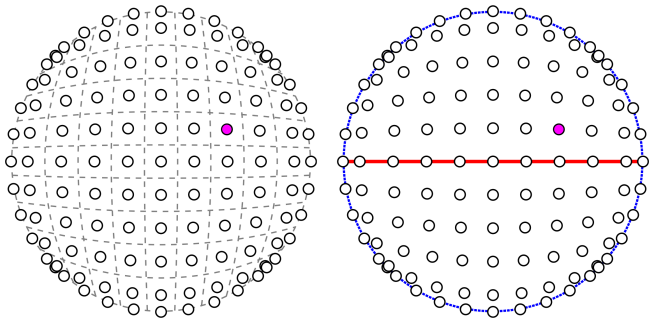

Figure 5.4: Disk with a unit radius. A quadratic IGA discretisation is chosen for the standard part (left), while the same node-set of control points is utilised for the LME approach in the enhanced part (right). The crack is indicated by the red solid line. The magenta marker shows the location of the point for which the basis functions and the corresponding gradients have been plotted in Figure 5.5.

complete removal is impossible. Therefore, compatibility enforcement narrows it down to a small region around the crack, reducing the error to a sufficiently small region [44]. Otherwise, all points within the enhanced field will be involved, increasing the computation error and a possible loss of optimal convergence [46].

5.4.1 Enhancement of individual control points and the integration scheme

Within IGA the inter-element sharing of control points complicates the enrichment scheme [44]. Unlike IGA, however, the absence of the notion of an element within a meshless approach facilitates a more global definition of enrichment: points behind the crack tip whose supports intersect the crack path will be enriched. As illustration, the enrichment scheme for a uniform node-set is shown in Figures 5.2 and 5.3. Points within the zone between l-distanced offsets from the crack path (see Figure 5.2) and before the crack tip (see Figure 5.3) are enriched, where $l = \sqrt{-\ln(\mathrm{TOL}_0)/\gamma}h$ and TOL_0 is the tolerance for vanishing the support of the LME basis function. The length l can be considered as a function of nodal spacing h_{node} and a scalar Λ, $l = \Lambda h_{\mathrm{node}}$ (see Table 5.1). For smaller values of γ the support of the basis function becomes bigger, and consequently, the distribution of the basis becomes smoother [108]. For instance, $\gamma = 0.1$ returns a radius which approximately equals 9 times the nodal spacing h_{node} (considering a uniform node-set).

Integration cells have been utilised within the LME approach [108]. Herein, the same IGA discretisation is used as the integration cells which is equipped with subtriangulation for cracked elements. Integration points are defined using a standard Gaussian quadrature rule.

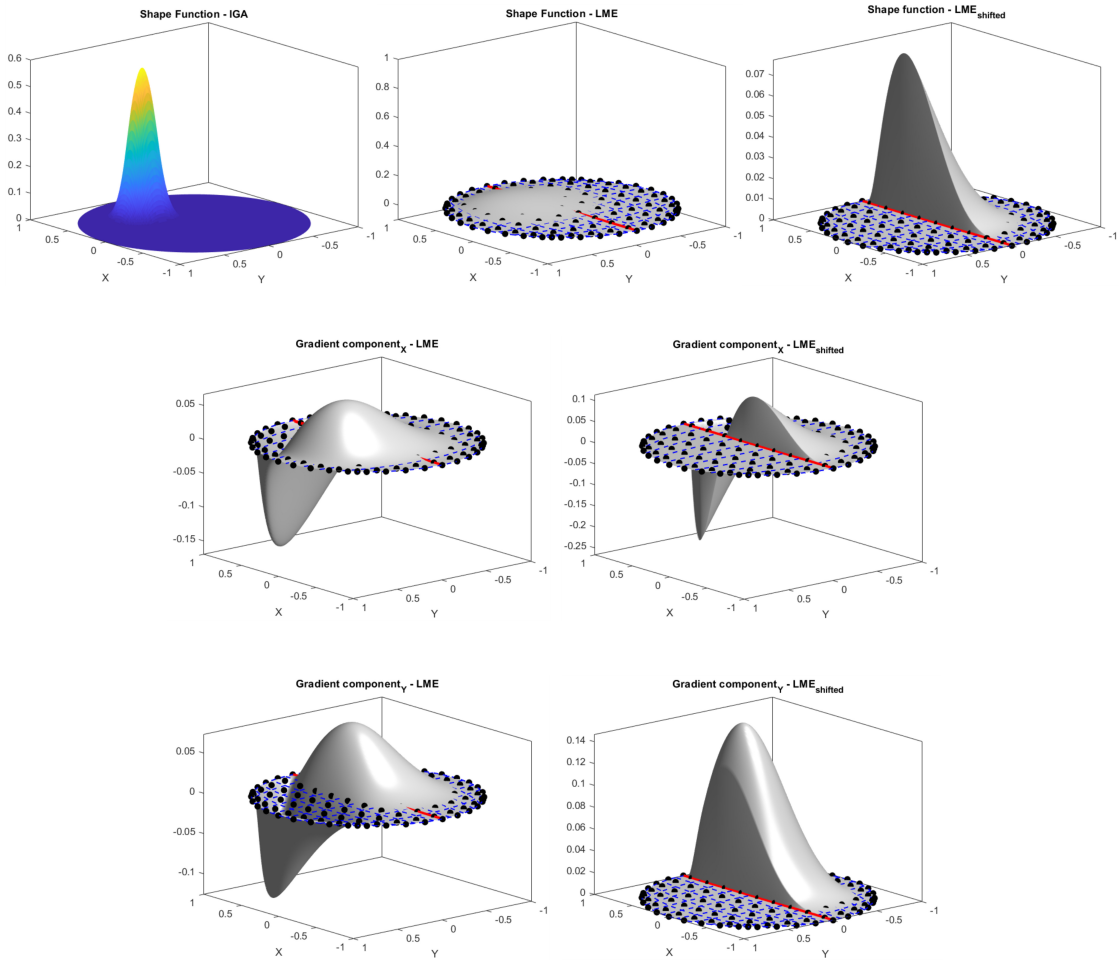

Figure 5.5: Shifting technique for the disk example with $\gamma = 0.1$. The top row at left represents the IGA basis function (coloured plot) for the standard section, while the LME values before and after shifting technique are shown in the middle and at the right, respectively. The gradients in the $\mathcal{X}$ and $\mathcal{Y}$-directions are given in the middle and the bottom rows before (left) and after (right) shifting.

5.4.2 Compatibility enforcement for LME

The shifting technique is adopted here as a means to enforce compatibility, Figure 5.2. This is new as shifting has not been used for a meshless approach within the extended framework. Furthermore, the blending technique with a Heaviside step function is exploited, an approach which effectively removes the discontinuous field in front of the crack tip [44], see the dashed red circle in Figure 5.3. This approach is robust, efficient and simple within the X-IGALME framework, definitely when compared to techniques to model cracks within a meshfree approach, such as the visibility or transparency criteria [98].

Employing shifting and blending, as well as Equations (5.7) and (5.11), the displacement

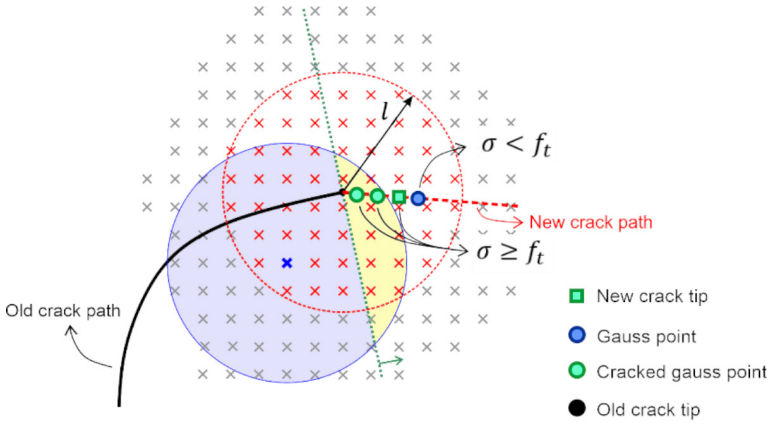

Figure 5.6: Crack extension determined with the nonlocal technique. The nonlocal approach involves the support of all points within the support of the old crack tip, i.e. all red crosses. As an example, the support of the blue cross is divided into two sections: the yellow part which denotes the intact material, i.e. where the Heaviside removes the effect of the discontinuity, and the purple part which indicates the area where both the standard and the enhanced fields exist.

Table 5.1: Radius of Gaussian decay of the basis function. The tolerance is set $\mathrm{TOL}_0 = 10^{-8}$ for vanishing the support of the LME basis function.

γ	0.1	0.5	0.8	1	1.5	2
Λ	8.94	4	3.16	2.82	2.31	2

field of Equation (5.5) becomes:

$$\mathbf{u}(\mathbf{x}) = \sum_{\mathcal{I}\in\mathcal{N}} \mathbf{R}_{\mathcal{I}}(\mathbf{x})\mathbf{a}_{\mathcal{I}} + \sum_{\mathcal{I}^{\mathcal{H}}\in\mathcal{N}^{\mathcal{H}}} \mathcal{H}^{Bl}_{\Gamma_d}(\mathbf{x}) \left(\mathcal{H}^{GP}_{\Gamma_d}(\mathbf{x}) - \mathcal{H}^{\mathcal{I}^{\mathcal{H}}}_{\Gamma_d}\right) \mathbf{N}_{\mathrm{LME}_{\mathcal{I}^{\mathcal{H}}}}(\mathbf{x})\mathbf{b}_{\mathcal{I}^{\mathcal{H}}} \tag{5.34}$$

with $\mathcal{N}^{\mathcal{H}} \subset \mathcal{N}$ the subset enriched by the Heaviside function, while $\mathcal{H}^{\mathcal{I}^{\mathcal{H}}}_{\Gamma_d}$ and $\mathcal{H}^{GP}_{\Gamma_d}$ are the values of the Heaviside function at the control point $\mathcal{I}^{\mathcal{H}}$ and the Gauss point under consideration defined by the sign function. $\mathcal{H}^{Bl}_{\Gamma_d}$ is the Heaviside function defined at the Gauss point with respect to the crack tip [44]. According to Equation (5.34) discretised equations are equipped with shifting and blending techniques at the discontinuity.

To demonstrate the effect of shifting, the basis function of an arbitrary point is illustrated for a disk, see Figure 5.4. Note that IGA accurately captures the curvature of the disk, and LME improves the accuracy of the enriched part. Figure 5.5 illustrates the effect of shifting on the basis functions in the first row. Shifted values of the gradients in the $\mathcal{X}$ and $\mathcal{Y}$-directions are compared with crude basis functions in the second and the third rows, respectively. Noteworthy is the fact that lower values for γ might help in enforcing the compatibility between the standard and the enhanced sections, i.e. in reducing the effect of the enhanced

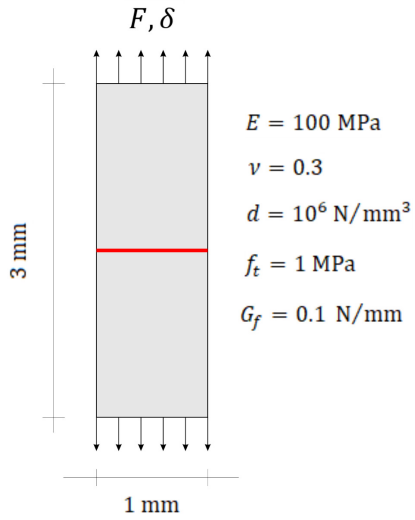

Figure 5.7: Geometry and material properties of a cracked plate (the crack is represented by the red solid line) subjected to simple tension. A dummy stiffness d is adopted to keep the interface element closed before the fracture criterion is met. F and δ denote the force and the displacement, respectively.

term at the location of control points.

5.4.3 Direction of crack extension

The higher-order continuity provided by IGA removes the stress jumps at element boundaries observed in the standard finite element analysis. Meshless techniques can provide an even higher accuracy, leading to a further improved estimate of the stresses around the crack tip. To determine the crack propagation direction, however, a more global estimate for stresses is required [44]. Thus, utilising a nonlocal like approach, an average of the stresses around the crack tip is used, thus estimating the crack propagation direction from averaged stress values, see Figure 5.6. Afterwards, the averaged local stress in front of the crack tip is compared with the fracture strength in the fracture criterion. The Gaussian distribution function [27, 44] is utilised for the averaging. The same support width of the LME basis function is exploited as length scale, since it is normally larger than the length scale normally used in element-based approaches (2-3 times the length of the typical element [144]).

5.4.4 Complementary features IGA and LME

IGA and LME possess complementary features, allowing to mitigate the deficiencies of the other approach:

- The capability of IGA to model the geometry exactly mitigates the difficulty of LME to achieve sufficient accuracy at the boundary. On the other hand, LME improves the

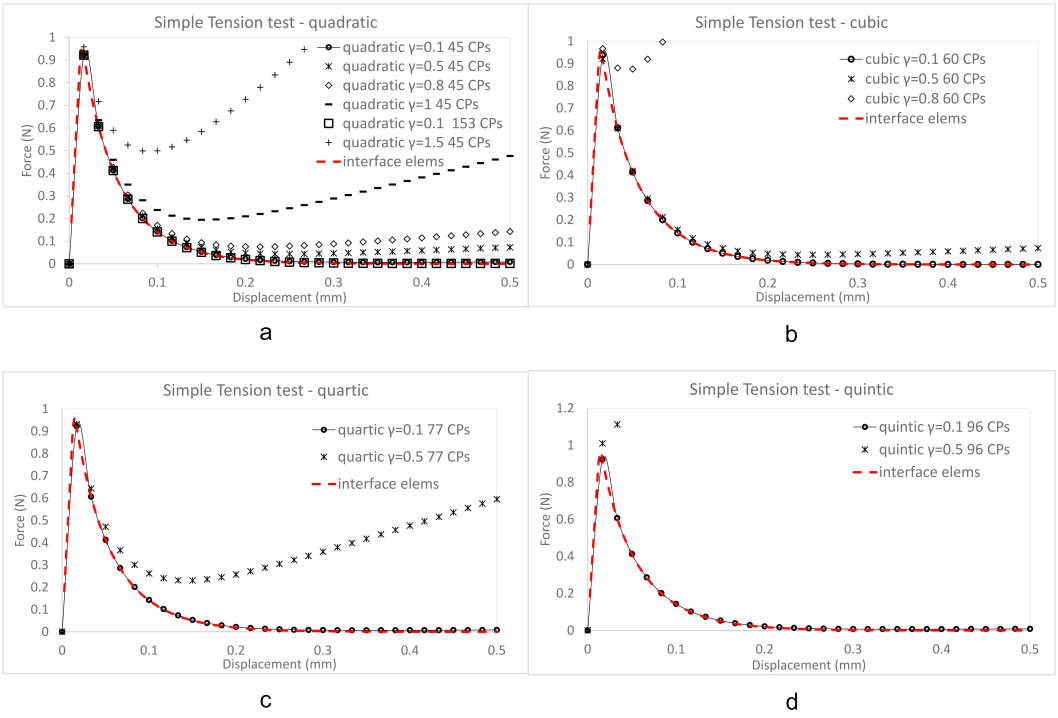

Figure 5.8: Load-displacement curve for the simple tension test. "CPs" denotes control points. "quartic", "cubic" and "quintic" denote the order of the NURBS.

accuracy in the interior.

- When dealing with arbitrary crack paths, a disproportionate split of elements is inevitable in element-based extended approaches, which can lead to singularities [44, 146]. Since a meshfree approach has been adopted for the enhanced part here, this issue is now eliminated. Therefore, any remeshing or node repositioning is unnecessary.

- Unlike XIGA [44] where two crack tips must be utilised – one for the enrichment scheme and another for the real location of the crack tip – just a single crack tip is now required. Accordingly, a simpler enrichment scheme can be adopted compared to the element-wise enrichment of XIGA.

- In contrast to XIGA, where different orders for the standard and extended parts are incompatible [39, 44], LME and IGA can always be combined within X-IGALME, provided that the right combination of the node-set and the dimensionless aspect ratio γ have been chosen. Moreover, a super-quadratic convergence rate can then be obtained.

5.5 Numerical Examples and Discussion

Now, the efficacy of the method is investigated at hand of some numerical examples.

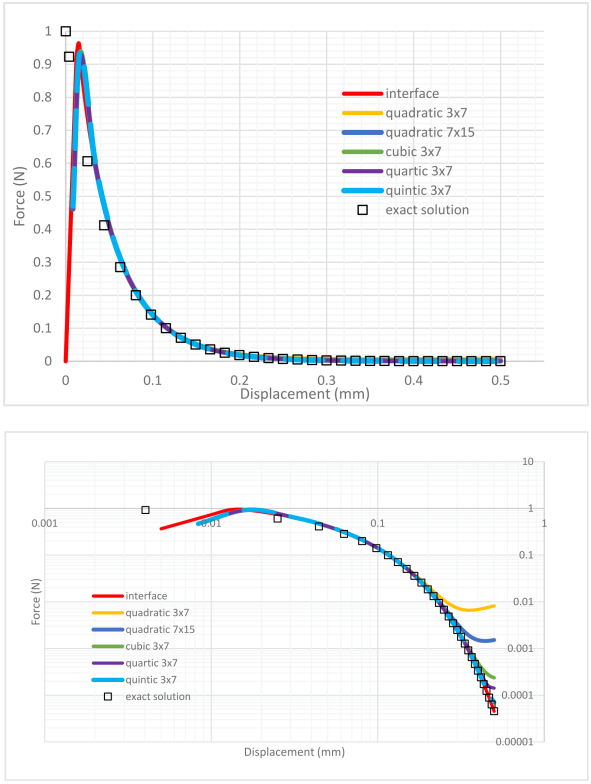

Figure 5.9: Force-displacement curves for $\gamma = 0.1$ are plotted for different NURBS orders, see the top. The logarithmic scale for both axes are plotted at the bottom. The numbers denote the number of elements in the $\mathcal{X}$ and $\mathcal{Y}$-directions respectively.

5.5.1 Continuity order: simple tension test

In the first example the effect of different node-sets and the dimensionless aspect ratio γ are assessed. The results are compared with a solution obtained using standard interface elements, where a dummy stiffness has been utilised to constrain the interface until the fracture criterion has been met. The geometry and the material properties are shown in Figure 5.7.

The results in Figure 5.8 indicate convergence for lower values of the dimensionless aspect ratio γ. This is shown for different NURBS orders for the standard part, leading to different node-sets for the enhanced part. It is noted that the same number of elements have been employed in the simulations to enable a proper comparison. For this case $\gamma = 0.1$ renders the best result for all NURBS orders.

To represent the differences between the NURBS orders utilised in this example, a log-log scale figure is plotted for the force-displacement curve resulted by $\gamma = 0.1$. A better performance in the form of a convergence trend is observed with the increase of the NURBS continuity-order (see Figure 5.9). Next is the effect of mesh refinement which is respectively

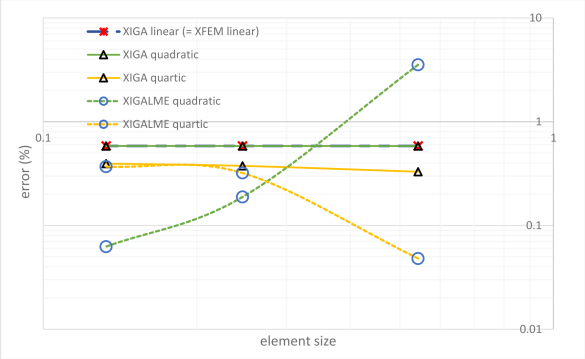

Figure 5.10: Relative error for the mesh refinement.

compared with XIGA of the same order and linear XFEM, see Figure 5.10. The relative error is computed on the integral below the force-displacement curve $\int_0^\infty F \cdot \delta \, \mathrm{d}\delta$, i.e. the error calculated on the dissipated energy. Results show a better performance of X-IGALME compared to XIGA and XFEM, except for the coarsest mesh of the quadratic order. Error patterns for X-IGALME, however, are not similar to each other or to XIGA, which is believed to be due to the meshfree characteristic of the extended part.

5.5.2 Sensitivity analysis of singularity: simple tension test

A sensitivity analysis has been adopted to check the singularity of X-IGALME's stiffness matrix. This is important in the sense that element-wise approaches are known for this characteristic when the crack approaches one of the edges of the cracked element [146]. Therefore, a special enrichment is needed when the crack path coincides with the element edge in such approaches. The geometry is illustrated in Figure 5.11 which is similar to Section 5.5.1 with different enrichment cases when the crack coincides with the edge.

The results are presented in Figure 5.12. X-IGALME renders a stable trend even when the crack coincides with the edge. On the contrary, the other approaches return very high condition numbers for the stiffness matrices which implies an instability of the solution. The condition number for X-IGALME becomes even more stable when less control points are enriched, e.g. where the enrichment meets XIGA enrichment. This shows the stability of the solution. Nevertheless, the stability of X-IGALME provides a single prescription of the enrichment (see Figures 5.13a and 5.13c), while a special enrichment for element-wise approaches is needed where the crack coincides with the edge of the cracked element (see Figure 5.13.b), otherwise singularity results.

To assess the accuracy of the solution by the condition numbers reported in Figure 5.12, the area below the force displacement curve is calculated for quartic order and is compared to quartic XIGA, see Figure 5.14. Generally, errors are below 1%. X-IGALME with the

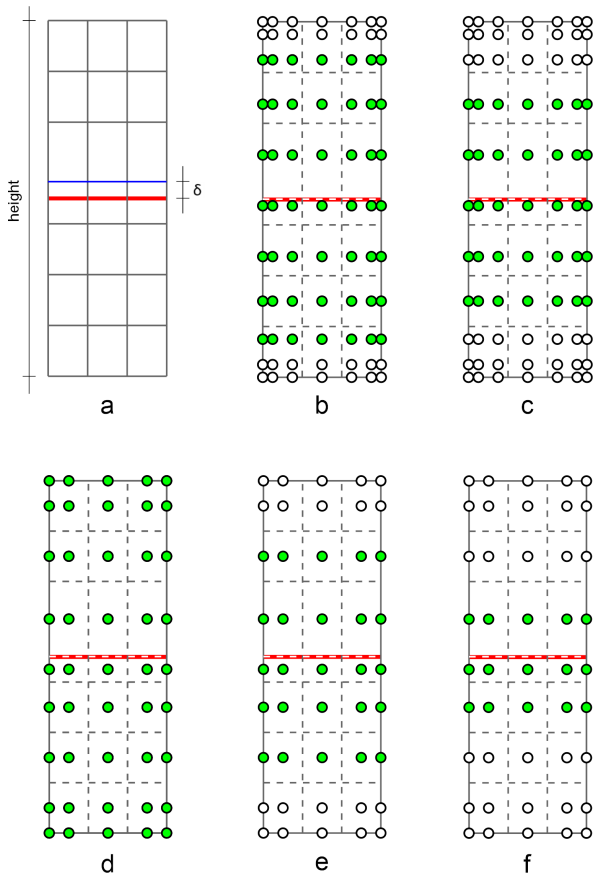

Figure 5.11: Sensitivity analysis for the singularity of X-IGALME. (a) defines the distance of the crack from the specified edge (the blue edge). Different cases of enrichment are shown for the coincidence of the crack and the specified edge: (b) and (c) are the normal and XIGA-like enrichment for X-IGALME in quartic order; (d), (e) and (f) denote the normal, the other enrichment and the XIGA-like enrichment for X-IGALME in quadratic order. X-IGALME is compared to XIGA and XFEM for different continuity-orders of NURBS.

XIGA-like enrichment shows the best performance at the smallest distances of the crack from the edge. This deteriorates further away (bigger distances between the crack and the edge), where the normal enrichment of X-IGALME is superior. Noteworthy is the fact that XIGA and XIGA-like enrichment for X-IGALME render close results.

5.5.3 Aspect ratio effect on energy dissipation: Three Point Bending test

The effect of the dimensionless aspect ratio γ on the energy dissipation have been investigated for a Three Point Bending (TPB) test. The geometry and the material properties are shown in Figure 5.15. As noted before, the shear stiffness has been set equal to zero in order to obtain a symmetric stiffness matrix. To investigate whether the energy dissipation is

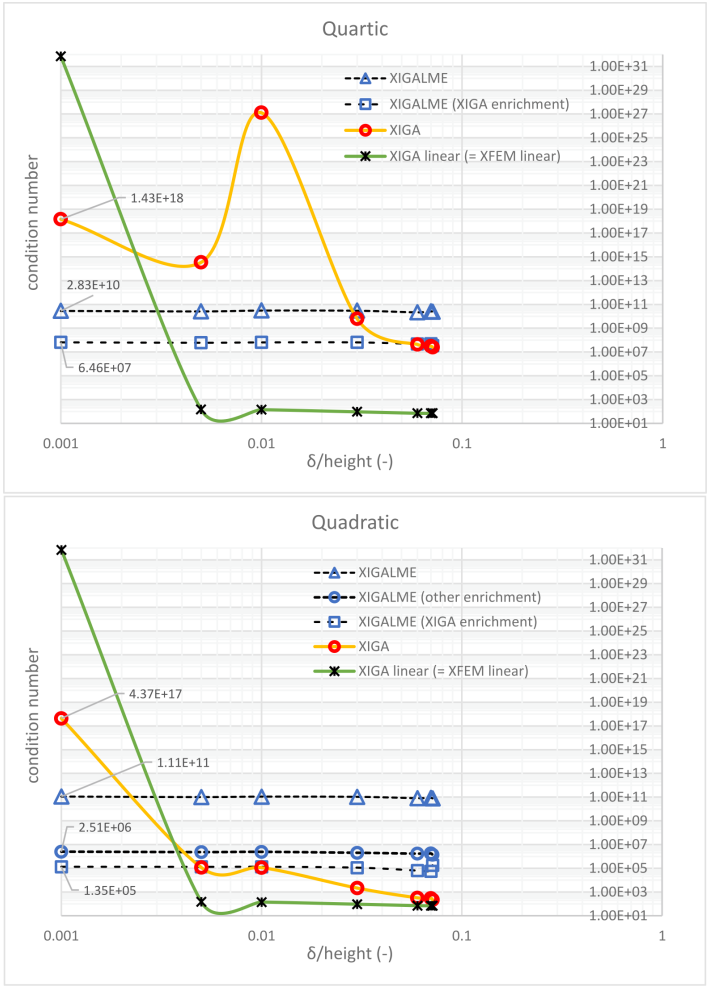

Figure 5.12: Condition number comparison of X-IGALME with XIGA and linear XFEM.

independent of the spatial discretisation, the dissipated energy is compared with the fracture energy, 0.3 Nmm. From the results in Table 5.2 we conclude that lower γ values lead to a convergence towards the case of $\gamma = 0.3$, see Figure 5.16. In addition, the dissipated energy for $\gamma = 0.3$ is closer to the fracture energy, supporting the conclusion made in Section 5.5.1, namely that lower values for γ yield better results. From the perspective of the NURBS order, the results for the quadratic discretisation are acceptable only when $\gamma = 0.3$. For a quartic NURBS, however, all γ values yield satisfactory results, although the trend holds that better results are obtained for lower values of γ. To study the effect of the spatial discretisation, a coarse quartic NURBS mesh has been examined with $\gamma = 0.3$. The results for the coarse and fine meshes appear to coincide.

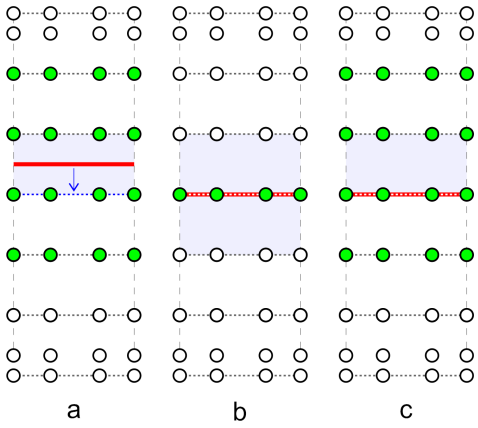

Figure 5.13: Enrichment prescriptions for X-IGALME and other element-wise extended approaches. A cubic order has been adopted for discretisation and the shade indicates the cracked element/elements. (a) indicates the crack inside the element whose enrichment is the same for X-IGALME and other approaches. Locating the crack on the blue edge necessitates a special enrichment shown in (b) for element-wise extended approaches. For X-IGALME, however, the same enrichment as (a) can be preserved, c.f. (c).

Table 5.2: Integration of load-displacement curves (dissipated energy).

Case	Qd[†]-0.3-1062[‡]	Qd-0.5-1062	Qd-0.8-1062	
Area(Nmm)	0.3212	0.4172	0.5803	
Case	Qr-0.3-1062	Qr-0.5-1062	Qr-0.8-1062	Qr-0.3-702
Area(Nmm)	0.2959	0.3120	0.3296	0.3079

[†] Qd: quadratic NURBS; Qr: quartic NURBS.
[‡] The order follows *type-γ-elems*; e.g. Qd-0.5-1062 denotes quadratic - $\gamma = 0.5$ - 1062 elements.

5.5.4 Straight crack propagation: peeling test

A Double Cantilever Beam (DCB), shown in Figure 5.17, is now investigated. Different from the TPB test, the significance of this example lies in the propagation which takes place perpendicular to the smaller edge of the beam, where the node-set plays a crucial role for the enhanced part. The material properties are as follows: The Young's modulus, Poisson's ratio, the tensile strength and the fracture energy are $E = 100$ MPa, $\nu = 0.3$, $f_t = 1$ MPa and $G_f = 0.1$ Nmm^{-1}, respectively. For the interface elements, which serve as the benchmark, the dummy stiffness $d = 10^6$ Nmm^{-3} to prevent negative openings. The results are also compared with findings from XIGA [44].

As expected, the results are unstable or divergent for coarse meshes in the vertical direction. While maintaining the same mesh in the horizontal direction, a mesh refinement in the vertical direction leads to a failure of the line-search technique to compute the LME basis

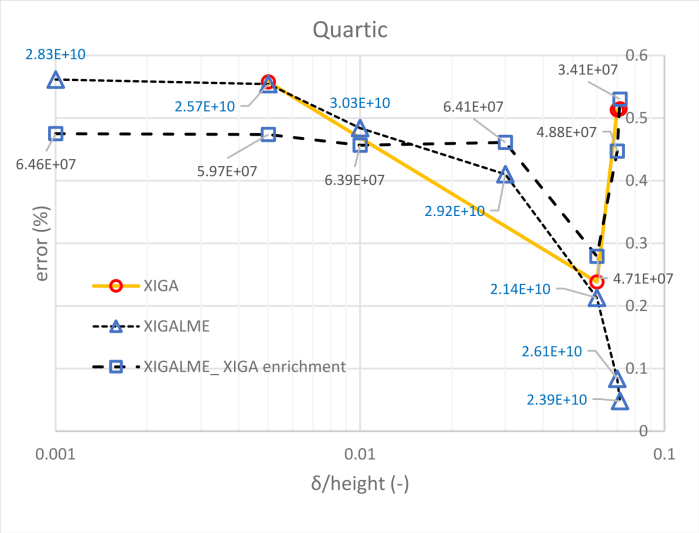

Figure 5.14: Error estimation of the singularity analysis (see Figure 5.12) for quartic order. The digits correspond to the condition number of each case. XIGA is only reported for stable cases. δ denotes the distance of the crack from the specified edge.

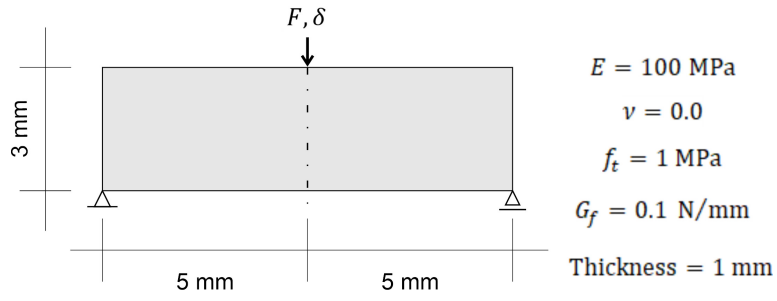

Figure 5.15: Geometry and material properties of Three Point Bending test.

function [128, 6]. Hence, a uniform nodal spacing is used, which facilitates LME procedure and improves the crack propagation. This leads to a finer mesh compared to XIGA [44], see the blue triangles in Figure 5.18a.

The values for γ are problem-dependent (node-set-specific). It can be improved by optimising the value for γ at each point. This optimisation problem can be solved by adopting a variational approach which considers the physical field as well as the locality of the basis functions [109].

For cohesive fracture, the moment of crack propagation is central in obtaining a smooth mechanical response. Although cohesive fracture is energy-based, i.e. it compensates a belated fracture initiation in forthcoming loading steps, a jagged response can be inevitable. The results presented here are obtained for a stress-based fracture criterion, i.e. $\sigma_y^{\text{loc}} \geq f_t$. To investigate the effect of the fracture criterion on the jagged response of Figure 5.18a (blue

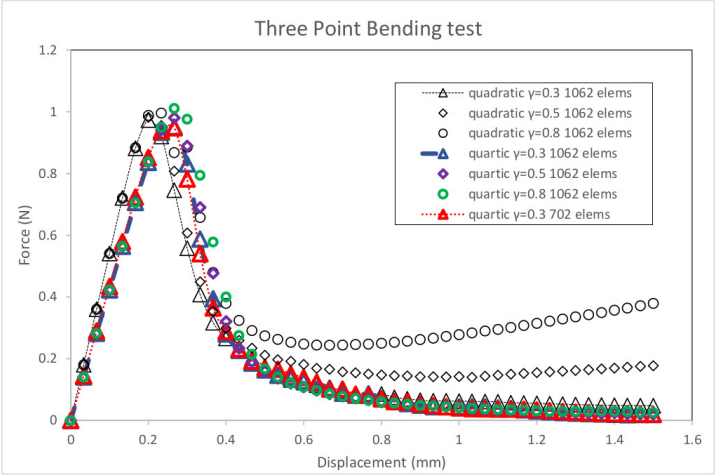

Figure 5.16: Load-displacement curves for the Three Point Bending test using different γ-values. Quadratic and quartic denote the order of the NURBS.

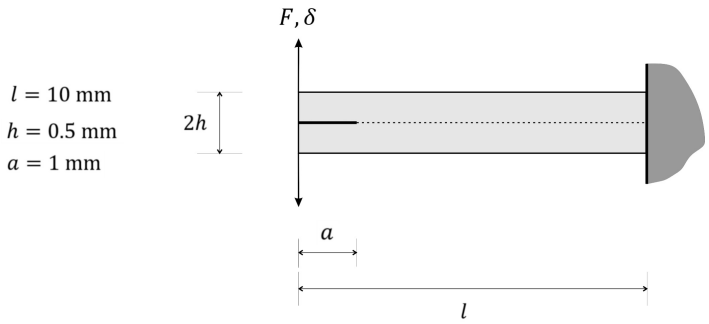

Figure 5.17: Double Cantilever Beam with an initial notch subjected to mode-I loading.

triangles), we have adopted the additional criterion of a positive displacement jump, similar to the criterion used in interface elements. However, while the degrees of freedom are uniquely defined for an interface element and a dummy stiffness guarantees the non-negativity of the displacement jump, this requires more effort for an extended method, since a fictitious crack propagation with new degrees of freedom must be defined. Afterwards, a new nested solution is necessary for the new, temporary configuration to compute the displacement jumps. The extension will become permanent upon satisfaction of the displacement fracture criterion. Otherwise, the previous configuration of crack is used. The same number of elements and the same NURBS order are used (similar to the blue triangles in Figure 5.18a). This results in Figure 5.18b, where there is less noise (lower amplitude) for the present approach. The results are also compared with those from XIGA. X-IGALME's best results are compared

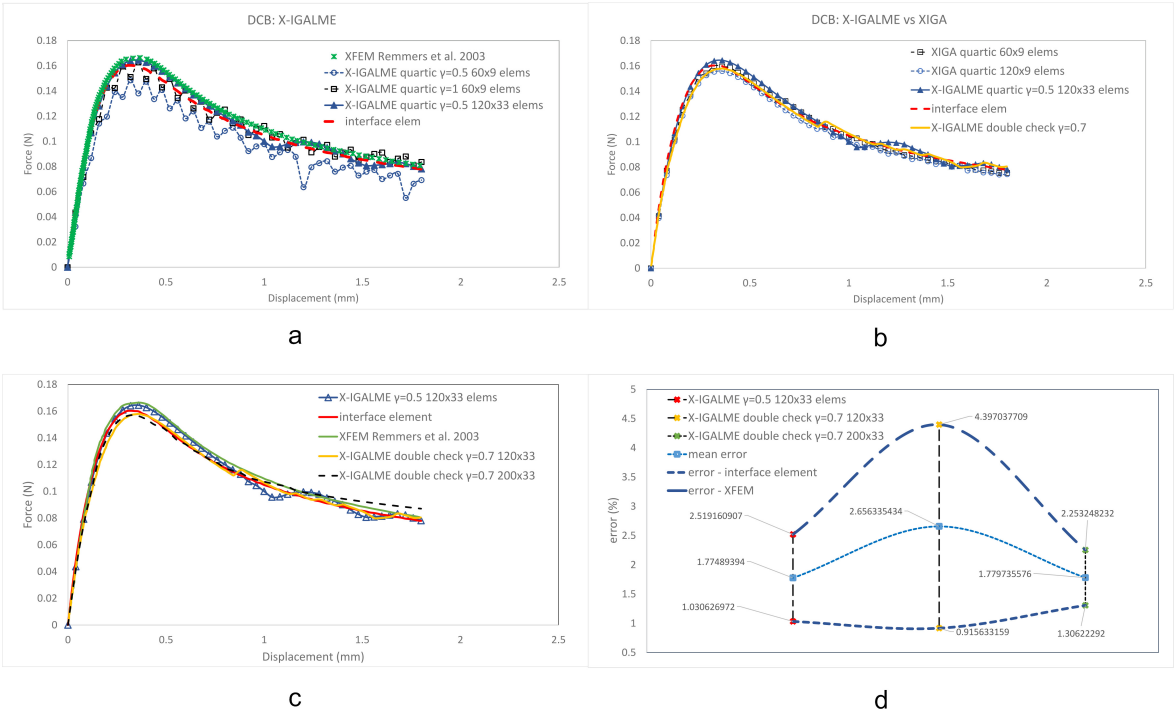

Figure 5.18: Load-displacement curve for the Double Cantilever Beam. The results are compared with interface elements and XFEM [103] in (a) and (c), while a comparison between X-IGALME and XIGA has been made in (b). The numbers in the legend denote the number of elements in the $\mathcal{X}$ and in the $\mathcal{Y}$-directions, respectively. The best results of X-IGALME are compared with Interface element and XFEM in (c). The relative error (integral under the curve) is plotted for X-IGALME results benchmarked against interface element and XFEM approaches in (d).

with interface element and XFEM approaches, in Figure 5.18c. A further refinement is utilised to obtain the smoothest solution, see the dashed black line in Figure 5.18c. The corresponding relative errors (based on the integral below the force-displacement curves) are plotted in Figure 5.18d. The smallest error is observed for the interface element showing closer response of X-IGALME to this approach, while the mean error (mean of the interface element and XFEM errors) is around two percent. The peak values of X-IGALME are also closer to the interface element approach, except for the $\gamma = 0.5$ which is closer to XFEM.

5.5.5 Arbitrary crack propagation: TPB test with eccentric crack

Free crack propagation is now examined within a TPB test similar to that in Section 5.5.3. The key difference is that now the crack is forced to initiate 0.7 millimeters away from the centreline (see Figure 5.19). Therefore, an eccentric propagation is promoted where a curved crack profile results. The material properties are given in Figure 5.19, and $\gamma = 0.3$ for

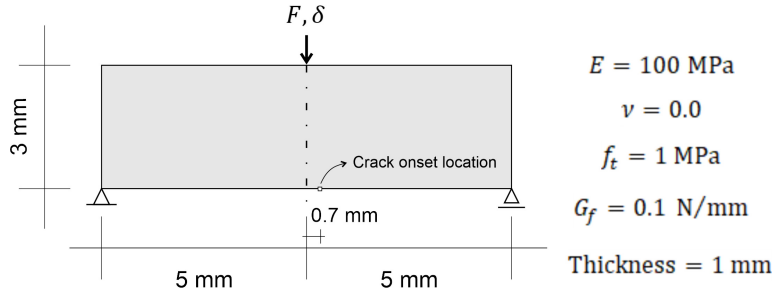

Figure 5.19: Three-Point Bending test with an eccentric crack.

the quadratic and the quartic discretisations in conformity with the results of Section 5.5.3. Figure 5.20 gives the crack paths, which are compared with that which results from XFEM [8]. The results almost coincide.

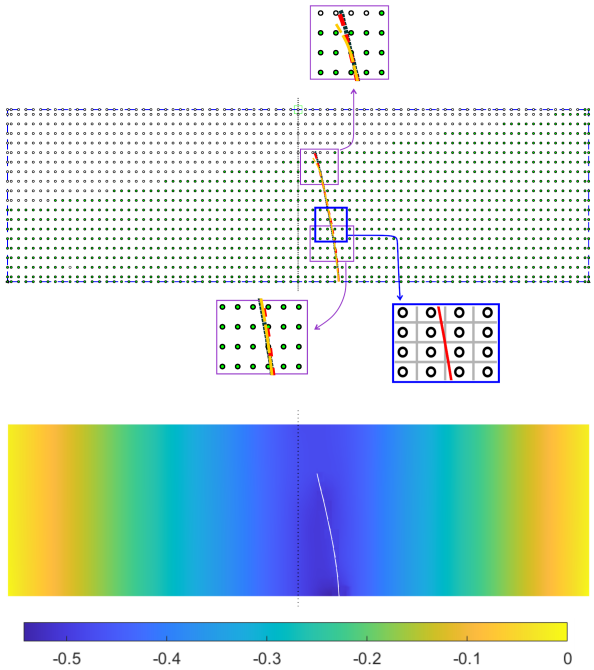

Figure 5.20: Crack profiles for the quadratic (solid red line) and the quartic NURBS (dashed yellow line). These results are compared with XFEM [8] (dotted black line). The displacement contour in the $\mathcal{Y}$-direction is given for the quadratic discretisation. The values of the colour bar are given in millimeters.

5.5.6 Exact parametrisation of a curved geometry: circular plate with multiple holes

A circular plate with a slit in the centre is subjected to prescribed displacements at the boundary to evaluate X-IGALME in an exact parametrisation of a curved geometry. The

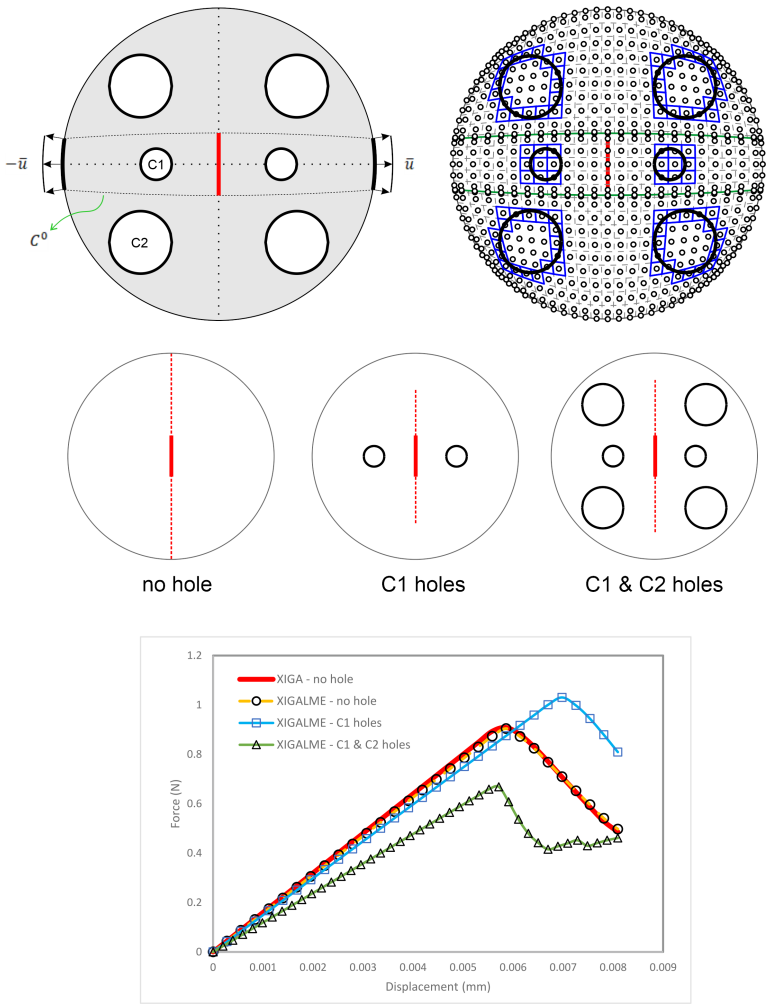

Figure 5.21: A disk with an initial slit and multiple holes is presented. Crack propagation is investigated for three cases: no hole; C1 holes; C1 and C2 holes. Force-displacement curves are also plotted for the three cases and are compared to XIGA for the no hole case.

performance in the presence of multiple holes is also investigated by 6 holes comprised of 2 different sizes. Geometry and discretisation/node-set are presented in Figure 5.21. The crack length is 0.4 mm and the radii for the disk, C1 and C2 holes are 1, 0.1 and 0.2 millimeters, respectively. Void level set has been adopted for modelling the holes, where unlike element-wise extended approaches, no special care has to be exercised in enrichment [44] due to the singularity-free characteristic of the X-IGALME. The material properties are given as: $E = 100$ MPa; $\nu = 0$; $G_f = 0.1$ N/mm; $\gamma = 1$ and $f_t = 1$ MPa. The slit and the fracturing are set traction-free.

The solution is first benchmarked against XIGA without any hole for the full propagation of the crack through the entire disk. In a second analysis only C1 holes are considered where

the stiffness is lower than the first case (the blue line with rectangles is below the yellow/red line). The location of C1 holes delays the propagation of the initial slit. Adding C2 holes to the problem significantly reduces the stiffness (the green line with triangles is blow the others). A softening phenomenon happens once again upon crack propagation until it reaches the C2 holes. Afterwards, a delay in propagation of the crack (due to the presence of C2 holes) renders a hardening behavior followed by alternate softening responses.

5.6 Concluding Remarks

Isogeometic analysis has been augmented with local maximum entropy in an extended framework, which has been coined X-IGALME. The high accuracy of isogeometric analysis in capturing complex boundaries together with the high accuracy of the local maximum entropy approach in the interior renders the method an excellent alternative within the class of extended discretisation methods. The higher continuity-order provided by both IGA and LME leads to an improved estimate of stresses which is central in finding the correct crack extension direction. Moreover, it sets the scene for higher-order differential equations.

The approach has been assessed for different NURBS orders, node-sets and values of the aspect ratio γ. It is proven that the choice for γ is node-set specific. Nevertheless, despite failing to return the conventional error pattern for mesh refinement, the errors show a better performance for X-IGALME in almost all cases. It has been observed that lower values for γ return correct results. This is in line with the hypothesis that the lower values of γ help in compatibility enforcement. The effect of γ on the energy dissipation has been investigated as well, supporting the conclusion about the lower values of γ. An optimisation problem on how to choose the value of γ for a given node-set is a potential topic for a future research. The role of different quadrature rules on the solution is another topic to explore.

A detailed sensitivity analysis of singularity has been performed on X-IGALME. The results indicate a guaranteed stability of the solution for X-IGALME, where XIGA and XFEM fail. Unlike element-wise approaches, the singularity-free characteristic of X-IGALME facilitates a single prescription for enrichment in any condition, including void level set. Finally, straight and curved fractures as well as voids have been simulated successfully for straight and curved geometries. Indeed, X-IGALME possesses some excellent features as a result from combining of an isogeometric finite element scheme and a meshless technique.

Chapter 6

XIGA for Fluid-Saturated Porous Media

An extended isogeometric analysis (XIGA) approach is proposed for modelling fracturing in a fluid-saturated porous material[1]. XIGA provides a definition of the discontinuity independent of the underlying mesh layout, which obviates the need of knowing the crack extension direction a priori. Unlike Lagrange shape functions used in the standard finite element approach, Non-Uniform Rational B-Splines (NURBS) provide a higher-order interelement continuity which leads to a continuous fluid flow also at element boundaries, thereby satisfying the local mass balance. It also leads to an improved estimate of the crack path due to a smoother stress distribution. The NURBS basis functions are cast in finite element data structure using Bézier extraction. To model the discontinuity, the Heaviside sign function is utilised within the displacement and the pressure fields, complemented by the shifting and the blending techniques to enforce compatibility perpendicular and parallel to the crack path, respectively. Different aspects of the approach are assessed through examples comprising straight and curved crack paths for stationary and propagating discontinuities.

6.1 Research Background

Fluid flow in a deforming porous medium is a topic of major attention due to its numerous applications in, for instance, petroleum and geotechnical engineering [139, 78], biology and medical sciences [85, 97, 137], and three or four-phase media [125, 67, 136]. Initially, the theory was limited to intact porous materials [132, 18, 31, 84]. Analytical solutions which

[1]This chapter is directly adopted from:

Fathi, F., Chen, L. , Hageman, T. and de Borst, R., 2021. Extended isogeometric analysis of a progressively fracturing fluid-saturated porous medium. Submitted to International Journal for Numerical Methods in Engineering

include fractures are available [99, 52, 96], but are subject to simplifying assumptions such as linear elasticity, homogeneity and impermeability, as well as idealised geometries. One of the earliest numerical models which considered a discontinuity, including fluid flow in the surrounding porous medium was proposed by Boone and Ingraffea [21], exploiting a combination of finite element and finite difference methods.

The advent of interface elements paved the way for modelling discontinuities embedded in an otherwise continuous medium. They have become popular owing to their simple implementation and robust computational performance [114, 120, 121, 72, 140]. A disadvantage of interface elements is that they require an a priori knowledge of the crack extension direction. Remeshing was introduced as the remedy for the arbitrary crack propagation [28, 29, 27], also in saturated porous media [116, 118].

A more elegant approach to arbitrary crack paths is the extended finite element method (XFEM), where the crack path is decoupled from the underlying mesh layout. It was first developed for linear elastic fracture mechanics (LEFM) [15, 17] and subsequently developed for cohesive fracture [144, 90, 103]. Different aspects of XFEM within saturated/unsaturated porous media have been studied [37, 104, 106], including shear banding [105] and large deformation [70]. Moreover, the implications of assuming a continuous or a discontinuous pressure across the discontinuity have been assessed [47].

In (un)saturated porous media standard finite element analysis typically does not locally conserve mass owing to the $\mathcal{C}^0$-continuity at element boundaries. Lagrange basis functions lead to a discontinuous interelement pressure gradient and therefore to a loss of local mass balance, unless special degrees of freedom are used [86]. Meshfree methods have been exploited to resolve this issue as they provide a higher order of continuity, and consequently, a smoother stress field and pressure gradient [102, 56, 55]. Nevertheless, a higher computational cost compared to finite element methods and the poor geometric parametrisation of the complex boundaries are disadvantages of meshfree approaches, which have limited their use.

A more promising alternative to provide higher-order continuity is isogeometric analysis (IGA), originally proposed to connect the design and the analysis tools in order to obtain the highest possible precision in geometric parametrisation and to reduce the computational cost through bypassing the mesh generation stage [66, 75, 74]. For poroelasticity IGA was first adopted for the intact porous materials [71], and developed subsequently for fractured and/or fracturing porous media using hydromechanical interface elements [72, 140, 32, 33, 59]. Later, the extension was made to the simulation of non-Newtonian fluids and multi-phase flows [58, 62, 61, 60].

De Luycker *et al.* [39] were first to develop an extended isogeometric approach (XIGA), blending concepts of XFEM and IGA. This is possible owing to the fact that B-spline and NURBS basis functions form a partition of unity, which is necessary to define extra layers of

approximants. Unlike the original work, compatibility enforcement was absent in later XIGA contributions [53, 95], which is, however, necessary to render the original and the extra layers consistent. This is of utmost importance, particularly for XIGA, where higher interelement continuity at the element boundaries extends the discontinuous domain to the intact zones, but then in an incorrect manner. For this reason compatibility enforcement was studied comprehensively when trying to develop XIGA for cohesive fracture [44]. The consequences of an incomplete enforcement were also observed in a study on geometric nonlinearity [46]. More recently, IGA was extended with a local maximum entropy (LME), coined X-IGALME [45], in order to blend finite element and meshfree methods. This approach yields some outstanding features, in particular the singularity-free property of X-IGALME regardless of the crack location within the mesh, which is a major issue in element-based extended approaches [146]

Herein, XIGA is adopted to model fracturing in a fully saturated porous media. Rate-independent, isotropic linear elasticity is used for the solid skeleton, and a cohesive-zone model governs at the crack propagation. A small displacement gradient is assumed throughout. Poroelasticity is considered for the interstitial fluid, while a discontinuous pressure (two degrees of freedom) model defines the fluid behaviour at the discontinuity [37, 121]. Non-Uniform Rational B-Splines (NURBS) are adopted for the discretisation. They are cast within a standard finite element data structure using Bézier extraction [22, 72].

First, the governing equations are briefly summarised for the poromechanical problem, including the governing relations at the discontinuity. They are linearised and discretised using Bézier extraction-based NURBS and incorporated in a standard finite element matrix notation. Next, implementation aspects are covered, encompassing compatibility, enrichment, integration and crack extension. The contribution concludes with case studies which demonstrate the capability of the proposed approach in modelling a stationary fracture, followed by a study of a progressively fracturing porous medium, comprising straight and curved crack paths.

6.2 Mechanical problem

A fully saturated porous body Ω is considered, which contains a discontinuity Γ_d, see Figure 6.1. In the absence of the acceleration and body forces, the quasi-static equilibrium equation reads:

$$\begin{cases} \nabla \cdot \boldsymbol{\sigma} = & 0 & \mathbf{x} \in \Omega \\ \mathbf{u} = & \overline{\mathbf{u}} & \mathbf{x} \in \Gamma_u \\ \mathbf{n}_t \cdot \boldsymbol{\sigma} = & \overline{\mathbf{t}} & \mathbf{x} \in \Gamma_t \\ \mathbf{n}_{\Gamma_d} \cdot \boldsymbol{\sigma} = & \mathbf{t}_d & \mathbf{x} \in \Gamma_d \end{cases}, \tag{6.1}$$

where $\boldsymbol{\sigma}$ is the Cauchy stress tensor, $\mathbf{n}_{\Gamma_d}$ and $\mathbf{n}_t$ are the vectors normal to the fracture

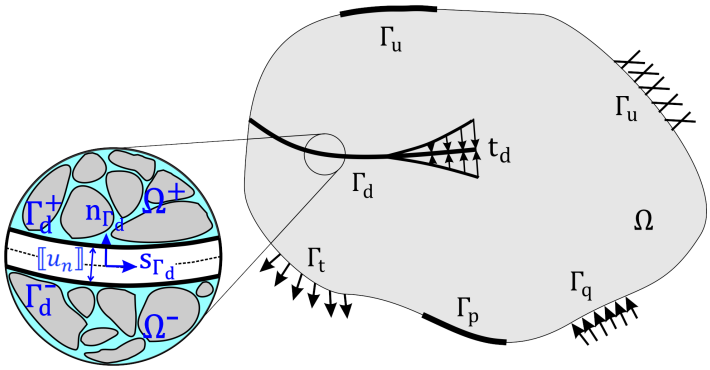

Figure 6.1: Boundary value problem Ω with the discontinuity Γ_d and cohesive tractions $\mathbf{t}_d$.

and the external traction surface Γ_t, respectively. The prescribed values for displacements and tractions are referred to as $\bar{\mathbf{u}}$ and $\bar{\mathbf{t}}$, respectively. The discontinuity is imposed within the displacement field with a Heaviside function $\mathbf{n}_{\Gamma_d} \cdot \nabla \mathcal{D}_{\Gamma_d} = \mathcal{H}_{\Gamma_d}$, where $\mathcal{D}_{\Gamma_d}$ is the sign distance function, leading to $\mathbf{u} = \hat{\mathbf{u}} + \mathcal{H}_{\Gamma_d}\,\tilde{\mathbf{u}}$ which is comprised of continuous (standard) $\hat{\square}$ and discontinuous (enhanced) $\tilde{\square}$ parts [44].

Recalling the small displacement assumption and its gradient, the infinitesimal strain field becomes:

$$\boldsymbol{\epsilon} = \nabla \hat{\mathbf{u}} + \mathcal{H}_{\Gamma_d} \nabla \tilde{\mathbf{u}} + 2\delta_{\Gamma_d} \left(\tilde{\mathbf{u}} \otimes \mathbf{n}_{\Gamma_d} \right), \tag{6.2}$$

where δ_{Γ_d} is the Dirac-delta and follows the identity $\mathbf{n}_{\Gamma_d} \cdot \nabla \mathcal{H}_{\Gamma_d} = 2\delta_{\Gamma_d}$. The constitutive law for the solid part yields:

$$\boldsymbol{\sigma}_s = \mathbf{D} : \boldsymbol{\epsilon}, \tag{6.3}$$

where $\mathbf{D}$ is the fourth-order linear-elastic stiffness tensor. Accordingly, the total stress tensor used in Equation (6.1) reads:

$$\boldsymbol{\sigma} = \boldsymbol{\sigma}_s - \alpha p \mathbf{1}. \tag{6.4}$$

α and p are the Biot coefficient and the pore fluid pressure, respectively. $\mathbf{1}$ indicates the identity matrix.

6.2.1 Governing weak forms

Now, the weak form of Equation (6.1) is written to set the scene for the discretisation:

$$\int_\Omega \nabla \delta \mathbf{u} : \boldsymbol{\sigma} \, \mathrm{d}\Omega + \int_{\Gamma_d} \delta [\![\mathbf{u}]\!] \cdot (\mathbf{n}_{\Gamma_d} \cdot \boldsymbol{\sigma}) \, \mathrm{d}\Gamma = \int_{\Gamma_t} \delta \mathbf{u} \cdot \bar{\mathbf{t}} \, \mathrm{d}\Gamma. \tag{6.5}$$

Inserting the displacement jump $[\![\mathbf{u}]\!] = \mathbf{u}^+ - \mathbf{u}^-$ into Equation 6.5 and defining a test function for the displacement field, $\delta\mathbf{u} = \delta\hat{\mathbf{u}} + \mathcal{H}_{\Gamma_d}\delta\tilde{\mathbf{u}}$, yields:

$$\int_\Omega \nabla\delta\mathbf{u} : \boldsymbol{\sigma}\,\mathrm{d}\Omega + 2\int_{\Gamma_d} \delta\tilde{\mathbf{u}} \cdot (\mathbf{n}_{\Gamma_d} \cdot \boldsymbol{\sigma})\,\mathrm{d}\Gamma = \int_{\Gamma_t} \delta\mathbf{u} \cdot \bar{\mathbf{t}}\,\mathrm{d}\Gamma, \tag{6.6}$$

where

$$\mathbf{n}_{\Gamma_d} \cdot \boldsymbol{\sigma} = \mathbf{t}_d - p\,\mathbf{n}_{\Gamma_d}, \tag{6.7}$$

with t_d denoting the cohesive traction at the discontinuity. Equation (6.6) decomposes into two separate equations for $\delta\hat{\mathbf{u}}$ and $\delta\tilde{\mathbf{u}}$,

$$\int_\Omega \nabla\delta\hat{\mathbf{u}} : \boldsymbol{\sigma}\,\mathrm{d}\Omega = \int_{\Gamma_t} \delta\hat{\mathbf{u}} \cdot \bar{\mathbf{t}}\,\mathrm{d}\Gamma, \tag{6.8a}$$

$$\int_\Omega \mathcal{H}_{\Gamma_d}\nabla\delta\tilde{\mathbf{u}} : \boldsymbol{\sigma}\,\mathrm{d}\Omega + 2\int_{\Gamma_d} \delta\tilde{\mathbf{u}} \cdot (\mathbf{n}_{\Gamma_d} \cdot \boldsymbol{\sigma})\,\mathrm{d}\Gamma = \int_{\Gamma_t} \mathcal{H}_{\Gamma_d}\,\delta\tilde{\mathbf{u}} \cdot \bar{\mathbf{t}}\,\mathrm{d}\Gamma. \tag{6.8b}$$

Similar to Section 2.2.3 a cohesive-zone model with an exponential decay is used for the traction-relative opening relation at the discontinuity.

6.3 Poromechanical problem

Next, the mass balance of an isotropic fully saturated porous medium is stated to complement the momentum balance given in Section 6.2. The interstitial fluid pressure can be computed from the mass conservation of the mixture:

$$\begin{cases} \alpha\nabla\cdot\dot{\mathbf{u}} + \nabla\cdot\mathbf{q} + \frac{1}{M}\dot{p} = & 0 & \mathbf{x}\in\Omega \\ p = & \bar{p} & \mathbf{x}\in\Gamma_p \\ \mathbf{n}_q\cdot\mathbf{q} = & \bar{q} & \mathbf{x}\in\Gamma_q \\ \mathbf{n}_{\Gamma_d}\cdot\mathbf{q} = & q_d & \mathbf{x}\in\Gamma_d \end{cases}, \tag{6.9}$$

where M is the Biot modulus:

$$\frac{1}{M} = \frac{\alpha - n_f}{K_s} + \frac{n_f}{K_f}, \tag{6.10}$$

with n_f the porosity of the medium, and K_s and K_f the solid and fluid bulk moduli, respectively.

The prescribed pressure and fluid flux are indicated by $\bar{p}$ and $\bar{q}$, respectively. $\mathbf{n}_q$ denotes the normal to the external flux surface. In this contribution we have chosen a discontinuous

pressure field, i.e. $p = \hat{p} + \mathcal{H}_{\Gamma_d}\tilde{p}$, which leads to a discontinuous fluid flux:

$$\mathbf{q} = -k_f \nabla p = -k_f \left(\underbrace{\nabla \hat{p}}_{\text{continuous}} + \underbrace{\mathcal{H}_{\Gamma_d} \nabla \tilde{p} + 2\mathbf{n}_{\Gamma_d}^{\mathrm{T}} \delta_{\Gamma_d} \tilde{p}}_{\text{discontinuous}} \right), \tag{6.11}$$

with k_f denoting the effective permeability, $k_f = k/\mu$. k and μ are the intrinsic permeability of the porous medium and the viscosity of the fluid, respectively. This is similar to a 2PDOF model of the fluid flow inside the fracture [37, 47].

Since the fluid pressure and flux are assumed to be discontinuous across the discontinuity, the weak form reads:

$$-\int_\Omega \alpha\, \delta p\, \nabla \cdot \dot{\mathbf{u}}\, \mathrm{d}\Omega - \int_\Omega k_f\, \nabla \delta p\, \nabla p\, \mathrm{d}\Omega - \int_\Omega \delta p\, \frac{1}{M}\, \dot{p}\, \mathrm{d}\Omega + \int_{\Gamma_d} \delta p\, \mathbf{n}_{\Gamma_d} \cdot [\![\mathbf{q}_d]\!]\, \mathrm{d}\Gamma = \int_{\Gamma_q} \delta p\, \mathbf{n} \cdot \bar{\mathbf{q}}\, \mathrm{d}\Gamma. \tag{6.12}$$

In the absence of an independent pressure degree of freedom inside the fracture, Equation (6.7) becomes:

$$\mathbf{n}_{\Gamma_d} \cdot \boldsymbol{\sigma} = t_d. \tag{6.13}$$

A 2PDOF model does not allow for the fluid flow along the fracture. Rather, the pressure jump is employed to directly compute the flux difference between the crack faces:

$$-\int_\Omega \alpha\, \delta p\, \nabla \cdot \dot{\mathbf{u}}\, \mathrm{d}\Omega - \int_\Omega k_f\, \nabla \delta p\, \nabla p\, \mathrm{d}\Omega - \int_\Omega \delta p\, \frac{1}{M}\, \dot{p}\, \mathrm{d}\Omega - \int_{\Gamma_d} k_d \delta \tilde{p}\, [\![p_n]\!]\, \mathrm{d}\Gamma = \int_{\Gamma_q} \delta p\, \mathbf{n} \cdot \bar{\mathbf{q}}\, \mathrm{d}\Gamma, \tag{6.14}$$

where k_d is the fracture permeability. It is noted that, based on the Heaviside sign function, the pressure jump becomes $[\![\mathbf{p}]\!] = \{[\![p_s]\!], [\![p_n]\!]\} = (\mathcal{H}^+_{\Gamma_d} - \mathcal{H}^-_{\Gamma_d})\tilde{p} = 2\tilde{p}$. Equation (6.14) can be decomposed as:

$$-\int_\Omega \alpha\, \delta \hat{p}\, \nabla \cdot \dot{\mathbf{u}}\, \mathrm{d}\Omega - \int_\Omega k_f\, \nabla \delta \hat{p}\, \nabla p\, \mathrm{d}\Omega - \int_\Omega \delta \hat{p}\, \frac{1}{M}\, \dot{p}\, \mathrm{d}\Omega = \int_{\Gamma_q} \delta \hat{p}\, \mathbf{n} \cdot \bar{\mathbf{q}}\, \mathrm{d}\Gamma, \tag{6.15a}$$

$$-\int_\Omega \mathcal{H}_{\Gamma_d}\, \alpha\, \delta \tilde{p}\, \nabla \cdot \dot{\mathbf{u}}\, \mathrm{d}\Omega - \int_\Omega \mathcal{H}_{\Gamma_d}\, k_f\, \nabla \delta \tilde{p}\, \nabla p\, \mathrm{d}\Omega - \int_\Omega \mathcal{H}_{\Gamma_d}\, \frac{1}{M}\, \delta \tilde{p}\, \dot{p}\, \mathrm{d}\Omega - 2\int_{\Gamma_d} k_d \delta \tilde{p}\, \tilde{p}\, \mathrm{d}\Gamma = \int_{\Gamma_q} \mathcal{H}_{\Gamma_d}\, \delta \tilde{p}\, \mathbf{n} \cdot \bar{\mathbf{q}}\, \mathrm{d}\Gamma. \tag{6.15b}$$

6.4 Linearised and discretised equations

6.4.1 Bézier extraction based NURBS

A univariate B-spline basis function can be cast in terms of the Bézier extraction operator $\mathbf{C}$ and a univariate Bernstein polynomial $\boldsymbol{\mathcal{B}}$ within the input domain $[-1\ 1]$:

$$\mathbf{N}^e = \mathbf{C}^e \boldsymbol{\mathcal{B}}, \tag{6.16}$$

with

$$\mathcal{B}_{k,m}(\xi) = \frac{1}{2}(1-\xi)\mathcal{B}_{k,m-1}(\xi) + \frac{1}{2}(1+\xi)\mathcal{B}_{k-1,m-1}(\xi), \tag{6.17a}$$

$$\mathcal{B}_{1,0}(\xi) \equiv 1, \tag{6.17b}$$

$$\mathcal{B}_{k,m}(\xi) \equiv 0 \qquad \text{if} \quad k < 1 \quad \text{or} \quad k > m+1. \tag{6.17c}$$

where the superscript e indicates the element index and m denotes the order of the underlying knot vector. Making use of the tensor product a bivariate Bernstein polynomial results:

$$\mathcal{B}^{m,n}_{k,l}(\xi,\eta) = \mathcal{B}_{k,m}(\xi) \otimes \mathcal{B}_{l,n}(\eta). \tag{6.18}$$

Defining w_k as the weight of the corresponding knot and univariate B-spline basis functions N and M, the bivariate NURBS basis function reads [22, 34]:

$$R^{m,n}_{k,l}(\xi,\eta) = \frac{N_{l,n}(\eta)N_{k,m}(\xi)w_{k,l}}{\sum_{\hat{k}}^{i}\sum_{\hat{l}}^{j} N_{\hat{k},m}(\eta)N_{\hat{l},n}(\xi)w_{\hat{k},\hat{l}}}. \tag{6.19}$$

A NURBS surface is then rendered by:

$$\mathbf{S}(\xi,\eta) = \sum_{k=1}^{j}\sum_{l=1}^{i} R^{m,n}_{k,l}(\xi,\eta)\mathbf{P}_{k,l}, \tag{6.20}$$

where $\mathbf{p}$ is the set of control points in the physical domain. In the classical integration approach, two pull backs are required to compute the quadrature, see Figure 2.1. Compliance with the finite element data structure removes this restriction as the information on the parametric domain is preserved in the Bézier extraction operator $\mathbf{C}$.

6.4.2 Discrete equations

The velocity of the solid particles $\dot{\mathbf{u}}$ and the fluid pressure field p are discretised,

$$\dot{\mathbf{u}} = \mathbf{R}_u\left(\dot{\hat{\mathbf{u}}} + \mathcal{H}_{\Gamma_d}\dot{\tilde{\mathbf{u}}}\right), \qquad p = \mathbf{R}_p\left(\hat{\mathbf{p}} + \mathcal{H}_{\Gamma_d}\tilde{\mathbf{p}}\right). \tag{6.21}$$

In a similar manner, test functions $\delta\mathbf{u}$ and δp are discretised as:

$$\delta\mathbf{u} = \mathbf{R}_u \left(\delta\hat{\mathbf{u}} + \mathcal{H}_{\Gamma_d}\delta\tilde{\mathbf{u}}\right), \qquad \delta p = \mathbf{R}_p \left(\delta\hat{\mathbf{p}} + \mathcal{H}_{\Gamma_d}\delta\tilde{\mathbf{p}}\right). \tag{6.22}$$

Employing a backward Euler scheme, $\dot{\square} = \frac{\square^{t+\Delta t} - \square^t}{\Delta t}$, the discretised format of the equilibrium equations, explicitly evaluated at $t + \Delta t$, becomes

$$\begin{aligned}
\mathbf{f}_{\hat{u}}^{\text{int},\, t+\Delta t} &= \mathbf{f}_{\hat{u}}^{\text{ext},\, t+\Delta t} \\
\mathbf{f}_{\tilde{u}}^{\text{int},\, t+\Delta t} &= \mathbf{f}_{\tilde{u}}^{\text{ext},\, t+\Delta t} \\
\mathbf{f}_{\hat{p}}^{\text{int},\, t+\Delta t} &= \mathbf{f}_{\hat{p}}^{\text{ext},\, t+\Delta t} \\
\mathbf{f}_{\tilde{p}}^{\text{int},\, t+\Delta t} &= \mathbf{f}_{\tilde{p}}^{\text{ext},\, t+\Delta t},
\end{aligned} \tag{6.23}$$

where the force vectors are given by:

$$\mathbf{f}_{\hat{u}}^{\text{ext},\, t+\Delta t} = \int_{\Gamma_\text{t}} \mathbf{R}_u^\text{T}\, \bar{\mathbf{t}}\, \text{d}\Gamma \tag{6.24a}$$

$$\mathbf{f}_{\tilde{u}}^{\text{ext},\, t+\Delta t} = \int_{\Gamma_\text{t}} \mathcal{H}_{\Gamma_d}\mathbf{R}_u^\text{T}\, \bar{\mathbf{t}}\, \text{d}\Gamma \tag{6.24b}$$

$$\mathbf{f}_{\hat{p}}^{\text{ext},\, t+\Delta t} = \Delta t \int_{\Gamma_\text{q}} \mathbf{R}_p^\text{T}\, \mathbf{n}^\text{T}\, \bar{\mathbf{q}}\, \text{d}\Gamma \tag{6.24c}$$

$$\mathbf{f}_{\tilde{p}}^{\text{ext},\, t+\Delta t} = \Delta t \int_{\Gamma_\text{q}} \mathcal{H}_{\Gamma_d}\mathbf{R}_p^\text{T}\, \bar{\mathbf{q}}\, \text{d}\Gamma, \tag{6.24d}$$

$$\mathbf{f}_{\hat{u}}^{\text{int},\, t+\Delta t} = \int_\Omega \mathbf{B}_u^\text{T}\, \left(\boldsymbol{\sigma}_s - \alpha\, \mathbf{m}\, (\mathbf{R}_p\hat{\mathbf{p}}^{t+\Delta t} + \mathcal{H}_{\Gamma_d}\mathbf{R}_p\tilde{\mathbf{p}}^{t+\Delta t})\right)\, \text{d}\Omega \tag{6.25a}$$

$$\mathbf{f}_{\tilde{u}}^{\text{int},\, t+\Delta t} = \int_\Omega \mathcal{H}_{\Gamma_d}\mathbf{B}_u^\text{T}\, \left(\boldsymbol{\sigma}_s - \alpha\, \mathbf{m}\, (\mathbf{R}_p\hat{\mathbf{p}}^{t+\Delta t} + \mathcal{H}_{\Gamma_d}\mathbf{R}_p\tilde{\mathbf{p}}^{t+\Delta t})\right)\, \text{d}\Omega + 2\int_{\Gamma_d} \mathbf{R}_u^\text{T}\, \mathbf{t}_d\, \text{d}\Gamma \tag{6.25b}$$

$$\begin{aligned}
\mathbf{f}_{\hat{p}}^{\text{int},\, t+\Delta t} = &-\int_\Omega \alpha\, \mathbf{R}_p^\text{T}\, \mathbf{m}^\text{T}\, \left(\mathbf{B}_u\hat{\mathbf{u}}^{t+\Delta t} + \mathcal{H}_{\Gamma_d}\mathbf{B}_u\tilde{\mathbf{u}}^{t+\Delta t}\right)\, \text{d}\Omega \\
-\Delta t\int_\Omega k_f\, \mathbf{B}_p^\text{T}\, \left(\mathbf{B}_p\, \hat{\mathbf{p}}^{t+\Delta t} + \mathcal{H}_{\Gamma_d}\mathbf{B}_p\, \tilde{\mathbf{p}}^{t+\Delta t}\right)\, \text{d}\Omega &- \int_\Omega \frac{1}{M}\, \mathbf{R}_p^\text{T}\, \left(\mathbf{R}_p\, \hat{\mathbf{p}}^{t+\Delta t} + \mathcal{H}_{\Gamma_d}\mathbf{R}_p\, \tilde{\mathbf{p}}^{t+\Delta t}\right)\, \text{d}\Omega \\
&+ \int_\Omega \alpha\, \mathbf{R}_p^\text{T}\, \mathbf{m}^\text{T}\, \left(\mathbf{B}_u\hat{\mathbf{u}}^t + \mathcal{H}_{\Gamma_d}\mathbf{B}_u\tilde{\mathbf{u}}^t\right)\, \text{d}\Omega + \int_\Omega \frac{1}{M}\, \mathbf{R}_p^\text{T}\, \left(\mathbf{R}_p\, \hat{\mathbf{p}}^t + \mathcal{H}_{\Gamma_d}\mathbf{R}_p\, \tilde{\mathbf{p}}^t\right)\, \text{d}\Omega
\end{aligned} \tag{6.25c}$$

$$\begin{aligned}
\mathbf{f}_{\tilde{p}}^{\mathrm{int},\,t+\Delta t} = &-\int_\Omega \mathcal{H}_{\Gamma_d}\alpha\,\mathbf{R}_p^{\mathrm{T}}\,\mathbf{m}^{\mathrm{T}}\,\left(\mathbf{B}_u\hat{\mathbf{u}}^{t+\Delta t}+\mathcal{H}_{\Gamma_d}\mathbf{B}_u\tilde{\mathbf{u}}^{t+\Delta t}\right)\,\mathrm{d}\Omega\\
&-\Delta t\int_\Omega \mathcal{H}_{\Gamma_d}k_f\,\mathbf{B}_p^{\mathrm{T}}\,\left(\mathbf{B}_p\,\hat{\mathbf{p}}^{t+\Delta t}+\mathcal{H}_{\Gamma_d}\mathbf{B}_p\,\tilde{\mathbf{p}}^{t+\Delta t}\right)\,\mathrm{d}\Omega\\
&-\int_\Omega \mathcal{H}_{\Gamma_d}\frac{1}{M}\,\mathbf{R}_p^{\mathrm{T}}\,\left(\mathbf{R}_p\,\hat{\mathbf{p}}^{t+\Delta t}+\mathcal{H}_{\Gamma_d}\mathbf{R}_p\,\tilde{\mathbf{p}}^{t+\Delta t}\right)\,\mathrm{d}\Omega-2\int_{\Gamma_d}k_d\,\mathbf{R}_p^{\mathrm{T}}\,\mathbf{R}_p\,\tilde{\mathbf{p}}^{t+\Delta t}\,\mathrm{d}\Gamma\\
&+\int_\Omega \mathcal{H}_{\Gamma_d}\alpha\,\mathbf{R}_p^{\mathrm{T}}\,\mathbf{m}^{\mathrm{T}}\,\left(\mathbf{B}_u\hat{\mathbf{u}}^{t}+\mathcal{H}_{\Gamma_d}\mathbf{B}_u\tilde{\mathbf{u}}^{t}\right)\,\mathrm{d}\Omega+\int_\Omega \mathcal{H}_{\Gamma_d}\frac{1}{M}\,\mathbf{R}_p^{\mathrm{T}}\,\left(\mathbf{R}_p\,\hat{\mathbf{p}}^{t}+\mathcal{H}_{\Gamma_d}\mathbf{R}_p\,\tilde{\mathbf{p}}^{t}\right)\,\mathrm{d}\Omega.
\end{aligned}\tag{6.25d}$$

Using the identity $\int_\Omega \delta_{\Gamma_d}(x)\phi(x)\,\mathrm{d}\Omega = \int_\Gamma \phi(x)\,\mathrm{d}\Gamma$ the linearised set of equations for a Newton-Raphson solution method reads:

$$\begin{bmatrix}
\mathbf{K}_{\hat{u}\hat{u}}^{\Omega} & \mathbf{K}_{\hat{u}\tilde{u}}^{\Omega} & \mathbf{K}_{\hat{u}\hat{p}}^{\Omega} & \mathbf{K}_{\hat{u}\tilde{p}}^{\Omega}\\
\mathbf{K}_{\tilde{u}\hat{u}}^{\Omega} & \mathbf{K}_{\tilde{u}\tilde{u}}^{\Omega}+\mathbf{K}_{\tilde{u}\tilde{u}}^{\Gamma_d} & \mathbf{K}_{\tilde{u}\hat{p}}^{\Omega} & \mathbf{K}_{\tilde{u}\tilde{p}}^{\Omega}\\
\mathbf{K}_{\hat{p}\hat{u}}^{\Omega} & \mathbf{K}_{\hat{p}\tilde{u}}^{\Omega} & \mathbf{K}_{\hat{p}\hat{p}}^{\Omega}+\mathbf{M}_{\hat{p}\hat{p}}^{\Omega} & \mathbf{K}_{\hat{p}\tilde{p}}^{\Omega}+\mathbf{M}_{\hat{p}\tilde{p}}^{\Omega}\\
\mathbf{K}_{\tilde{p}\hat{u}}^{\Omega} & \mathbf{K}_{\tilde{p}\tilde{u}}^{\Omega} & \mathbf{K}_{\tilde{p}\hat{p}}^{\Omega}+\mathbf{M}_{\tilde{p}\hat{p}}^{\Omega} & \mathbf{K}_{\tilde{p}\tilde{p}}^{\Omega}+\mathbf{M}_{\tilde{p}\tilde{p}}^{\Omega}+\Delta t\frac{\partial\mathbb{Q}_{\Gamma_d}}{\partial\tilde{p}}
\end{bmatrix}\begin{bmatrix}
\Delta\hat{\mathbf{u}}\\ \Delta\tilde{\mathbf{u}}\\ \Delta\hat{\mathbf{p}}\\ \Delta\tilde{\mathbf{p}}
\end{bmatrix}\tag{6.26}$$

$$=\begin{bmatrix}
\mathbf{f}_{\hat{u}}^{\mathrm{ext},\,t+\Delta t}\\ \mathbf{f}_{\tilde{u}}^{\mathrm{ext},\,t+\Delta t}\\ \mathbf{f}_{\hat{p}}^{\mathrm{ext},\,t+\Delta t}\\ \mathbf{f}_{\tilde{p}}^{\mathrm{ext},\,t+\Delta t}
\end{bmatrix}-\begin{bmatrix}
\mathbf{f}_{\hat{u}}^{\mathrm{int},\,t+\Delta t}\\ \mathbf{f}_{\tilde{u}}^{\mathrm{int},\,t+\Delta t}\\ \mathbf{f}_{\hat{p}}^{\mathrm{int},\,t+\Delta t}\\ \mathbf{f}_{\tilde{p}}^{\mathrm{int},\,t+\Delta t}
\end{bmatrix},$$

where $\mathbb{Q}_{\Gamma_d} = -2\int_{\Gamma_d} k_d\delta\tilde{p}\,\tilde{p}\,\mathrm{d}\Gamma$ represents the jump term in the flux over the fracture. The individual stiffness terms are given as

$$\mathbf{K}_{\hat{u}\hat{u}}^{\Omega} = \int_\Omega \mathbf{B}_u^{\mathrm{T}}\,\mathbf{D}\,\mathbf{B}_u\,\mathrm{d}\Omega \tag{6.27a}$$

$$\mathbf{K}_{\hat{u}\tilde{u}}^{\Omega} = \left(\mathbf{K}_{\tilde{u}\hat{u}}^{\Omega}\right)^{\mathrm{T}} = \int_\Omega \mathbf{B}_u^{\mathrm{T}}\,\mathbf{D}\,\mathbf{B}_u^{\mathrm{enr}}\,\mathrm{d}\Omega \tag{6.27b}$$

$$\mathbf{K}_{\hat{u}\hat{p}}^{\Omega} = \left(\mathbf{K}_{\hat{p}\hat{u}}^{\Omega}\right)^{\mathrm{T}} = -\int_\Omega \alpha\,\mathbf{B}_u^{\mathrm{T}}\,\mathbf{m}\,\mathbf{R}_p\,\mathrm{d}\Omega \tag{6.27c}$$

$$\mathbf{K}_{\hat{u}\tilde{p}}^{\Omega} = \left(\mathbf{K}_{\tilde{p}\hat{u}}^{\Omega}\right)^{\mathrm{T}} = -\int_\Omega \alpha\,\mathbf{B}_u^{\mathrm{T}}\,\mathbf{m}\,\mathbf{R}_p^{\mathrm{enr}}\,\mathrm{d}\Omega \tag{6.27d}$$

$$\mathbf{K}^{\Omega}_{\tilde{u}\tilde{u}} = \int_{\Omega} (\mathbf{B}^{\mathrm{enr}}_{u})^{\mathrm{T}}\ \mathbf{D}\,\mathbf{B}^{\mathrm{enr}}_{u}\,\mathrm{d}\Omega \tag{6.27e}$$

$$\mathbf{K}^{\Gamma_d}_{\tilde{u}\tilde{u}} = 4\int_{\Gamma_d} \mathbf{R}^{\mathrm{T}}_{u}\,\mathbf{Q}^{\mathrm{T}}\,\mathbf{T}\,\mathbf{Q}\,\mathbf{R}_{u}\,\mathrm{d}\Gamma \tag{6.27f}$$

$$\mathbf{K}^{\Omega}_{\tilde{u}\hat{p}} = \left(\mathbf{K}^{\Omega}_{\hat{p}\tilde{u}}\right)^{\mathrm{T}} = -\int_{\Omega} \alpha\ (\mathbf{B}^{\mathrm{enr}}_{u})^{\mathrm{T}}\ \mathbf{m}\,\mathbf{R}_{p}\,\mathrm{d}\Omega \tag{6.27g}$$

$$\mathbf{K}^{\Omega}_{\tilde{u}\tilde{p}} = \left(\mathbf{K}^{\Omega}_{\tilde{p}\tilde{u}}\right)^{\mathrm{T}} = -\int_{\Omega} \alpha\ (\mathbf{B}^{\mathrm{enr}}_{u})^{\mathrm{T}}\ \mathbf{m}\,\mathbf{R}^{\mathrm{enr}}_{p}\,\mathrm{d}\Omega \tag{6.27h}$$

$$\mathbf{K}^{\Omega}_{\hat{p}\hat{p}} = -\Delta t\int_{\Omega} k_f\,\mathbf{B}^{\mathrm{T}}_{p}\,\mathbf{B}_{p}\,\mathrm{d}\Omega \tag{6.27i}$$

$$\mathbf{M}^{\Omega}_{\hat{p}\hat{p}} = -\int_{\Omega} \frac{1}{M}\,\mathbf{R}^{\mathrm{T}}_{p}\,\mathbf{R}_{p}\,\mathrm{d}\Omega \tag{6.27j}$$

$$\mathbf{K}^{\Omega}_{\hat{p}\tilde{p}} = \left(\mathbf{K}^{\Omega}_{\tilde{p}\hat{p}}\right)^{\mathrm{T}} = -\Delta t\int_{\Omega} k_f\,\mathbf{B}^{\mathrm{T}}_{p}\,\mathbf{B}^{\mathrm{enr}}_{p}\,\mathrm{d}\Omega \tag{6.27k}$$

$$\mathbf{M}^{\Omega}_{\hat{p}\tilde{p}} = \left(\mathbf{M}^{\Omega}_{\tilde{p}\hat{p}}\right)^{\mathrm{T}} = -\int_{\Omega} \frac{1}{M}\,\mathbf{R}^{\mathrm{T}}_{p}\,\mathbf{R}^{\mathrm{enr}}_{p}\,\mathrm{d}\Omega \tag{6.27l}$$

$$\mathbf{K}^{\Omega}_{\tilde{p}\tilde{p}} = -\Delta t\int_{\Omega} k_d\ \left(\mathbf{B}^{\mathrm{enr}}_{p}\right)^{\mathrm{T}}\ \mathbf{B}^{\mathrm{enr}}_{p}\,\mathrm{d}\Omega \tag{6.27m}$$

$$\mathbf{M}^{\Omega}_{\tilde{p}\tilde{p}} = -\int_{\Omega} \frac{1}{M}\ \left(\mathbf{R}^{\mathrm{enr}}_{p}\right)^{\mathrm{T}}\ \mathbf{R}^{\mathrm{enr}}_{p}\,\mathrm{d}\Omega, \tag{6.27n}$$

where enriched strain-displacement matrices for a given Gauss point whose global location is indicated by $\mathbf{x}$ read:

$$\mathbf{B}^{\mathrm{enr}}_{u_i} = \mathcal{H}^{Bl}_{\Gamma_d}(\mathbf{x})\left(\mathcal{H}^{GP}_{\Gamma_d}(\mathbf{x}) - \mathcal{H}^{i}_{\Gamma_d}\right)\mathbf{B}_{u_i} = \mathcal{H}^{Bl}_{\Gamma_d}(\mathbf{x})\left(\mathcal{H}^{GP}_{\Gamma_d}(\mathbf{x}) - \mathcal{H}^{i}_{\Gamma_d}\right)\begin{bmatrix} \frac{\partial R_{u_i}}{\partial X_1} & 0 \\ 0 & \frac{\partial R_{u_i}}{\partial X_2} \\ \frac{\partial R_{u_i}}{\partial X_2} & \frac{\partial R_{u_i}}{\partial X_1} \end{bmatrix} \tag{6.28a}$$

$$\mathbf{B}^{\mathrm{enr}}_{p_i} = \mathcal{H}^{Bl}_{\Gamma_d}(\mathbf{x})\left(\mathcal{H}^{GP}_{\Gamma_d}(\mathbf{x}) - \mathcal{H}^{i}_{\Gamma_d}\right)\mathbf{B}_{p_i} = \mathcal{H}^{Bl}_{\Gamma_d}(\mathbf{x})\left(\mathcal{H}^{GP}_{\Gamma_d}(\mathbf{x}) - \mathcal{H}^{i}_{\Gamma_d}\right)\begin{bmatrix} \frac{\partial R_{p_i}}{\partial X_1} \\ \frac{\partial R_{p_i}}{\partial X_2} \end{bmatrix}. \tag{6.28b}$$

Next, the enriched basis functions yield:

$$\mathbf{R}^{\mathrm{enr}}_{u_i} = \mathcal{H}^{Bl}_{\Gamma_d}(\mathbf{x})\left(\mathcal{H}^{GP}_{\Gamma_d}(\mathbf{x}) - \mathcal{H}^{i}_{\Gamma_d}\right)\mathbf{R}_{u_i} = \mathcal{H}^{Bl}_{\Gamma_d}(\mathbf{x})\left(\mathcal{H}^{GP}_{\Gamma_d}(\mathbf{x}) - \mathcal{H}^{i}_{\Gamma_d}\right)\begin{bmatrix} R_{u_i} & 0 \\ 0 & R_{u_i} \end{bmatrix} \tag{6.29a}$$

$$R^{\mathrm{enr}}_{p_i} = \mathcal{H}^{Bl}_{\Gamma_d}(\mathbf{x})\left(\mathcal{H}^{GP}_{\Gamma_d}(\mathbf{x}) - \mathcal{H}^{i}_{\Gamma_d}\right)R_{p_i} \tag{6.29b}$$

with X_1 and X_2 denoting the global coordinates system, $i = 1, \cdots, n_{\mathrm{enr}}$ the index of the enriched control point, and n_{enr} indicating the total number of the enriched control points

within the element under consideration.

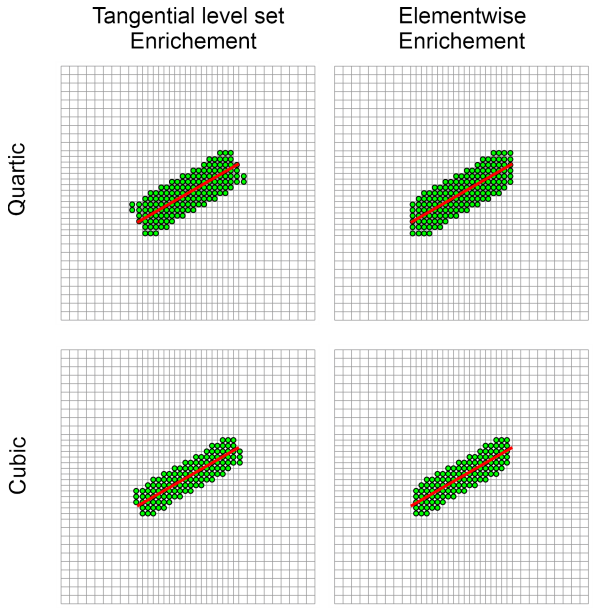

Figure 6.2: Enrichment schemes for quartic and cubic NURBS. Only enriched control points are shown for the sake of clarity.

6.5 Implementation aspects

Different from the enrichment scheme used in the standard finite element method, the interelement overlap of the NURBS basis functions impedes the straightforward enhancement of control points. The reason lies in the $\mathcal{C}^{\mathrm{p}}$-continuity ($\mathrm{p} > 0$) at the element boundaries. This increases with p-refinement [133], i.e. continuity elevation.

It is important in fluid-saturated porous media to satisfy the Ladyzhenskaya-Babuška-Brezzi condition [24, 26], and therefore, to restrict the order of continuity of the solid part to be one higher than that of the interstitial fluid pressure [113]. Moreover, a quadratic (second-order) NURBS is the minimum continuity-order requirement to guarantee a continuous pressure gradient across element boundaries. Herein, we have adopted quartic ($\mathcal{C}^3$) and cubic ($\mathcal{C}^2$) NURBS for the solid and the fluid parts, respectively. Implications of this choice are discussed in the section with the numerical examples.

6.5.1 Enhancement of individual control points

The interelement sharing of control points in IGA increases with order elevation. This is a complication when developing a general scheme for elementwise crack propagation in XIGA [44]. It is crucial that a control point at, or in front of the crack tip is not enriched, even it

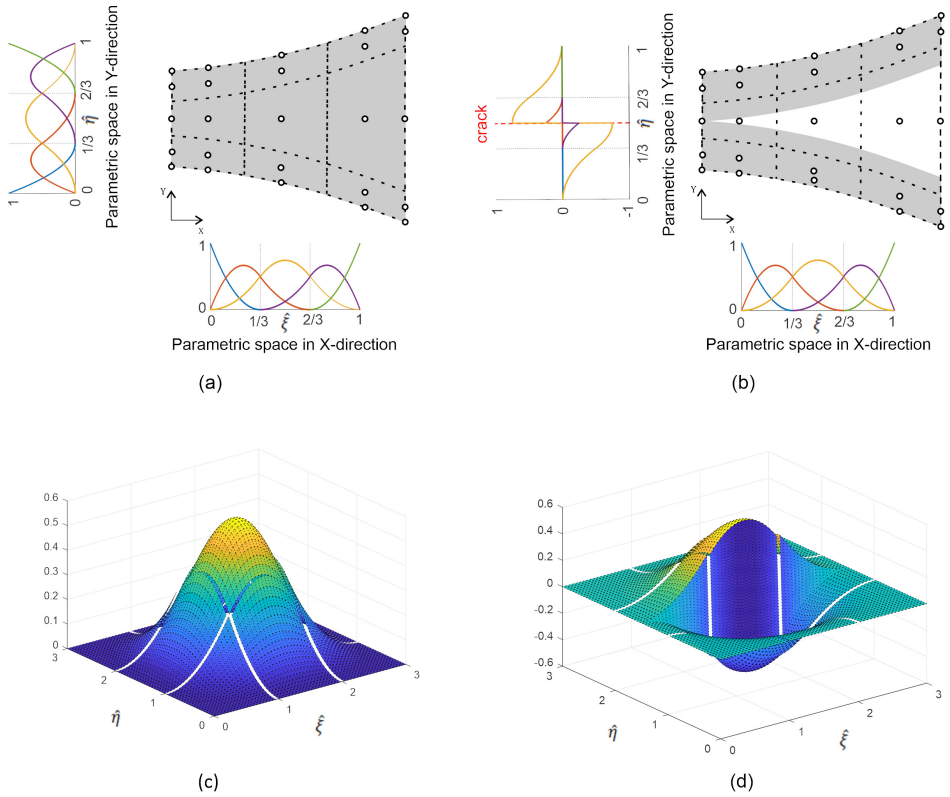

Figure 6.3: Shifted basis functions for quadratic NURBS under mode-I fracture. Univariate NURBS basis functions are shown for intact (a) and shifted discontinuous media (b). The tensor product has been exploited to increase the dimension for bivariate surfaces of intact (c) and shifted discontinuous media (d). Please note that the values at (c) and (d) are illustrated for the control point in the centre of the medium, i.e. tensor product of the yellow curves in (a) and (b).

belongs to cracked elements. The front is defined in two ways, by means of the tangential level-set or the elementwise approach, represented in Figure 6.2. This is further discussed in the ensuing sections, particularly see Figure 6.4 in Section 6.5.2.

6.5.2 Compatibility enforcement

A proper extended approach preserves the compatibility between the standard and the enhanced fields. For Lagrange basis functions, which provide $\mathcal{C}^0$-continuity at element boundaries, shifting and blending were adopted to successfully enforce compatibility [77, 93].

For IGA, however, the interelement share of the control points complicates compatibility enforcement as the control points are not located at element edges. The blending technique has been adopted by De Luycker et al. [39], while shifting has been studied for XIGA as well [44], see Figure 6.3. It was observed that full enforcement of the compatibility between standard and enhanced fields is almost impossible in XIGA. Nevertheless, shifting localises the

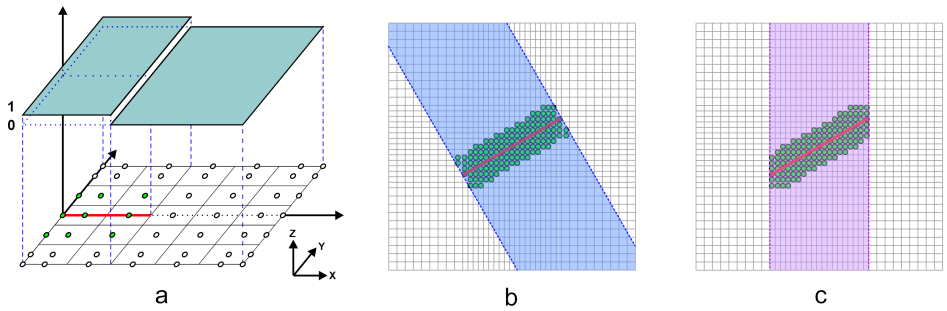

Figure 6.4: Compatibility enforcement in the form of the blending technique. (a) illustrates a Heaviside step function for an edge cracked plate, and active and inactive domains are denoted by 1 and 0, respectively. Enriched control points are designated by green circles, and the red line denotes the crack path. The blending technique is realised by level-set (b) and elementwise (c) enrichments for an inclined crack. The highlighted areas denote the domains where the Heaviside blending function returns 1.

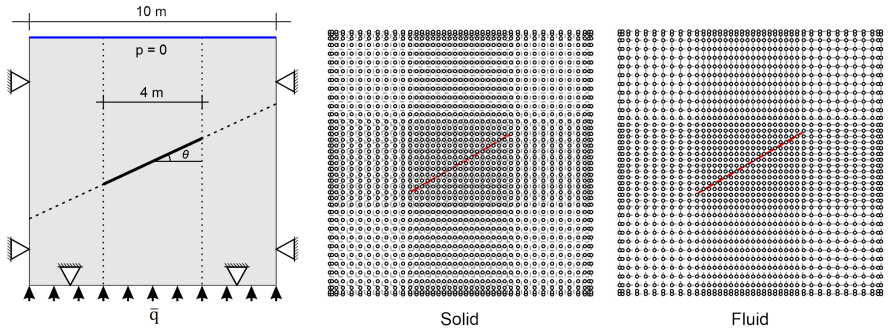

Figure 6.5: Square plate with a centre crack. Discretisations of the solid (quartic) and the fluid (cubic) are shown.

effect of the enhanced terms to a narrow region perpendicular to the crack path. Therefore, using a fairly fine mesh renders an almost negligible width. Noteworthy is that the XIGA with shifting performs better than XFEM for fine meshes, while XFEM is superior for coarse meshes owing to the full compatibility enforcement [46]. Loss of optimal convergence and divergence of the solution are possible consequences of a weak compatibility enforcement for coarse meshes.

Since control points are shared between elements in IGA, domain excess of the enhanced fields occurs, as the tip element shares enriched control points with the element in the front. This causes an unwanted opening of the domain in front of the crack. This can be avoided by adopting a Heaviside step function, see Figure 6.4. Employing shifting and blending Equations (6.21-6.22) become:

$$\dot{\mathbf{u}}(\mathbf{x}) = \sum_{\mathbb{A}\in\mathcal{N}} \mathbf{R}_{u_\mathbb{A}}(\mathbf{x})\,\dot{\hat{\mathbf{u}}}_\mathbb{A} + \sum_{\mathbb{B}\in\mathcal{N}^\mathcal{H}} \mathcal{H}^{Bl}_{\Gamma_d}(\mathbf{x}) \left(\mathcal{H}^{GP}_{\Gamma_d}(\mathbf{x}) - \mathcal{H}^{\mathbb{B}}_{\Gamma_d}\right) \mathbf{R}_{u_\mathbb{B}}(\mathbf{x})\,\dot{\hat{\mathbf{u}}}_\mathbb{B} \tag{6.30a}$$

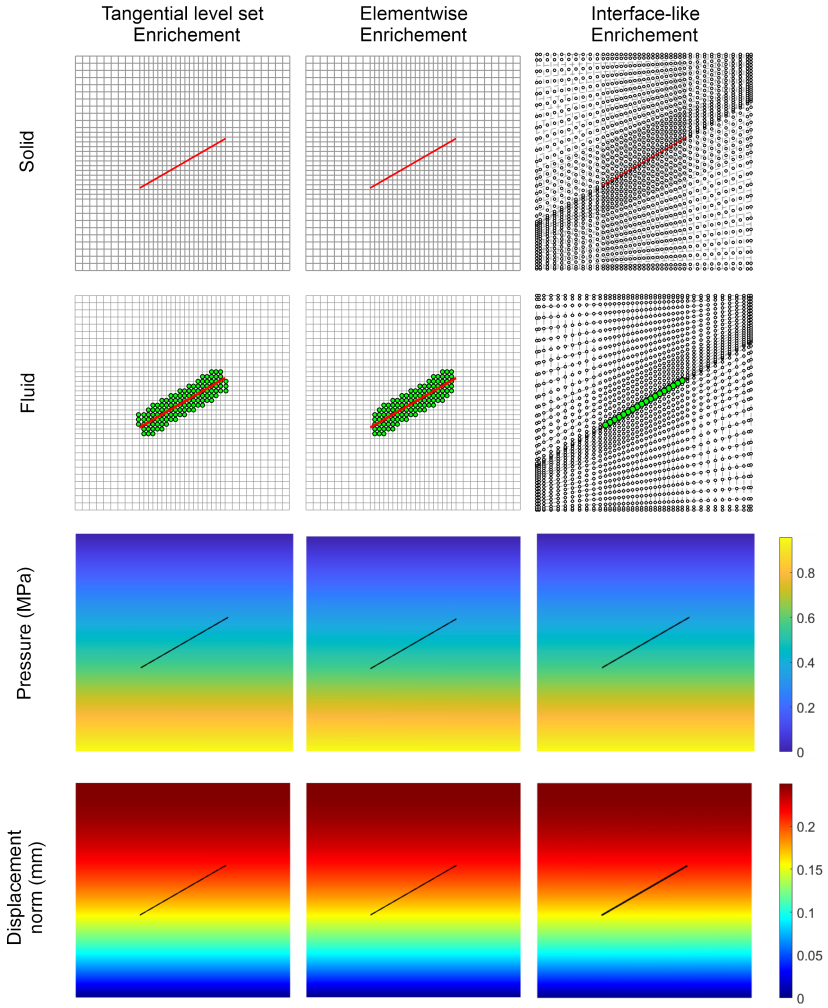

Figure 6.6: Enrichment schemes for the sqaure plate with the centre crack ($\theta = 30°$). No enrichment for solid has been adopted.

$$p(\mathbf{x}) = \sum_{\mathbb{A}\in\mathcal{N}} \mathbf{R}_{p_\mathbb{A}}(\mathbf{x})\,\hat{\mathbf{p}}_\mathbb{A} + \sum_{\mathbb{B}\in\mathcal{N}^\mathcal{H}} \mathcal{H}^{Bl}_{\Gamma_d}(\mathbf{x}) \left(\mathcal{H}^{GP}_{\Gamma_d}(\mathbf{x}) - \mathcal{H}^{\mathbb{B}}_{\Gamma_d}\right) \mathbf{R}_{p_\mathbb{B}}(\mathbf{x})\,\tilde{\mathbf{p}}_\mathbb{B} \tag{6.30b}$$

$$\delta\mathbf{u}(\mathbf{x}) = \sum_{\mathbb{A}\in\mathcal{N}} \mathbf{R}_{u_\mathbb{A}}(\mathbf{x})\,\delta\hat{\mathbf{u}}_\mathbb{A} + \sum_{\mathbb{B}\in\mathcal{N}^\mathcal{H}} \mathcal{H}^{Bl}_{\Gamma_d}(\mathbf{x}) \left(\mathcal{H}^{GP}_{\Gamma_d}(\mathbf{x}) - \mathcal{H}^{\mathbb{B}}_{\Gamma_d}\right) \mathbf{R}_{u_\mathbb{B}}(\mathbf{x})\,\delta\tilde{\mathbf{u}}_\mathbb{B} \tag{6.30c}$$

$$\delta p(\mathbf{x}) = \sum_{\mathbb{A}\in\mathcal{N}} \mathbf{R}_{p_\mathbb{A}}(\mathbf{x})\,\delta\hat{\mathbf{p}}_\mathbb{A} + \sum_{\mathbb{B}\in\mathcal{N}^\mathcal{H}} \mathcal{H}^{Bl}_{\Gamma_d}(\mathbf{x}) \left(\mathcal{H}^{GP}_{\Gamma_d}(\mathbf{x}) - \mathcal{H}^{\mathbb{B}}_{\Gamma_d}\right) \mathbf{R}_{p_\mathbb{B}}(\mathbf{x})\,\delta\tilde{\mathbf{p}}_\mathbb{B} \tag{6.30d}$$

with $\mathcal{N}^\mathcal{H} \subset \mathcal{N}$ the subset enriched by the Heaviside sign function. $\mathcal{H}^{\mathbb{B}}_{\Gamma_d}$ and $\mathcal{H}^{GP}_{\Gamma_d}$ denote the values of the Heaviside sign function at the control point $\mathbb{B}$ and the Gauss point under consideration. $\mathcal{H}^{Bl}_{\Gamma_d}$ is the Heaviside step function defined at the Gauss point with respect to the crack tip [44]. The remaining discretised equations are shifted and blended accordingly, and the Heaviside terms are replaced by the new shifted and blended Heaviside function.

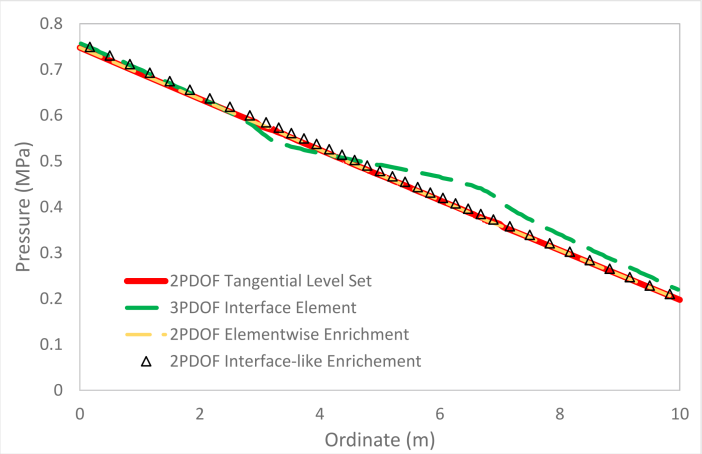

Figure 6.7: Pressure diagram along the crack: level-set based, elementwise and interface-like enrichments are reported. A 3PDOF standard interface element pressure profile [47] is also shown for comparison.

6.5.3 Direction of crack extension, integration scheme and point projection

The smoothness of NURBS basis functions provides a better estimate of stresses compared to Lagrange basis functions [22, 140]. Nevertheless, the local stress distribution varies significantly in the vicinity of the crack tip, suggesting a smoothing scheme to be employed. A non-local approach has been adopted here with the Gaussian weight function [144, 70]. Afterwards, the equivalent traction at the extension direction is compared to the fracture strength. Crack nucleation occurs upon satisfying this criterion at certain number of Gauss points along the path [46].

Herein, the standard Gauss quadrature is adopted for all integration processes in this chapter. Sub-triangulation have been used to guarantee a sufficient number of Gauss points, evenly distributed at each side of the crack. Making use of the extended approach, a discontinuity is created or extended upon satisfaction of the fracture criterion. This removes the need of a high dummy stiffness used in the interface element approach to avoid undesirable opening prior to fracturing and traction oscillations [141, 62, 72].

To carry out the line integration for the cohesive tractions a point projection is required [100]. Since degrees of freedom are not explicitly defined at the discontinuity, the line integration should also be computed in terms of the element degrees of freedom [46].

6.6 Numerical examples and discussion

The formulation is now assessed at the hand of some numerical examples. Different aspects are examined for stationary and fracturing discontinuities comprising straight and curved crack propagation.

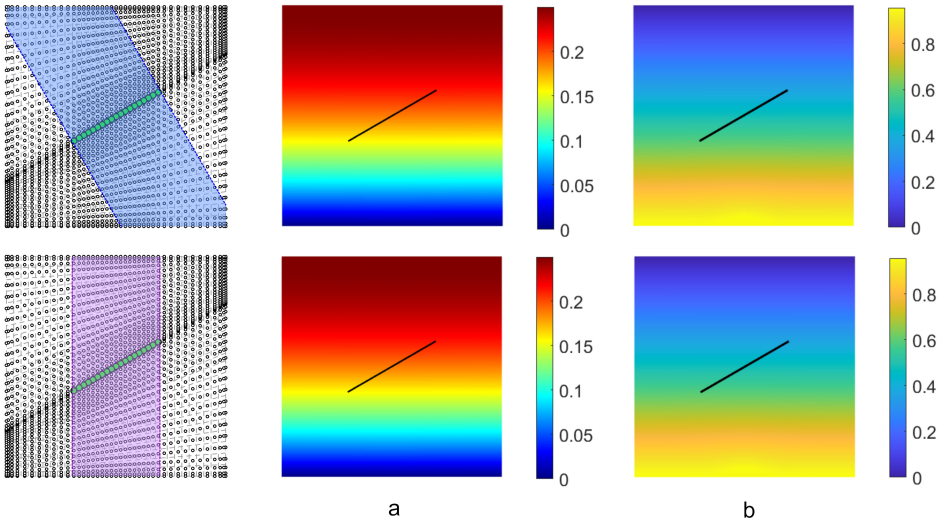

Figure 6.8: Assessment of the blending domain in the form of (a) displacement norm and (b) interstitial fluid pressure contours for interface-like enrichment. The top row denotes the level-set enrichment, while the elementwise enrichment is illustrated in the bottom row.

6.6.1 Stationary cracks: square plate with a centre crack

The first example concerns a stationary crack centred in a square plate, see Figure 6.5. A plane-strain condition is adopted and the discontinuity is assumed to be traction free. A constant flux $\bar{q} = 10^{-4}\ m/s$ is imposed at the bottom of the plate, while the fluid is allowed to flow freely at the top, see the blue edge in Figure 6.5. The other boundaries are impermeable. The material properties for the solid are as follows: Young's modulus $E = 9$ GPa, Poisson's ratio $\nu = 0.4$, Biot modulus $M = 10^{18}$ MPa, Biot coefficient $\alpha = 1$, porosity $n_f = 0.3$ and intrinsic permeability $k = 10^{-12}$ m^2. The fluid viscosity is taken $\mu = 1$ mPa.s. The domain is discretised in a non-uniform manner with a refinement in the centre, 37 and 35 elements in the horizontal and the vertical directions, respectively. A time step size $\Delta t = 1$ s has been used until the steady state situation at $t = 40$ s. The results are compared with findings from the interface elements [47].

Enrichment scheme

As noted in Section 6.5.1 two schemes can be adopted for the enrichment: a global scheme based on the tangential level-set and and a local scheme based on the tip element. These approaches become virtually indistinguishable for small inclinations, and identical for the limiting case of a horizontal crack. Figure 6.6 illustrates both enrichment schemes when $\theta = 30°$, see also Figure 6.2 for quartic and cubic NURBS. A clear difference is observed regarding the enriched control points at the tips of the crack. Regarding the solid part in

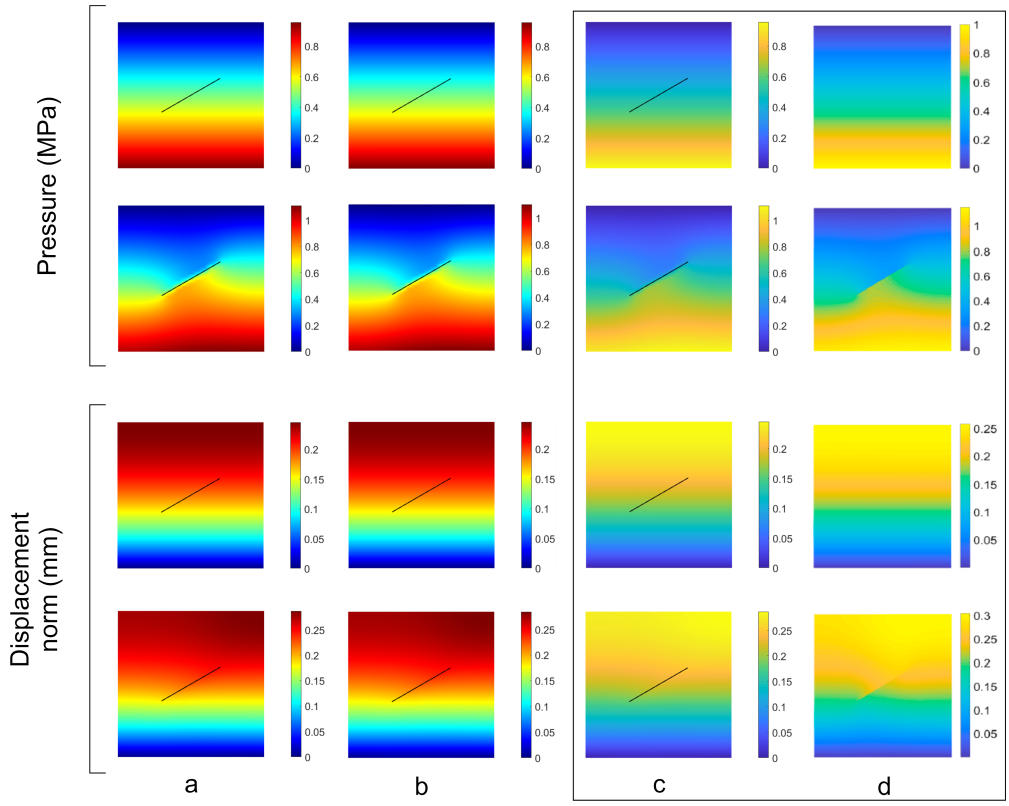

Figure 6.9: Effect of an impervious interface is compared with one with the same permeability of the interstitial fluid, $k_d = k_f$. Odd rows illustrate the permeable interface and even rows denote the impervious interface. (a) indicates the level-set and (b) shows the elementwise enrichment. For visualisation purposes, (c) portrays the column (a) in Parula colormap to compare with the results of the interface element [47] in (d).

Figure 6.6, no enrichment has been employed due to the discontinuous pressure (2PDOF) model, where the tangential fluid flow is absent inside the fracture. A similar remedy has been adopted when using interface elements [47].

To cover all the enrichment schemes an interface-like enrichment is also adopted here for the limiting case that the crack is on a $\mathcal{C}^0$-line between elements. Indeed, XIGA can be considered as a generalisation of isogeometric interface elements based on an interelement definition of the discontinuity. As observed from Figure 6.6 the only drawback of the interface-like enrichment is the need to adapt the crack to the mesh layout. Therefore, it also needs to know the extension path beforehand. On the other hand, there is no need to enforce compatibility perpendicular to the crack path as the enriched control points in interface-like enrichment only exist on the crack path shared between the cracked elements. Therefore, the shifting technique can be benchmarked against the results of interface-like enrichment perpendicular to the crack path. It is noted that in the tangential direction the blending

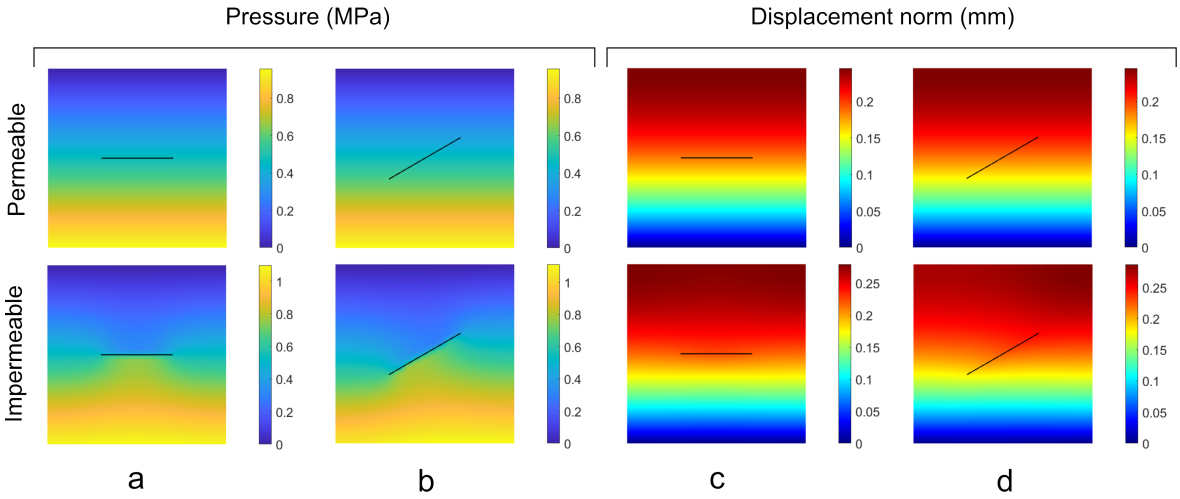

Figure 6.10: Crack orientation for permeable/impermeable fracture. (a) and (b) are $\theta = 0°$ and $30°$ for the pressure, similar to (c) and (d) for the displacement norm.

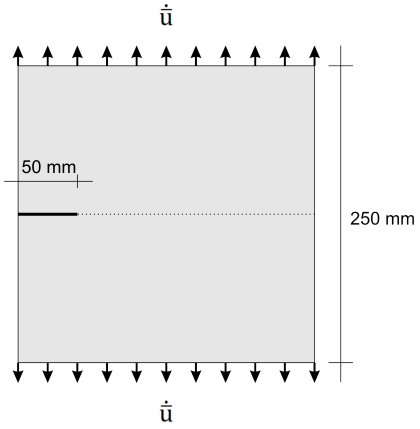

Figure 6.11: Pre-notched square plate subjected to mode-I fracture.

technique must still be adopted to remove the undesired effect of the enhanced terms ahead of the crack tip(s).

The results are now presented for the three schemes: level-set based, elementwise and interface-like enrichments, rendering nearly identical results in terms of the pressure, see Figure 6.6. They are also similar to the pressure contours reported by interface element approach [47]. This agreement is also supported by the pressure diagram along the discontinuity in Figure 6.7, confirming a good compatibility enforcement by shifting. The figure also includes a comparison with a three degree of freedom pressure (3PDOF) model for the interface [47], showing fairly similar results. This gives another confirmation that the present results are in the correct range. Furthermore, the two possible blending domains have been investigated for the interface-like enrichment, where the shifting technique is absent and only the blending

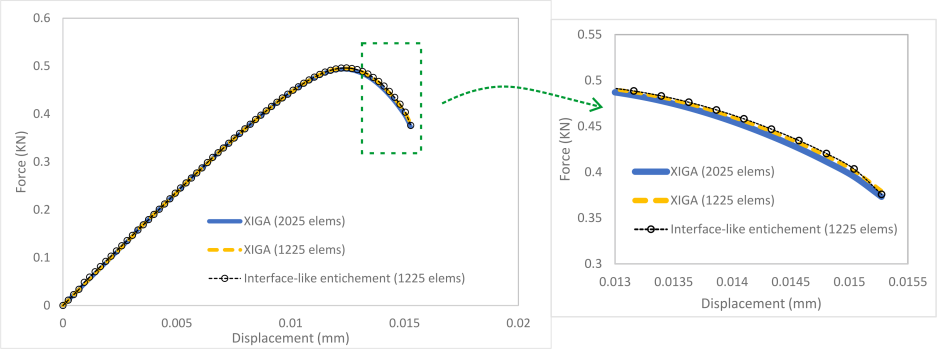

Figure 6.12: Force-displacement diagram for the single-edge notch test.

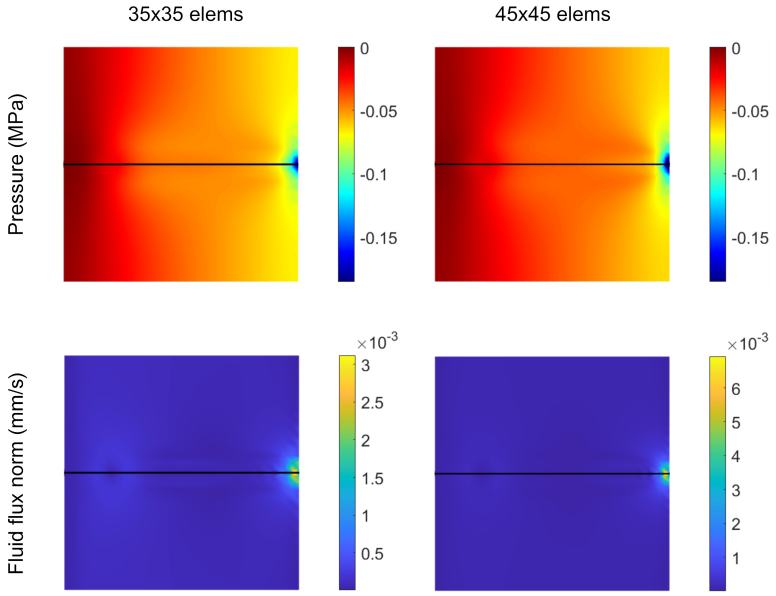

Figure 6.13: Pressure and norm of fluid flux contours for the single-edge notch test.

technique exists. The results represent an almost identical solution for both of these cases, see Figure 6.8, suggesting that both enrichments can be adopted for XIGA.

Level-set and elementwise enrichments differ when departing from the horizontal crack. In contrast with the differences observed in the two enrichment schemes in XIGA, compare the enrichments in Figure 6.2, the results match very well, underscoring the above remark about viability of both suggested enrichment approaches.

Fracture permeability

To investigate the effect of the interface permeability on the saturated porous media, interstitial fluid pressure and displacement norm are explored for $k_d = k_f$ and $k_d = 0$, to investigate

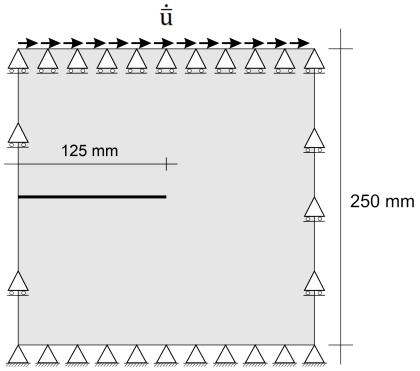

Figure 6.14: Pre-notched square plate subjected to shear loading at the top.

the effect of the permeability of the interface. The results are similar for level-set and elementwise enrichments, as expected, see Figure 6.9. The results have also been compared with the findings from 2PDOF standard interface elements [47] in the box in Figure 6.9. An excellent agreement is observed.

Finally, the effect of the crack orientation has been investigated for $\theta = 0^\circ$ and 30° in Figure 6.10. Neither the interstitial fluid pressure nor the displacements 'see' the crack for $k_d = k_f$, as should be. On the contrary, when $k_d = 0$, different patterns in the fluid pressure are observed, as shown in Figure 6.10. Hence, the fluid pressure makes the displacement field to recognise the presence of the crack, which shows the existence of the solid-fluid interaction.

6.6.2 Fracturing: single edge notch test

Straight crack propagation has been examined for a square plate with an edge notch under plane-strain condition, see Figure 6.11. The notch is assumed traction free, while a cohesive-zone model is used for the fracturing. Therefore the solid as well as the fluid phases are enriched. The simulation is carried out using the following material properties: Young's modulus $E = 25.85$ GPa, Poisson's ratio $\nu = 0.18$, Biot modulus $M = 10^{18}$ MPa, Biot coefficient $\alpha = 1$, porosity $n_f = 0.2$, intrinsic permeability $k = 2.78 \times 10^{-10}$ mm^2, solid bulk modulus $K_s = 13.46$ GPa, fluid bulk modulus $K_f = 0.2$ GPa, fluid viscosity $\mu = 1$ mPa.s, fracture energy $G_f = 0.095$ N/mm and fracture strength $f_t = 2.7$ MPa. Vertical velocities $\dot{\bar{u}} = 2.35 \times 10^{-3}$ mm/s are applied at the top and the bottom of the plate. Two discretisations, 35×35 and 45×45, are investigated using a quartic-cubic (solid-fluid) NURBS mesh. Similar to Section 6.6.1, an interface-like enrichment serves as a benchmark to validate the results. It is noted that the level-set and elementwise enrichments render the same results.

The load-displacement diagram in Figure 6.12 shows an excellent agreement between the discretisations for XIGA and the limiting case of the interface-like enrichment. Moreover, a comparison between the two discretisations is given for the interstitial fluid pressure and the

norm of the fluid flux in Figure 6.13. Again, a close agreement is observed.

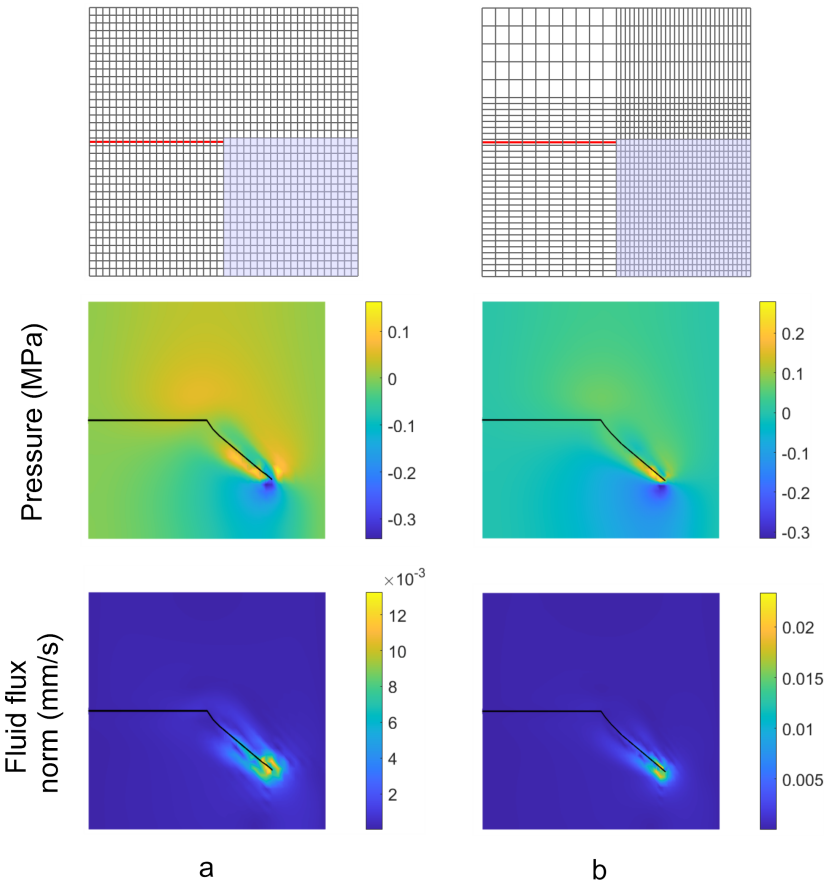

Figure 6.15: Single edge notch test: (a) uniform mesh with 1400 elements (360 elements at the highlighted section): (b) locally refined mesh with 1400 elements (690 elements at the highlighted section). The pressure and fluid flux contours are illustrated for each case.

6.6.3 Arbitrary propagation: single edge notch test

Extended approaches have been designed to capture arbitrary crack propagation. To examine this feature for XIGA in the context of fluid-saturated porous media, the single-edge notch test is considered again, Figure 6.14. The plate is subjected to a horizontal loading $\dot{\bar{u}} = 0.05$ mm/s at the top. The length of the notch extends to the centre of the plate, and the material properties are as in Section 6.6.2. In view of the results in the previous sections, only the level-set enrichment is utilised here.

Two discretisations with the same number of elements, but with a different mesh layout, have been considered. The results, in the form of contours of the pressure and the norm of the fluid flux, are illustratd in Figure 6.15. It is observed that the crack paths and the contour

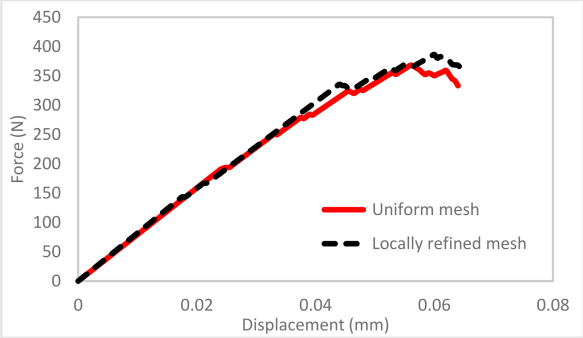

Figure 6.16: Load-displacement diagram for arbitrary propagation in a single edge notch test.

patterns almost coincide. As expected, a smoother contour results due to mesh refinement in the vicinity of the crack tip. This agreement is also shown by the load-displacement diagram in Figure 6.16.

6.7 Concluding remarks

An extended isogeometric approach (XIGA) has been developed for fracture simulation in a fluid-saturated porous medium. A cohesive-zone model governs the discontinuity for the solid part, while a two-pressure degrees of freedom (2PDOF) model has been adopted to account for the discontinuity within the pressure. Heaviside sign and step functions have been exploited to enforce compatibility perpendicular and parallel to the crack path in the forms of shifting and blending techniques, respectively. The higher continuity inherent in isogeometric analysis automatically ensures local mass conservation at element boundaries. The lack of such continuity is a deficiency observed in $\mathcal{C}^0$-continuous elements at their boundaries.

Non-Uniform Rational B-Splines (NURBS) basis functions have been adopted and then cast in the standard finite element data structure using Bézier extraction. The results are compared with findings from interface elements, as well as an interface-like enrichment.

Two types of enrichment have been assessed for XIGA: a global level-set based and a local elementwise enrichment. These approaches yield almost identical results. Moreover, the blending domain corresponding to these two enrichment schemes have been examined for the interface-like enrichment case, where no shifting exists and blending governs the compatibility enforcement. Again, the results are similar, in further support of earlier statements about about enrichment. An excellent agreement has been observed for the stationary crack problem compared to results by interface elements. Proof of the fluid-solid interaction has been observed at the hand of an interface permeability study. Straight and arbitrary fracturing have also been assessed and simulations yield most satisfactory results.

Chapter 7

Conclusion

EXtended IsoGeometric Analysis (XIGA) has been developed by blending IsoGeometric Analysis (IGA) and eXtended Finite Element Method (XFEM) to simulate fracturing in solids and fluid saturated porous media. To this end, Non-Uniform Rational B-splines (NURBS) have been utilised in an element-based finite element data structure by means of Bézier extraction. Similar to other extended approaches, XIGA decouples the crack path from the spatial discretisation, enabling a crack extension to be defined only on the original mesh layout. Implementation aspects have been carried out for compatibility enforcement, enhancement of individual control points, integration scheme, point projection, nonlocal-based determination of crack extension direction and so on. Moreover, efficacy of the porposed approach is benchmarked against those of XFEM and standard interface element approaches, subsuming small strain and particularly geometric nonlinearity, for instance simulating delamination in fibre-reinforced composites. Developed extended framework has also been incorporated into new territories, to enhance the isogeometric finite element analysis with entropy-based meshfree approaches. The viability of the approaches and the methodologies are assessed at hand of several examples comprised of straight and arbitrary fracturing. In the remainder, a brief summary of conclusions and goals achieved in each chapter are presented[1].

[1]Partially adopted from:

Fathi, F., Chen, L. and de Borst, R., 2020. Extended isogeometric analysis for cohesive fracture. International Journal for Numerical Methods in Engineering, 121(20), pp.4584-4613.

Fathi, F. and de Borst, R., 2021. Geometrically nonlinear extended isogeometric analysis for cohesive fracture with applications to delamination in composites. Finite Elements in Analysis and Design, 191, p.103527.

Fathi, F., Chen, L. and de Borst, R., 2021. X-IGALME: Isogeometric analysis extended with local maximum entropy for fracture analysis. International Journal for Numerical Methods in Engineering.

Fathi, F., Chen, L. , Hageman, T. and de Borst, R., 2021. Extended isogeometric analysis of a progressively fracturing fluid-saturated porous medium. Submitted to International Journal for Numerical Methods in Engineering

7.1 Extended IsoGeometric Analysis for Cohesive Fracture

An extended isogeometric analysis procedure has been developed for cohesive fracture in solids.

7.1.1 Goals achieved

- Compatibility between the standard and the enhanced fields has been enforced by utilising shifting technique in the direction perpendicular to the crack path. An additional blending technique in the form of a Heaviside step function has been exploited to remove undesired discontinuous field in front of the crack tip, which is also capable of locating a more realistic position of the crack tip inside an element.

- By virtue of knot insertion, the Kronecker-delta property of Lagrange interpolants has been retrieved in IGA at the expense of more degrees of freedom employed and consequently a higher computational cost involved. The performance of XIGA has been compared to XFEM while the compatibility is fully enforced.

- Complications ensue for XIGA due to the higher-order continuity of B-splines and NURBS which affect more rows of elements parallel to the crack path compared to a standard use of shifting technique in XFEM, i.e. the lack of Kronecker-delta property in splines impedes the compatibility to be fully enforced in shifting technique. This is, however, reminiscent of the blending technique adopted in extended approaches, particularly for quadratic and cubic orders where only one extra row of elements parallel to the crack path are involved at sides of the crack.

- The accuracy with respect to different orders of continuity for the standard and the enhanced parts of the displacement field has been investigated. It has been shown that, when using the same order for both parts, XIGA works perfectly irrespective of the order of continuity at element boundaries. For a different order of continuity, however, Bézier points ($\mathcal{C}^0$-continuity at element boundaries) should be used for both parts.

- Crack-void interaction and arbitrary fracturing have also been examined for the proposed method, showing an excellent performance of XIGA in capturing holes and free cracks simultaneously.

7.1.2 Future prospects

Other than those covered in the next chapters,

- A corrected XIGA formulation can be developed by augmenting the present shifting technique with an extra blending technique to account for continuity orders higher than

cubic. This will lead to a result identical to the standard blending technique without the conflicts reported in [39] for XIGA implementations.

7.2 Geometrically Nonlinear XIGA

Extended isogeometric analysis has been formulated for geometrically nonlinear cohesive fracture.

7.2.1 Goals achieved

- The formulation has been developed on a Total Lagrangian Formalism which facilitates avoiding the undesired enhanced field in the elements adjacent to the cracked ones to contribute to updating the position field in the Updated Lagrangian formalism, i.e. elimination of a source of error which may aggravate the convergence. Moreover, using the reference configuration removes any difficulty about the computation of the crack opening and subsequently the traction-opening relationship in the current configuration, especially while severe rotations are confronted.

- The use of a sign function rather than a Heaviside step function has removed the need to make an assumption for the normal to the centreline of the crack. It has also been used to enforce compatibility in the shifting form. Preserving the higher-order continuity across element boundaries in IGA, the shifting technique is unable to fully localise the enhanced term to the cracked elements. This undesired excess of the enhanced field introduces a source of error whose effect is proportional to the element size, i.e. errors become negligible with fairly fine meshes. This trend has been observed for the XIGA results, which is absent in XFEM due to $\mathcal{C}^0$-continuity of the Lagrange interpolation at element boundaries, where shifting technique confines the enhanced field to the cracked elements. Nevertheless, It has been observed that the finest XIGA mesh needed is still coarser than that of XFEM, indicating the slightly better performance of XIGA compared to XFEM.

- A variety of examples have been examined including buckling and large rotations which assess the good performance of the sign function compared to the step function. In terms of degrees of freedom and convergence of the nonlinear solver the isogeometric formulation seems slightly superior to a standard formulation using Lagrangian interpolants.

7.2.2 Future prospects

- The formulation can be developed for a progressively fracturing porous medium to cover large deformation dominant materials, such as biological tissues.

7.3 IGA Enhanced with Local Maximum Entropy

Isogeometic analysis has been augmented with local maximum entropy in an extended framework, which has been coined X-IGALME.

7.3.1 Goals achieved

- The high accuracy of isogeometric analysis in capturing complex boundaries together with the high accuracy of the local maximum entropy approach in the interior has rendered the method an excellent alternative within the class of extended discretisation methods.

- The higher continuity-order provided by both IGA and LME has led to an improved estimate of stresses which is central in finding a better prediction of the crack extension direction. Moreover, it sets the scene for higher-order differential equations.

- The approach has been assessed for different NURBS orders, node-sets and values of the aspect ratio γ. It is proven that the choice for γ is node-set specific. Nevertheless, despite failing to return the conventional error pattern for mesh refinement, the errors show a better performance for X-IGALME in almost all cases. It has been observed that lower values for γ return correct results.

- The effect of γ on the energy dissipation has been investigated as well, supporting the conclusion about the better performance of the lower values of γ. This is in line with the hypothesis that the lower values of γ help in compatibility enforcement.

- A detailed sensitivity analysis of singularity has been performed on X-IGALME. The results indicate a guaranteed stability of the solution for X-IGALME, where XIGA and XFEM fail. Unlike these elementwise approaches, the singularity-free characteristic of X-IGALME facilitates a single prescription for enrichment in any condition, including void level set.

7.3.2 Future prospects

- An optimisation problem on how to choose the value of γ for a given node-set is a potential topic for a future research.

- The role of different quadrature rules on the solution is another topic to explore.
- The proposed approach can be developed for fluid saturated porous media, particularly due to the ultra-smooth ($\mathcal{C}^{\infty}$-continuity) characteristic of LME basis functions in the enhanced section.

7.4 XIGA for Fluid-Saturated Porous Media

An extended isogeometric analysis (XIGA) approach has been proposed for fracture simulation in fluid saturated porous media. A cohesive-zone model has been used at the discontinuity within the solid part, while a 2 pressure degrees of freedom (2PDOF) model has been adopted for the fluid.

7.4.1 Goals achieved

- Use of higher-order continuity available in B-splines automatically has satisfied the local mass balance at element boundaries, a quality absent in Lagrange basis functions used in the customary finite element approach.
- Use of NURBS has provided higher-order interelement continuity leading to continuous fluid flow and stresses even at element boundaries. The former satisfies the conservation of mass, while the latter improves stress estimates which subsequently leads to a more accurate determination of the crack extension.
- Compatibility enforcement has been realised of the solid and the fluid. Moreover, two types of enrichments have been assessed for XIGA: a global level-set based and a local elementwise enrichment. Both of these approaches have been proven valid for XIGA within porous media, as they render identical results. This has been supported by interface-like enrichment case too, where the blending domain corresponding to these two enrichment schemes have been examined in the absence of shifting.
- Solid-fluid interaction has been observed at the hand of interface permeability study. Straight and arbitrary fracturing have also been assessed with supporting validation tests including stationary and propagating cracks.

7.4.2 Future prospects

- The formulation can be developed for one and three pressure degrees of freedom (1PDOF and 3PDOF) models to account for the fluid flow along the discontinuity.
- The proposed approach can be extended to partially saturated porous media as well as multi-phase problems.

- A further development can be obtained by deriving the formulation for non-Newtonian fluids and hydraulic fracture problems.

Bibliography

[1] G. Alfano and M. A. Crisfield. Finite element interface models for the delamination analysis of laminated composites: mechanical and computational issues. *International Journal for Numerical Methods in Engineering*, 50:1701–1736, 2001.

[2] S. Alizadeh Sabet. *Application of a Cosserat Continuum Model to Non-associated Plasticity*. PhD thesis, University of Sheffield, 2020.

[3] O. Allix and A. Corigliano. Geometrical and interfacial non-linearities in the analysis of delamination in composites. *International Journal of Solids and Structures*, 36:2189–2216, 1999.

[4] O. Allix and P. Ladevèze. Interlaminar interface modelling for the prediction of delamination. *Composite Structures*, 22:235–242, 1992.

[5] F. Amiri, C. Anitescu, M. Arroyo, S. P. A. Bordas, and T. Rabczuk. Xlme interpolants, a seamless bridge between xfem and enriched meshless methods. *Computational Mechanics*, 53(1):45–57, 2014.

[6] M. Arroyo and M. Ortiz. Local maximum-entropy approximation schemes: a seamless bridge between finite elements and meshfree methods. *International Journal for Numerical Methods in Engineering*, 65:2167–2202, 2006.

[7] H. Askes and E. C. Aifantis. Gradient elasticity in statics and dynamics: an overview of formulations, length scale identification procedures, finite element implementations and new results. *International Journal of Solids and Structures*, 48(13):1962–1990, 2011.

[8] H. Askes, G. N. Wells, and R. de Borst. Novel discretization concepts. In R. de Borst and H. A. Mang, editors, *Comprehensive Structural Integrity*, volume Volume 3: Numerical and Computational Methods, pages 377–425. Elsevier, Oxford, 2003.

[9] I. Babuška and J. M. Melenk. The partition of unity method. *International Journal for Numerical Methods in Engineering*, 40:727–758, 1997.

[10] G. I. Barenblatt. The mathematical theory of equilibrium cracks in brittle fracture. *Archive of Applied Mechanics*, 7:55–129, 1962.

[11] Z. P. Bažant and B. H. Oh. Crack band theory for fracture of concrete. *Matériaux et construction*, 16(3):155–177, 1983.

[12] Y. Bazilevs, V. M. Calo, J. A. Cottrell, J. A. Evans, T. J. R. Hughes, S. Lipton, M. A. Scott, and T. W. Sederberg. Isogeometric analysis using t-splines. *Computer Methods in Applied Mechanics and Engineering*, 199(5-8):229–263, 2010.

[13] Y. Bazilevs, V. M. Calo, T. J. Hughes, and Y. Zhang. Isogeometric fluid-structure interaction: theory, algorithms, and computations. *Computational mechanics*, 43(1):3–37, 2008.

[14] Y. Bazilevs, V. M. Calo, Y. Zhang, and T. J. Hughes. Isogeometric fluid–structure interaction analysis with applications to arterial blood flow. *Computational Mechanics*, 38(4-5):310–322, 2006.

[15] T. Belytschko and T. Black. Elastic crack growth in finite elements with minimal remeshing. *International Journal for Numerical Methods in Engineering*, 45:601–620, 1999.

[16] T. Belytschko, Y. Y. Lu, and L. Gu. Element-free galerkin methods. *International journal for numerical methods in engineering*, 37(2):229–256, 1994.

[17] T. Belytschko, N. Moës, S. Usui, and C. Parimi. Arbitrary discontinuities in finite elements. *International Journal for Numerical Methods in Engineering*, 50(4):993–1013, 2001.

[18] M. A. Biot. *Mechanics of incremental deformations*. 1965.

[19] A. Bompadre, L. E. Perotti, C. J. Cyron, and M. Ortiz. Convergent meshfree approximation schemes of arbitrary order and smoothness. *Computer Methods in Applied Mechanics and Engineering*, 221:83–103, 2012.

[20] J. Bonet and R. D. Wood. *Nonlinear Continuum Mechanics for Finite Element Analysis*. Cambridge University Press, Cambridge, 1997.

[21] T. J. Boone and A. R. Ingraffea. A numerical procedure for simulation of hydraulically-driven fracture propagation in poroelastic media. *International Journal for Numerical and Analytical Methods in Geomechanics*, 14(1):27–47, 1990.

[22] M. J. Borden, M. A. Scott, J. A. Evans, and T. J. R. Hughes. Isogeometric finite element data structures based on Bézier extraction of NURBS. *International Journal for Numerical Methods in Engineering*, 87:15–47, 2011.

[23] M. J. Borden, C. V. Verhoosel, M. A. Scott, T. J. Hughes, and C. M. Landis. A phase-field description of dynamic brittle fracture. *Computer Methods in Applied Mechanics and Engineering*, 217:77–95, 2012.

[24] F. Brezzi and M. Fortin. *Mixed and Hybrid Finite Element Methods*. Springer Verlag, Berlin - Heidelberg, 1991.

[25] P. Broumand and A. R. Khoei. The extended finite element method for large deformation ductile fracture problems with a non-local damage-plasticity model. *Engineering Fracture Mechanics*, 112:97–125, 2013.

[26] D. Chapelle and K.-J. Bathe. The inf-sup test. *Computers & Structures*, 47:537–545, 1993.

[27] L. Chen and R. de Borst. Cohesive fracture analysis using Powell-Sabin B-splines. *International Journal for Numerical and Analytical Methods in Geomechanics*, 43:625–640, 2019.

[28] L. Chen, E. J. Lingen, and R. de Borst. Adaptive hierarchical refinement of nurbs in cohesive fracture analysis. *International Journal for Numerical Methods in Engineering*, 112:2151–2173, 2017.

[29] L. Chen, C. V. Verhoosel, and R. de Borst. Discrete fracture analysis using locally refined t-splines. *International Journal for Numerical Methods in Engineering*, 116:117–140, 2018.

[30] J. A. Cottrell, T. J. R. Hughes, and Y. Bazilevs. *Isogeometric Analysis*. Wiley & Sons, Chichester, 2009.

[31] R. De Boer. Highlights in the historical development of the porous media theory: toward a consistent macroscopic theory. 1996.

[32] R. De Borst. *Computational methods for fracture in porous media: Isogeometric and extended finite element methods*. Elsevier, 2017.

[33] R. de Borst. Fluid flow in fractured and fracturing porous media: A unified view. *Mechanics Research Communications*, 80:47–57, 2017.

[34] R. de Borst and L. Chen. The role of Bézier extraction in adaptive isogeometric analysis: Local refinement and hierarchical refinement. *International Journal for Numerical Methods in Engineering*, 113:999–1019, 2018.

[35] R. de Borst, M. A. Crisfield, J. J. C. Remmers, and C. V. Verhoosel. *Nonlinear Finite Element Analysis of Solids and Structures*. John Wiley & Sons, Chichester, 2012.

[36] R. De Borst and H.-B. Mühlhaus. Gradient-dependent plasticity: formulation and algorithmic aspects. *International journal for numerical methods in engineering*, 35(3):521–539, 1992.

[37] R. De Borst, J. Réthoré, and M.-A. Abellan. A numerical approach for arbitrary cracks in a fluid-saturated medium. *Archive of Applied Mechanics*, 75(10):595–606, 2006.

[38] R. De Borst and L. Sluys. Localisation in a cosserat continuum under static and dynamic loading conditions. *Computer Methods in Applied Mechanics and Engineering*, 90(1-3):805–827, 1991.

[39] E. De Luycker, D. J. Benson, T. Belytschko, Y. Bazilevs, and M. C. Hsu. X-FEM in isogeometric analysis for linear fracture mechanics. *International Journal for Numerical Methods in Engineering*, 87:541–565, 2011.

[40] C. A. Duarte and J. T. Oden. H-p clouds—an h-p meshless method. *Numerical Methods for Partial Differential Equations: An International Journal*, 12(6):673–705, 1996.

[41] D. S. Dugdale. Yielding of steel sheets containing slits. *Journal of the Mechanics and Physics of Solids*, 8:100–108, 1960.

[42] P. Dumstorff. *Modellierung und Numerische Simulation von Rissfortschritt in Spröden und Quasi-Spröden Materialien auf Basis der Extended Finite Element Method*. PhD thesis, Ruhr-Universität Bochum, Bochum, 2006.

[43] F. Fathi, S. H. Ardakani, P. F. Dehaghani, and S. Mohammadi. A finite strain integral-type anisotropic damage model for fiber-reinforced materials: Application in soft biological tissues. *Computer Methods in Applied Mechanics and Engineering*, 322:262–295, 2017.

[44] F. Fathi, L. Chen, and R. de Borst. Extended isogeometric analysis for cohesive fracture. *International Journal for Numerical Methods in Engineering*, 121:4584–4613, 2020.

[45] F. Fathi, L. Chen, and R. de Borst. X-IGALME: Isogeometric analysis extended with local maximum entropy for fracture analysis. *International Journal for Numerical Methods in Engineering*, 2021.

[46] F. Fathi and R. de Borst. Geometrically nonlinear extended isogeometric analysis for cohesive fracture with applications to delamination in composites. *Finite Element in Analysis and Design*, 2021.

[47] K. P. Fathima and R. de Borst. Implications of single or multiple pressure degrees of freedom at fractures in fluid-saturated porous media. *Engineering Fracture Mechanics*, 213:1–20, 2019.

[48] P. H. Feenstra and R. De Borst. A plasticity model and algorithm for mode-i cracking in concrete. *International Journal for Numerical Methods in Engineering*, 38(15):2509–2529, 1995.

[49] M. Fleming, Y. Chu, B. Moran, and T. Belytschko. Enriched element-free galerkin methods for crack tip fields. *International journal for numerical methods in engineering*, 40(8):1483–1504, 1997.

[50] T. P. Fries. A corrected XFEM approximation without problems in blending elements. *International Journal for Numerical Methods in Engineering*, 75:503–532, 2008.

[51] T. P. Fries and T. Belytschko. The extended/generalized finite element method: an overview of the method and its applications. *International Journal for Numerical Methods in Engineering*, 84:253–304, 2010.

[52] J. Geertsma and F. De Klerk. A rapid method of predicting width and extent of hydraulically induced fractures. *Journal of petroleum technology*, 21(12):1571–1581, 1969.

[53] S. S. Ghorashi, N. Valizadeh, and S. Mohammadi. Extended isogeometric analysis for simulation of stationary and propagating cracks. *International Journal for Numerical Methods in Engineering*, 89:1069–1101, 2012.

[54] H. Gómez, V. M. Calo, Y. Bazilevs, and T. J. R. Hughes. Isogeometric analysis of the Cahn-Hilliard phase-field model. *Computer Methods in Applied Mechanics and Engineering*, 197:4333–4352, 2008.

[55] M. Goudarzi and S. Mohammadi. Weak discontinuity in porous media: an enriched EFG method for fully coupled layered porous media. *International Journal for Numerical and Analytical Methods in Geomechanics*, 38:1792–1822, 2014.

[56] M. Goudarzi and S. Mohammadi. Analysis of cohesive cracking in saturated porous media using an extrinsically enriched EFG method. *Computers and Geotechnics*, 63:183–198, 2015.

[57] A. A. Griffith. The phenomena of rupture and flow in solids. *Philosophical Transactions of the Royal Society of London*, A221:163–198, 1921.

[58] T. Hageman and R. de Borst. Flow of non-newtonian fluids in fractured porous media: Isogeometric vs standard finite element discretisation. *International Journal for Numerical and Analytical Methods in Geomechanics*, 43(11):2020–2037, 2019.

[59] T. Hageman and R. de Borst. A convergence study of monolithic simulations of flow and deformation in fractured poroelastic media. *International Journal for Numerical Methods in Engineering*, 121(3):393–410, 2020.

[60] T. Hageman and R. de Borst. Sub-grid models for multiphase fluid flow inside fractures in poroelastic media. *Journal of Computational Physics*, 414:109481, 2020.

[61] T. Hageman and R. de Borst. A refined two-scale model for newtonian and non-newtonian fluids in fractured poroelastic media. *Journal of Computational Physics*, 441:110424, 2021.

[62] T. Hageman, K. P. Fathima, and R. de Borst. Isogeometric analysis of fracture propagation in saturated porous media due to a pressurised non-newtonian fluid. *Computers and Geotechnics*, 112:272–283, 2019.

[63] T. Hageman, S. A. Sabet, and R. de Borst. Convergence in non-associated plasticity and fracture propagation for standard, rate-dependent, and cosserat continua. *International Journal for Numerical Methods in Engineering*, 122(3):777–795, 2021.

[64] A. Hillerborg, M. Modéer, and P. E. Petersson. Analysis of crack formation and crack growth in concrete by means of fracture mechanics and finite elements. *Cement and Concrete Research*, 6:773–781, 1976.

[65] A. Huerta and S. Fernández-Méndez. Enrichment and coupling of the finite element and meshless methods. *International Journal for Numerical Methods in Engineering*, 48:1615–1636, 2000.

[66] T. J. Hughes, J. A. Cottrell, and Y. Bazilevs. Isogeometric analysis: Cad, finite elements, nurbs, exact geometry and mesh refinement. *Computer methods in applied mechanics and engineering*, 194(39-41):4135–4195, 2005.

[67] J. M. Huyghe and J. D. Janssen. Quadriphasic mechanics of swelling incompressible porous media. *International Journal of Engineering Science*, 35(8):793–802, 1997.

[68] A. R. Ingraffea and V. Saouma. Numerical modelling of discrete crack propagation in reinforced and plain concrete. In *Fracture Mechanics of Concrete*, pages 171–225. Martinus Nijhoff Publishers, Dordrecht, 1985.

[69] G. Irwin. Analysis of stresses and strains near the end of a crack traversing a plate. *Journal of Applied Mechanics*, 24:361–364, 1957.

[70] F. Irzal, J. J. Remmers, J. M. Huyghe, and R. de Borst. A large deformation formulation for fluid flow in a progressively fracturing porous material. *Computer Methods in Applied Mechanics and Engineering*, 256:29–37, 2013.

[71] F. Irzal, J. J. Remmers, C. V. Verhoosel, and R. de Borst. Isogeometric finite element analysis of poroelasticity. *International Journal for Numerical and Analytical Methods in Geomechanics*, 37(12):1891–1907, 2013.

[72] F. Irzal, J. J. C. Remmers, C. V. Verhoosel, and R. de Borst. An isogeometric analysis Bézier interface element for mechanical and poromechanical fracture problems. *International Journal for Numerical Methods in Engineering*, 97:608–628, 2014.

[73] M. Jirasek. Nonlocal damage mechanics. *Revue Européenne de Génie Civil*, 11:993–1021, 2007.

[74] P. Kagan and A. Fischer. Integrated mechanically based CAE system using b-spline finite elements. *Computer-Aided Design*, 32(8-9):539–552, 2000.

[75] P. Kagan, A. Fischer, and P. Z. Bar-Yoseph. New B-spline finite element approach for geometrical design and mechanical analysis. *International Journal for Numerical Methods in Engineering*, 41(3):435–458, 1998.

[76] M. Kästner, P. Metsch, and R. de Borst. Isogeometric analysis of the Cahn-Hilliard equation – a convergence study. *Journal of Computational Physics*, 305:360–371, 2016.

[77] A. R. Khoei. *Extended Finite Element Method: Theory and Applications*. John Wiley & Sons, Chichester, 2014.

[78] A. R. Khoei and E. Haghighat. Extended finite element modeling of deformable porous media with arbitrary interfaces. *Applied Mathematical Modelling*, 35:5426–5441, 2011.

[79] I. Kolo, H. Askes, and R. de Borst. Convergence analysis of laplacian-based gradient elasticity in an isogeometric framework. *Finite Elements in Analysis and Design*, 135:56–67, 2017.

[80] I. Kolo and R. de Borst. Dispersion and isogeometric analyses of second-order and fourth-order implicit gradient-enhanced plasticity models. *International Journal for Numerical Methods in Engineering*, 114(4):431–453, 2018.

[81] I. Kolo and R. de Borst. An isogeometric analysis approach to gradient-dependent plasticity. *International Journal for Numerical Methods in Engineering*, 113(2):296–310, 2018.

[82] S. Kumar, K. Danas, and D. M. Kochmann. Enhanced local maximum-entropy approximation for stable meshfree simulations. *Computer Methods in Applied Mechanics and Engineering*, 344:858–886, 2019.

[83] P. Laborde, J. Pommier, Y. Renard, and M. Salaün. High-order extended finite element method for cracked domains. *International Journal for Numerical Methods in Engineering*, 64:354–381, 2005.

[84] R. W. Lewis, R. W. Lewis, and B. Schrefler. *The finite element method in the static and dynamic deformation and consolidation of porous media*. John Wiley & Sons, 1998.

[85] K. Malakpoor, E. F. Kaasschieter, and J. M. Huyghe. Mathematical modelling and numerical solution of swelling of cartilaginous tissues. part i: modelling of incompressible charged porous media. *ESAIM: Mathematical Modelling and Numerical Analysis*, 41(4):661–678, 2007.

[86] K. Malakpoor, E. F. Kaasschieter, and J. M. Huyghe. Mathematical modelling and numerical solution of swelling of cartilaginous tissues. part ii: Mixed-hybrid finite element solution. *ESAIM: Mathematical Modelling and Numerical Analysis*, 41(4):679–712, 2007.

[87] S. May, R. de Borst, and J. Vignollet. Powell-Sabin B-splines for smeared and discrete approaches to fracture in quasi-brittle materials. *Computer Methods in Applied Mechanics and Engineering*, 307:193–214, 2016.

[88] J. Mazars and G. Pijaudier-Cabot. Continuum damage theory—application to concrete. *Journal of engineering mechanics*, 115(2):345–365, 1989.

[89] D. Millán, A. Rosolen, and M. Arroyo. Thin shell analysis from scattered points with maximum-entropy approximants. *International Journal for Numerical Methods in Engineering*, 85:723–751, 2011.

[90] N. Moës and T. Belytschko. Extended finite element method for cohesive crack growth. *Engineering Fracture Mechanics*, 69:813–833, 2002.

[91] N. Moës, J. Dolbow, and T. Belytschko. A finite element method for crack growth without remeshing. *International Journal for Numerical Methods in Engineering*, 46:131–150, 1999.

[92] N. Moës, A. Gravouil, and T. Belytschko. Non-planar 3d crack growth by the extended finite element and level sets—part i: Mechanical model. *International journal for numerical methods in engineering*, 53(11):2549–2568, 2002.

[93] S. Mohammadi. *Extended Finite Element Method for Fracture Analysis of Structures*. John Wiley & Sons, Chichester, 2008.

[94] A. Needleman. Material rate dependence and mesh sensitivity in localization problems. *Computer methods in applied mechanics and engineering*, 67(1):69–85, 1988.

[95] N. Nguyen-Thanh, N. Valizadeh, M. Nguyen, H. Nguyen-Xuan, X. Zhuang, P. Areias, G. Zi, Y. Bazilevs, L. De Lorenzis, and T. Rabczuk. An extended isogeometric thin shell analysis based on kirchhoff–love theory. *Computer Methods in Applied Mechanics and Engineering*, 284:265–291, 2015.

[96] R. Nordgren. Propagation of a vertical hydraulic fracture. *Society of Petroleum Engineers Journal*, 12(04):306–314, 1972.

[97] C. Oomens, D. Van Campen, and H. Grootenboer. A mixture approach to the mechanics of skin. *Journal of biomechanics*, 20(9):877–885, 1987.

[98] D. Organ, M. Fleming, T. Terry, and T. Belytschko. Continuous meshless approximations for nonconvex bodies by diffraction and transparency. *Computational Mechanics*, 18:225–235, 1996.

[99] T. Perkins and L. R. Kern. Widths of hydraulic fractures. *Journal of petroleum technology*, 13(09):937–949, 1961.

[100] L. Piegl and W. Tiller. *The NURBS book*. Springer Science & Business Media, Dordrecht, 2012.

[101] G. Pijaudier-Cabot and Z. P. Bažant. Nonlocal damage theory. *Journal of engineering mechanics*, 113(10):1512–1533, 1987.

[102] T. Rabczuk and G. Zi. A meshfree method based on the local partition of unity for cohesive cracks. *Computational Mechanics*, 39:743–760, 2007.

[103] J. J. C. Remmers, R. de Borst, and A. Needleman. A cohesive segments method for the simulation of crack growth. *Computational Mechanics*, 31:69–77, 2003.

[104] J. Réthoré, R. d. Borst, and M.-A. Abellan. A two-scale approach for fluid flow in fractured porous media. *International Journal for Numerical Methods in Engineering*, 71(7):780–800, 2007.

[105] J. Réthoré, R. de Borst, and M.-A. Abellan. A discrete model for the dynamic propagation of shear bands in a fluid-saturated medium. *International journal for numerical and analytical methods in geomechanics*, 31(2):347–370, 2007.

[106] J. Réthoré, R. De Borst, and M.-A. Abellan. A two-scale model for fluid flow in an unsaturated porous medium with cohesive cracks. *Computational Mechanics*, 42(2):227–238, 2008.

[107] J. R. Rice and D. A. Simons. The stabilization of spreading shear faults by coupled deformation-diffusion effects in fluid-infiltrated porous materials. *Journal of Geophysical Research*, 81:5322–5334, 1976.

[108] A. Rosolen and M. Arroyo. Blending isogeometric analysis and local maximum entropy meshfree approximants. *Computer Methods in Applied Mechanics and Engineering*, 264:95–107, 2013.

[109] A. Rosolen, D. Millán, and M. Arroyo. On the optimum support size in meshfree methods: a variational adaptivity approach with maximum-entropy approximants. *International Journal for Numerical Methods in Engineering*, 82:868–895, 2010.

[110] A. Rosolen, D. Millán, and M. Arroyo. Second-order convex maximum entropy approximants with applications to high-order pde. *International Journal for Numerical Methods in Engineering*, 94:150–182, 2013.

[111] J. G. Rots. Computational modeling of concrete fracture. 1988.

[112] A. G. Sanchez-Rivadeneira and C. A. Duarte. A stable generalized/eXtended FEM with discontinuous interpolants for fracture mechanics. *Computer Methods in Applied Mechanics and Engineering*, 345:876–918, 2019.

[113] R. S. Sandhu, H. Liu, and K. J. Singh. Numerical performance of some finite element schemes for analysis of seepage in porous elastic media. *International Journal for Numerical and Analytical Methods in Geomechanics*, 1:177–194, 1977.

[114] J. C. J. Schellekens and R. de Borst. On the numerical integration of interface elements. *International Journal for Numerical Methods in Engineering*, 36:43–66, 1993.

[115] J. C. J. Schellekens and R. de Borst. Free edge delamination in carbon-epoxy laminates: a novel numerical/experimental approach. *Composite Structures*, 28:357–373, 1994.

[116] B. A. Schrefler, S. Secchi, and L. Simoni. On adaptive refinement techniques in multifield problems including cohesive fracture. *Computer Methods in Applied Mechanics and Engineering*, 195:444–461, 2006.

[117] M. A. Scott, M. J. Borden, C. V. Verhoosel, T. W. Sederberg, and T. J. Hughes. Isogeometric finite element data structures based on bézier extraction of t-splines. *International Journal for Numerical Methods in Engineering*, 88(2):126–156, 2011.

[118] S. Secchi, L. Simoni, and B. A. Schrefler. Mesh adaptation and transfer schemes for discrete fracture propagation in porous materials. *International Journal for Numerical and Analytical Methods in Geomechanics*, 31:331–345, 2007.

[119] T. W. Sederberg, J. Zheng, A. Bakenov, and A. Nasri. T-splines and t-nurccs. *ACM transactions on graphics (TOG)*, 22(3):477–484, 2003.

[120] J. M. Segura and I. Carol. On zero-thickness interface elements for diffusion problems. *International Journal for Numerical and Analytical Methods in Geomechanics*, 28:947–962, 2004.

[121] J. M. Segura and I. Carol. Coupled HM analysis using zero-thickness interface elements with double nodes. Part I: Theoretical model. *International Journal for Numerical and Analytical Methods in Geomechanics*, 32:2083–2101, 2008.

[122] J. C. Simo, J. Oliver, and F. Armero. An analysis of strong discontinuities induced by strain-softening in rate-independent inelastic solids. *Computational Mechanics*, 12:277–296, 1993.

[123] S. K. Singh, I. V. Singh, G. Bhardwaj, and B. K. Mishra. A Bézier extraction based XIGA approach for three-dimensional crack simulations. *Advances in Engineering Software*, 125:55–93, 2018.

[124] L. Sluys and R. De Borst. Wave propagation and localization in a rate-dependent cracked medium—model formulation and one-dimensional examples. *International Journal of Solids and Structures*, 29(23):2945–2958, 1992.

[125] H. Snijders, J. Huyghe, and J. Janssen. Triphasic finite element model for swelling porous media. *International Journal for Numerical Methods in Fluids*, 20(8-9):1039–1046, 1995.

[126] F. L. Stazi, E. Budyn, J. Chessa, and T. Belytschko. An extended finite element method with higher-order elements for curved cracks. *Computational Mechanics*, 31:38–48, 2003.

[127] M. Stolarska, D. L. Chopp, N. Moës, and T. Belytschko. Modelling crack growth by level sets in the extended finite element method. *International journal for numerical methods in Engineering*, 51(8):943–960, 2001.

[128] N. Sukumar. Construction of polygonal interpolants: a maximum entropy approach. *International Journal for Numerical Methods in Engineering*, 61:2159–2181, 2004.

[129] N. Sukumar, D. L. Chopp, N. Moës, and T. Belytschko. Modeling holes and inclusions by level sets in the extended finite-element method. *Computer methods in applied mechanics and engineering*, 190(46-47):6183–6200, 2001.

[130] D. Swenson and A. Ingraffea. Modeling mixed-mode dynamic crack propagation nsing finite elements: theory and applications. *Computational Mechanics*, 3(6):381–397, 1988.

[131] R. L. Taylor, O. C. Zienkiewicz, and E. Oñate. A hierarchical finite element method based on the partition of unity. *Computer Methods in Applied Mechanics and Engineering*, 152:73–84, 1998.

[132] K. Terzaghi, R. B. Peck, and G. Mesri. *Soil mechanics in engineering practice*. John Wiley & Sons, 1996.

[133] D. C. Thomas, M. A. Scott, J. A. Evans, K. Tew, and E. J. Evans. Bézier projection: a unified approach for local projection and quadrature-free refinement and coarsening of NURBS and T-splines with particular application to isogeometric design and analysis. *Computer Methods in Applied Mechanics and Engineering*, 284:55–105, 2015.

[134] J. F. Unger, S. Eckardt, and C. Könke. Modelling of cohesive crack growth in concrete structures with the extended finite element method. *Computer Methods in Applied Mechanics and Engineering*, 196:4087–4100, 2007.

[135] N. Valizadeh, Y. Bazilevs, J. S. Chen, and T. Rabczuk. A coupled IGA-meshfree discretization of arbitrary order of accuracy and without global geometry parameterization. *Computer Methods in Applied Mechanics and Engineering*, 293:20–37, 2015.

[136] R. Van Loon, J. M. Huyghe, M. Wijlaars, and F. P. Baaijens. 3D FE implementation of an incompressible quadriphasic mixture model. *International journal for numerical methods in engineering*, 57(9):1243–1258, 2003.

[137] W. J. Vankan, J. M. Huyghe, D. W. Slaaf, C. C. Van Donkelaar, M. R. Drost, J. D. Janssen, and A. Huson. Finite-element simulation of blood perfusion in muscle tissue during compression and sustained contraction. *American Journal of Physiology-Heart and Circulatory Physiology*, 273(3):H1587–H1594, 1997.

[138] C. V. Verhoosel, M. A. Scott, R. de Borst, and T. J. R. Hughes. An isogeometric approach to cohesive zone modeling. *International Journal for Numerical Methods in Engineering*, 87:336–360, 2011.

[139] A. Verruijt. *Computational geomechanics*, volume 7. Springer Science & Business Media, 1995.

[140] J. Vignollet, S. May, and R. d. Borst. Isogeometric analysis of fluid-saturated porous media including flow in the cracks. *International Journal for Numerical Methods in Engineering*, 108(9):990–1006, 2016.

[141] J. Vignollet, S. May, and R. de Borst. On the numerical integration of isogeometric interface elements. *International Journal for Numerical Methods in Engineering*, 102:1773–1749, 2015.

[142] G. N. Wells. *Discontinuous modelling of strain localisation and failure*. Delft University of Technology, 2001.

[143] G. N. Wells, R. de Borst, and L. J. Sluys. A consistent geometrically non-linear approach for delamination. *International Journal for Numerical Methods in Engineering*, 54:1333–1355, 2002.

[144] G. N. Wells and L. J. Sluys. A new method for modelling cohesive cracks using finite elements. *International Journal for Numerical Methods in Engineering*, 50:2667–2682, 2001.

[145] G. N. Wells, L. J. Sluys, and R. de Borst. Simulating the propagation of displacement discontinuities in a regularized strain-softening medium. *International Journal for Numerical Methods in Engineering*, 53:1235–1256, 2002.

[146] Q. Zhang, I. Babuška, and U. Banerjee. Robustness in stable generalized finite element methods (SGFEM) applied to Poisson problems with crack singularities. *Computer Methods in Applied Mechanics and Engineering*, 311:476–502, 2016.

[147] C. Zimmermann and R. A. Sauer. Adaptive local surface refinement based on LR NURBS and its application to contact. *Computational Mechanics*, 60(6):1011–1031, 2017.